UNIVERSITY OF CRETE

DEPARTMENT OF PHYSICS

On the design of InN nano-heterostructures for Field Effect Transistors

A dissertation submitted in partial satisfaction of

the requirements for the degree of

Bachelor of Science

in

Physics

by

AIAS ASTERIS

June 2023

This page is intentionally left blank.

Examination Committee

Prof. Alexandros Georgakilas (supervisor)

Prof. Eleftherios Iliopoulos

Dr. Charalambos Katsidis

June, 2023

Heraklion, Crete, Greece

Abstract

InN is a III-V semiconductor with a small electron effective mass, high electron mobility and the highest electron drift velocity ever reported in solid-state devices. InN is thus a prominent candidate for the channel of field-effect transistors (FETs) that operate in the terahertz region. The realization of InN-based FETs, however, is hindered by several impediments; surface electron accumulation due to InN surface states, high bulk electron concentration, and crystal defects introduced by the large lattice mismatch between InN and potential substrates. Polarization in InN heterostructures significantly affects electron distribution within InN, too.

In an attempt to better understand planar heterostructures for III-nitride FETs, self-consistent Schrödinger-Poisson (SCSP) calculations have been implemented for the equilibrium energy band and charge distribution profiling of InN channels on GaN, AlN and $In_{0.8}Al_{0.2}N$ (0001) buffer layers. Metal-Insulator-Semiconductor (MIS) structures have also been investigated, using Si_3N_4, HfO_2, Al_2O_3, or SiO_2 as the insulator.

The polarization-induced charge at the InN/AlN-buffer interface contributes to the channel depletion of electrons, yet favors hole accumulation near said interface. The two-dimensional hole gas could be prevented by assuming a positive charge contribution by misfit dislocations, equal to +1e per 5 nm of dislocation line. The formation of MIS systems facilitates channel electron depletion, with depletion efficiency increasing with insulator dielectric constant. Considering a compressively strained InN film on $In_{0.8}Al_{0.2}N$ buffer layer yields similar results with the case of the AlN buffer. The pseudomorphic InN growth would reduce the density of crystal defects that degrade the electron transport properties in the InN layers, rendering the incorporation of the $In_{0.8}Al_{0.2}N$ buffer preferable.

Ultra-thin, continuous 2-5 nm InN films have been successfully grown on GaN and AlN (0001) buffer layers by plasma-assisted molecular beam epitaxy (PA-MBE). In-situ streaky RHEED patterns and post-growth AFM measurements indicated two-dimensional, step-flow growth and atomic-smooth surfaces.

Acknowledgements

I would like to take this opportunity to extend my gratitude to all the members of the Microelectronics Research Group (MRG) of the University of Crete and the Foundation for Research and Technology - Hellas (FORTH). First and foremost, I am indebted to Prof. Alexandros Georgakilas for giving me the opportunity to join MRG and work on a fascinating research project, while his mentorship and unwavering support have opened doors to incredible opportunities in my educational endeavors. I would also like to thank Dr. Adam Adikimenakis and Dr. Charalampos Katsidis for their unending guidance and support throughout this thesis, teaching me so very much about all the techniques used for this work. Next, and from the bottom of my heart, I would like to thank Maria Kayambaki, Maria Androulidaki and Katerina Tsagkaraki not only for their technical support, but also for making me feel welcome to the group from day one. Finally, I would like to express my deepest appreciation to Prof. Eleftherios Iliopoulos for his invaluable guidance in my academic journey, which has played a significant role in shaping my future prospects.

Table of Contents

1. Introduction 1
    1.1 III-V Nitride Semiconductors 2
    1.2 Scope of This Work 2
2. Polarization in III-V Nitrides 5
    2.1 Polarization Fundamentals 5
    2.2 Properties of III-V Nitride Semiconductors 6
        2.2.1 Crystal Structure 6
        2.2.2 Piezoelectric Polarization 8
        2.2.3 Spontaneous Polarization 10
        2.2.4 Properties of Alloys 10
    2.3 Polarization-Induced 2DEG/2DHG 11
    2.4 High Electron Mobility Transistors 13
3. Molecular Beam Epitaxy 18
    3.1 Basic Physical Processes 18
    3.2 Plasma-Assisted MBE 20
    3.3 Growth Conditions 21
        3.3.1 Vacuum Conditions 21
        3.3.2 Substrate Temperature 22
        3.3.3 Beam Fluxes and III/V Flux Ratio 23
    3.4 Lattice Dislocations 24
        3.4.1 Lattice Mismatch 25
        3.4.2 Stain Relaxation Mechanisms 25
    3.5 Experimental PA-MBE Arrangement 26
        3.5.1 Load Chamber 26
        3.5.2 Transfer Chamber 27
        3.5.3 Growth Chamber 27
4. Characterization Techniques 32
    4.1 Reflection High-Energy Electron Diffraction 32
    4.2 Atomic Force Microscopy 35
    4.3 Hall-Effect Measurements 37
5. Schrödinger-Poisson Solver 42

5.1 The Equations 42
5.2 The Nextnano Software 43
5.3 Material Parameters and Simulation Conditions 44

6. Results & Discussion 48

6.1 Substrate Preparation 48
6.2 Thin InN Film Growth 49
6.3 Conductivity & Hall-Effect Measurements 50
6.4 Atomic Force Microscopy 50
6.5 Energy Band and Charge Distribution Profiling 51
6.5.1 The InN/GaN Heterostructure 53
6.5.2 The InN/AlN Heterostructure 58
6.5.3 The InN/$In_xAl_{1-x}N$/GaN Heterostructure 62
6.5.4 The InN/$In_xAl_{1-x}N$/AlN Heterostructure 67
6.5.5 The Effects of Dislocations 68
6.5.6 The Effects of Donor Concentration 69

7. Conclusions 75

1. Introduction

The invention of transistor in the late 1940s marked a major turning point in the field of electronics [1]. By replacing the cumbersome, fragile and inefficient vacuum tubes in electronic equipment, the semiconductor-based device opened up new possibilities of equipment miniaturization and enabled the development of increasingly powerful and efficient electronic devices. Transistors are responsible for the sky-rocketing of all modern technology and our entry into the digital age. They have allowed us to efficiently produce and process (computation), store (memory), and transmit and receive (communication) information. Transistors are nowadays a fundamental building block of modern electronics, as they are used in virtually all electronic devices, with their applications expanding from consumer electronics to healthcare, defense systems and space exploration.

However, in the age of the internet of things, artificial intelligence and big data, device efficiency demands get higher and more stringent by the day. Our technological infrastructure is called upon to process exponentially-increasing amounts of information at higher and higher speeds. Such a task could soon fall off the range of capabilities of the current state of electronics, so there is an ever-pressing need for high-frequency electronics, that operate with higher gain and efficiency. That is, there is a need for high-power and high-frequency transistors that will enable faster and more reliable networks, which in turn will perform the necessary tasks for next generations of technology, beyond 5G. III-nitride-based heterostructure field-effect transistors (HFETs) have stood out as the preferred transistor type for this purpose [2].

As the connection between material properties and microstructure became clearer, there have been increasing efforts to design transistors with the desired behavior. The focal point of past research had revolved around elemental semiconductors, such as silicon or germanium, or traditional III-V compound semiconductors, such as GaAs, GaP etc. [3]. Despite their contemporary success, the capabilities of said materials hindered further technological advances [2]. In the quest for materials with enhanced functionality, the main focus of interest then shifted to III-V nitride semiconductors (GaN, InN, AlN) and their alloys [3]. Their group specific characteristics hold great promise for the next generation of transistors, that will open the door to high-power and high-frequency electronics.

1.1 III-V Nitride Semiconductors

III-nitrides include the semiconductors AlN, GaN and InN, which have band gaps spanning the entire UV and visible ranges [4]. The interest in III-V nitrides began in the early

1990's with the demonstration of the first efficient blue light emitting diode [5] and the most efficient blue laser diode [6]. Since then, optical applications of this material system have involved UV, violet, blue and green light-emitting diodes and lasers, as well as solar cells [7]. Continued improvements in device development and efficiency have rapidly increased the interest in III-nitrides, which have expanded -among other applications- to high electron mobility transistors (HEMTs).

III-nitride semiconductors are prime candidates for high-frequency and high-power transistors. As the name suggests, III-V nitride semiconductors consist of one (or more, in the case of alloys) group-III elements and nitrogen. Due to the strong ionic nature of metal-nitrogen bonds and their non-centrosymmetric crystal structure, these materials exhibit significant polarization fields along the c-axis [8]. A discontinuity in polarization in a layered III-V nitride heterostructure can induce a two-dimensional electron gas [9] of high density and mobility [10, 11]. These spatially confined gases of mobile carriers can perform as highly conductive channel material for High Electron Mobility Transistors.

1.2 Scope of This Work

Over the past two decades, InN has risen as a prominent candidate for the next generation of electronics [12]. InN shows great potential as a channel material for future high-frequency and high-power transistors, as it demonstrates ultra-high electron peak-velocity and mobility [13, 2]. However, despite the significant progress in the development of InN epitaxial structures by plasma-assisted molecular beam epitaxy (PA-MBE) [14, 15], certain technological constrains of InN growth hinder the consistent development of InN-based devices. These impediments are the high bulk electron concentration [16], Fermi level pinning at the InN surface within the conduction band and formation of a surface electron accumulation layer [14, 17], large lattice mismatch between InN and either GaN or AlN buffer layers and the subsequent presence of misfit and threading dislocations [15], as well as electron accumulation at the highly defective epilayer/substrate interfaces [18].

This work aims to contribute to the design and growth optimization of InN heterostructures, that could control the charge accumulation in the InN layer, for the channel of field effect transistors. One-dimensional self-consistent Schrödinger-Poisson (SCSP) equation solving software was implemented for the theoretical examination of polarization effects on sheet charge density and band formation of said heterostructures. The effects of high-k dielectric materials in MIS systems are computationally examined. Guided by SCSP calculations, thin InN-on-GaN or AlN structures are developed by PA-MBE, using a radio frequency (RF) nitrogen plasma source. Conductivity and Hall effect measurements, and Atomic Force Microscopy have been utilized for sample evaluation.

The outline of this thesis is as follows. First, a brief introduction to polarization theory

is provided. Basic III-V nitride properties are discussed and the motivation behind this work is explained, by shedding light on the 2DEG (2DHG) formation at heterostructure interfaces. A quick description of MBE's physical mechanisms is given, discussing potential growth-related crystal imperfections. The experimental characterization techniques employed are briefly introduced, inspecting both in- and ex-situ techniques. The numerical tools used for this thesis are then explained. Finally, experimental and computational results are presented and discussed.

References

[1] *The Story of the Transistor.* Bell Telephone Laboratories, (1958).

[2] J. Kuzmik, A. Adikimenakis, M. Tapajna, D. Gregusova, S. Hascik, E. Dobrocka, K. Tsagaraki, R. Stoklas, and A. Georgakilas, *AIP Advances*, vol. **11**, no. 12, p. 125325, (2021).

[3] P. Rutennara, M. Albrecth, and J. Neugerbauer, in *Nitride Semiconductors - Handbook on Materials and Devices*, P. Rutennara, M. Albrecth, and J. Neugerbauer, Eds. Weinheim, Germany: Wiley-VCH, (2003).

[4] I. Vurgaftman and J. R. Meyer, *J. Appl. Phys.*, vol. **94**, no. 6, pp. 3675–3696, (2003).

[5] S. Nakamura, T. Mukai, and M. Senoh, *Appl. Phys. Lett.*, vol. **64**, no. 13, pp. 1687–1689, (1994).

[6] S. Nakamura et al., *Jpn. J. Appl. Phys.*, vol. **35**, p. L74, (1996).

[7] J. Wu, W. Walukiewicz, K. M. Yu, W. Shan, I. Ager, J. W., E. E. Haller, H. Lu, W. J. Schaff, W. K. Metzger, and S. Kurtz, *J. Appl. Phys.*, vol. **94**, no. 10, pp. 6477–6482, (2003).

[8] F. Bernardini, V. Fiorentini, and D. Vanderbilt, , *Phys. Rev. B*, vol. **56**, pp. R10 024–R10 027, (1997).

[9] O. Ambacher et al., *J. Appl. Phys.*, vol. **85**, no. 6, pp. 3222–3233, (1999).

[10] Y. Cao and D. Jena, *Appl. Phys. Lett.*, vol. **90**, no. 18, p. 182112, (2007).

[11] W. Wang et al., *Appl. Phys. Express*, vol. **5**, no. 1, p. 015502, (2012).

[12] A. G. Bhuiyan, A. Hashimoto, and A. Yamamoto, *J. Appl. Phys.*, vol. **94**, no. 5, pp. 2779–2808, (2003).

[13] V. M. Polyakov and F. Schwierz, *Appl. Phys. Lett.*, vol. **88**, no. 3, (2006), 032101.

[14] H. Lu, W. J. Schaff, L. F. Eastman, and C. E. Stutz, *Appl. Phys. Lett.*, vol. **82**, no. 11, pp. 1736–1738, (2003).

[15] E. Dimakis, E. Iliopoulos, K. Tsagaraki, T. Kehagias, P. Komninou, and A. Georgakilas, *J. Appl. Phys.*, vol. **97**, (2005), 113520.

[16] C. G. Van de Walle, J. L. Lyons, and A. Janotti, *phys. stat. sol. (a)*, vol. **207**, no. 5, pp. 1024–1036, (2010).

[17] I. Mahboob, T. D. Veal, C. F. McConville, H. Lu, and W. J. Schaff, *Phys. Rev. Lett.*, vol. **92**, p. 036804, (2004).

[18] C. C. Katsidis, A. O. Ajagunna, and A. Georgakilas, *J. Appl. Phys.*, vol. **113**, no. 7, (2013), 073502.

2. Polarization in III-V Nitrides

Advances in production (growth and fabrication) techniques of devices require the investigation of all physical effects taking place in solids, in order to understand them at a fundamental level. In that regard, polarization has been recognised as a meaningful tool of device engineering, due to its significant consequences on the electrostatics of materials.

This chapter serves to shed light over III-V nitrides' potential for high-power and high-frequency electronics. After a brief overview of the classical polarization theory that is the basis of this work, and III-nitride properties, with an emphasis on their electronic polarization. Polarization effects in the aforementioned material group are then investigated, paving the way towards the latter's application in high electron mobility transistors.

2.1 Polarization Fundamentals

To understand the use of nitride materials as the channel of field effect transistors, one must first take a step back to understand some simple, yet crucial concepts of polarization theory. The macroscopic polarization of solids is classically defined as the dipole moment per unit volume [1]. By such an approach, each unit cell of a crystalline object can be modeled as a microscopic dipole of moment $\vec{p_i}$. Over a volume V, the total polarization of a crystal is equal to:

$$\vec{P} = \frac{1}{V}\sum_i \vec{p_i} \tag{2.1.1}$$

The electric potential at point $\vec{r}$ of a dipole of moment $\vec{p}$ in position $\vec{r'}$ can be easily found to be:

$$V(\vec{r}) = \frac{1}{4\pi\epsilon_0}\frac{\vec{r}-\vec{r'}}{|\vec{r}-\vec{r'}|^3}\cdot\vec{p} \tag{2.1.2}$$

Expanding this equation to a solid with polarization $\vec{P}$, one should replace $\vec{p}$ with $d\vec{p} = \vec{P}(\vec{r'})d^3r'$, and therefore:

$$V(\vec{r}) = \frac{1}{4\pi\epsilon_0}\int_V \frac{\vec{r}-\vec{r'}}{|\vec{r}-\vec{r'}|^3}\cdot\vec{P}(\vec{r'})\ d^3r' \tag{2.1.3}$$

With some added dexterity and the divergence theorem, the equation above can be equivalently written as:

$$V(\vec{r}) = \frac{1}{4\pi\epsilon_0}\left(\oint_{\partial V} \frac{1}{|\vec{r}-\vec{r'}|}\vec{P}(\vec{r'}) \cdot d^2\vec{r'} - \int_V \frac{1}{|\vec{r}-\vec{r'}|}(\vec{\nabla}_{r'} \cdot \vec{P})\ d^3r'\right) \tag{2.1.4}$$

The first term corresponds to the potential of a polarization induced surface charge:

$$\sigma_p = \vec{P} \cdot \hat{n} \tag{2.1.5}$$

where $\hat{n}$ is the unit vector perpendicular to the boundary surface, and the second term corresponds to the potential of a polarization induced volume charge:

$$\rho_p = -\vec{\nabla} \cdot \vec{P} \tag{2.1.6}$$

These fundamental results are adequate for a qualitative understanding of what follows, i.e. how polarization inside a semiconductor crystalline material affects charge distribution and energy bands. An accurate evaluation of macroscopic polarization requires a quantum approach [2, 3]. However, all elastic constants and polarization moduli used below have been calculated implementing the quantum theory of polarization.

2.2 Properties of III-V Nitride Semiconductors

A distinctive property of III-V nitride semiconductors is their direct band-gap energies, which cover the whole visible spectrum, as shown in Fig. 2.1. III-V nitride semiconductors also exhibit strong polarization fields. Due to nitrogen's large electronegativity, metal-nitrogen bonds are of strong ionic character [4]. Consequently, such materials are characterized by large piezoelectric coefficients and, in turn, powerful piezoelectric polarization fields [5]. Their crystal structure, on the other hand, allows for the existence of a strong spontaneous polarization component [6].

2.2.1 Crystal Structure

Depending on growth conditions, III-V nitrides can exist in either zinc-blende or wurtzite structures. Contrary to most III-V compound semiconductors (GaAs, AlAs, GaP, InP etc.), which occur mainly in the former, III-V nitrides' stable phase is the wurtzite one [9].

The wurtzite hexagonal unit cell is characterized by lattice constants, a and c, as depicted in Fig. 2.2. The structure can equivalently be considered as two interpenetrating hexagonal closely packed (hcp) structures displaced by u (cell-internal parameter) along the c-axis (or the $\langle 0001 \rangle$ direction) [9]. The two hcp sub-lattices comprise solely metal

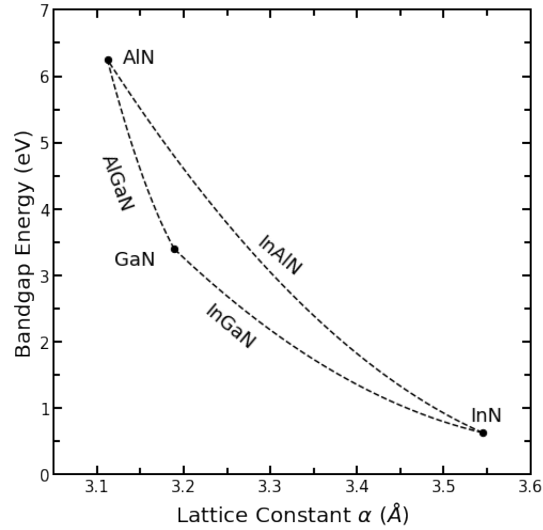

Fig. 2.1: Direct band-gap energy of binary III-V nitride semiconductors against their c-plane lattice constant. Data retrieved from [7, 8].

and nitrogen atoms, respectively. It should be noticed that in the case of an ideal (most dense) wurtzite crystal the lattice constant ratio is $\frac{c}{a} = \sqrt{\frac{8}{3}} = 1.633$ and u parameter is $u = \frac{3}{8} = 0.375$.

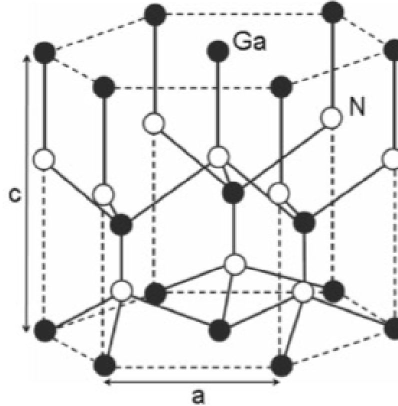

Fig. 2.2: The wurtzite crystal structure. The structure is formed by two intertwined hexagonal sublattices of, for instance, Ga and N atoms. Reprinted from [9].

The relative position of the hcp structures determines the polarity of the crystal. Due to the non-centrosymmetric nature of the wurtzite crystal, when cut on a {0001} plane with vertical bonds, the surface atoms can be either group-III elements or nitrogen, giving rise to two distinct polar surfaces. The first case, called metal (Ga, Al, In)-faced, occurs when the hcp structure of group-III atoms is lower (by uc) with respect to its nitrogen counterpart, showcased in Fig. 2.3a. This growth direction is conventionally considered as the [0001] crystallographic orientation. The opposite case, Fig. 2.3b, is called nitrogen (N)-faced and is identified as the $[000\bar{1}]$ direction. Each polar surface has unique chemical

and physical properties. Therefore, polarity has a vital role in material growth and device design.

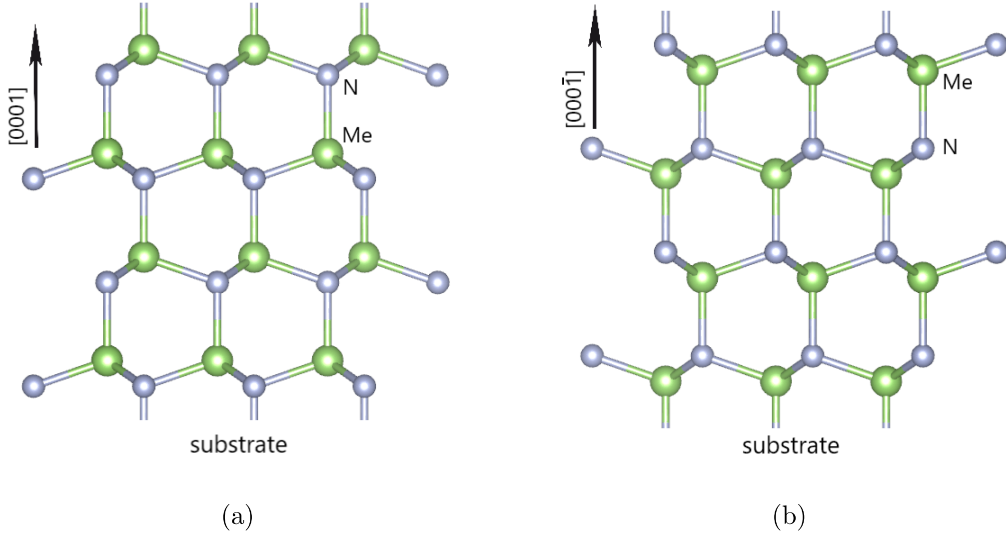

Fig. 2.3: (a) Me-face and (b) N-face polarity of the wurtzite phase.

2.2.2 Piezoelectric Polarization

Piezoelectric polarization of a crystal refers to the polarization induced by mechanical strain. When stressed in the (0001) plane, the aforementioned Me-N bonds are deformed, inducing a permanent dipole moment along the c-axis. Owing to the large ionicity of said bonds, wurtzite-based structures have strong strain-induced piezoelectric field [5, 10].

Using the piezoelectric moduli d_{ijk} and e_{ijk}, the piezoelectric polarization field along the ith axis can be expressed as [11]:

$$P_{pz,i} = d_{ijk}\sigma_{jk} = e_{ijk}\varepsilon_{jk} \tag{2.2.1}$$

where σ_{jk} is the stress tensor, ε_{jk} is the strain tensor. Summation over repeated indices is assumed. By Hooke's law, the deformation, ε_{kl}, of a linear elastic material subjected to external or internal stresses σ_{ij}, is equal to:

$$\sigma_{ij} = C_{ijkl}\ \varepsilon_{kl} \tag{2.2.2}$$

where C_{ijkl} is the elastic tensor of said material. Taking spatial symmetry into account, moduli d_{ijk} and e_{ijk} are symmetric with respect to the indices j and k [11]. By Voigt notation $(xx, yy, zz, yz, zx, xy \equiv 1, ..., 6)$, the aforementioned tensors can be rewritten in more concise matrix forms $(d_{ijk} \rightarrow d_{ij}, ..., \varepsilon_{jk} \rightarrow \varepsilon_j)$. Additionally, the wurtzite phase's

piezoelectric tensor is characterized of three independent non-zero coefficients. As a result, the e_{ij} and C_{ij} tensors assume the following forms:

$$e_{ij} = \begin{pmatrix} 0 & 0 & 0 & 0 & e_{15} & 0 \\ 0 & 0 & 0 & e_{15} & 0 & 0 \\ e_{31} & e_{31} & e_{33} & 0 & 0 & 0 \end{pmatrix} , \tag{2.2.3}$$

and

$$C_{ij} = \begin{pmatrix} C_{11} & C_{12} & C_{13} & 0 & 0 & 0 \\ C_{12} & C_{11} & C_{13} & 0 & 0 & 0 \\ C_{13} & C_{13} & C_{33} & 0 & 0 & 0 \\ 0 & 0 & 0 & C_{44} & 0 & 0 \\ 0 & 0 & 0 & 0 & C_{44} & 0 \\ 0 & 0 & 0 & 0 & 0 & \frac{1}{2}(C_{11} - C_{12}) \end{pmatrix} \tag{2.2.4}$$

From Eqs. 2.2.1-2.2.4, the piezoelectric polarization component along the c-axis can be calculated:

$$P_{pz,3} = e_{33}\varepsilon_3 + e_{31}(\varepsilon_1 + \varepsilon_2) \tag{2.2.5}$$

Considering biaxial stress, there is no stress in the z-direction, $\sigma_3 = C_{13}\varepsilon_1 + C_{13}\varepsilon_2 + C_{33}\varepsilon_3 = 0$, and the strain along the same direction is:

$$\varepsilon_3 = -2C_{13}/C_{33}\ \varepsilon_1 \tag{2.2.6}$$

Due to the isotropic (biaxial) strain along the (0001) plane:

$$\varepsilon_1 = \varepsilon_2 = \frac{a - a_0}{a_0} \tag{2.2.7}$$

with a and a_0 being the strained and relaxed lattice constants of the crystal, respectively. Finally, the c-axis piezoelectric polarization component is:

$$P_{pz,3} = 2\frac{a - a_0}{a_0}\left(e_{31} - e_{33}\frac{C_{13}}{C_{33}}\right) \tag{2.2.8}$$

Table 2.1 lists the lattice, piezoelectric and elastic constants for the major binary III-V nitride semiconductors. The piezoelectric constants of group-III nitrides are a factor of 10 larger than those of group-III arsenides [6].

Table 2.1: Physical properties of binary III-V nitride semiconductors at room temperature. Data retrieved from (a): Ref. [12], (b): Ref. [7], (c): Ref. [13], (d): Ref. [8].

Material	a (c) (Å)	E_{gap} (eV)	$e_{31}^{(c)}$ (C/m^2)	$e_{33}^{(c)}$ (C/m^2)	$C_{13}^{(d)}$ (C/m^2)	$C_{33}^{(d)}$ (C/m^2)	$P_{sp}^{(c)}$ (C/m^2)
InN	3.545(5.699)$^{(a)}$	0.63$^{(b)}$	-0.57	0.97	92	224	-0.042
GaN	3.189(5.185)	3.40$^{(d)}$	-0.35	1.27	106	398	-0.034
AlN	3.112(4.982)	6.25$^{(d)}$	-0.50	1.79	108	373	-0.090

2.2.3 Spontaneous Polarization

Wurtzite III-V nitride semiconductors exhibit spontaneous polarization due to the absence of inversion-symmetry axes [6] and the deviation from the ideal wurtzite structure [14]. This polarization arises from the difference in the electronegativities of the nitrogen and group-III elements, which causes a separation of charge in the direction perpendicular to the c-axis of the crystal. The orientation of spontaneous polarization of III-nitrides is always towards $[000\bar{1}]$ (from nitrogen atoms to group-III atoms). Therefore, considering the [0001] direction as positive, spontaneous polarization values are always negative, as listed in Table 2.1.

2.2.4 Properties of Alloys

InN, GaN and AlN can be combined into structures of mixed composition, called alloys. Nitride alloys consisting of two III-nitride semiconductors, i.e. $A_xB_{1-x}N$ $(0 < x < 1)$, are called ternary, and of three, i.e. $A_xB_yC_{1-x-y}N$ $(0 < x, y < 1)$, are called quaternary. As naturally expected, the chemical composition of a material bears important effects on its properties. That is, optical, electronic and mechanical properties of each alloy are dependent on its molar fractions, x and y.

For the calculation of lattice, elastic and piezoelectric constants for alloys, Vegard's law of linear interpolation may be invoked [15]. I.e., for an alloy $A_xB_{1-x}N$:

$$\begin{aligned} a_{ABN}(x) &= a_{AN}x + a_{BN}(1-x) \\ c_{ABN}(x) &= c_{AN}x + c_{BN}(1-x) \end{aligned} \tag{2.2.9}$$

and

$$e^{ij}_{ABN}(x) = e^{ij}_{AN}x + e^{ij}_{BN}(1-x)$$
$$C^{ij}_{ABN}(x) = C^{ij}_{AN}x + C^{ij}_{BN}(1-x) \tag{2.2.10}$$

By substituting Eqs. 2.2.8 and 2.2.9 into Eq. 2.2.4, piezoelectric polarization is calculated.

Energy gaps, cell-internal parameters and spontaneous polarization are non-linearly dependent on the molar fractions of the alloy. Instead they are approximated by quadratic equations of the form [4]:

$$Y_{ABN}(x) = Y_{AN}x + Y_{BN}(1-x) + b_{ABN}x(1-x) \tag{2.2.11}$$

where b_{ABN} is the bowing parameter. These parameters are a degree of deviation from the linear description, and are generally dependent on material composition [16, 17].

2.3 Polarization-Induced 2DEG/2DHG

The polarization-induced two-dimensional electron gas (2DEG) or hole gas (2DHG) is a unique feature of wurtzite III-V nitride semiconductors, which arises from the combination of spontaneous and piezoelectric polarization at heterointerfaces [4]. When a nitride material is grown on a substrate with a different polarization, an accumulation of bound charges occurs, as per Eqs. 2.1.5 and 2.1.6. The total bound charge can be expressed as:

$$\rho = -\vec{\nabla}(\vec{P}_{sp} + \vec{P}_{pz}) \tag{2.3.1}$$

This means a spatially changing polarization field creates a net bound charge in the crystal. In analogy, an abrupt polarization discontinuity can cause a fixed polarization surface charge. In the case of heterostructures, at the interface AN/BN, said polarization charge is:

$$\sigma_{AN/BN} = P_{BN} - P_{AN} = (P^{sp}_{BN} + P^{pz}_{BN}) - (P^{sp}_{AN} + P^{pz}_{AN}) \tag{2.3.2}$$

where AN, BN are any III-V nitride semiconductors. By Gauss' law, an electric field is established due to said sheet charge, which in turn leads to an accretion of electrons (if surface charge is positive), or holes (if negative) near the interface [18].

Let us consider, for example, a strained Al-faced AlN-on-GaN heterostructure. AlN has a lattice constant $a_{AlN} = 3.112$ Å, whereas GaN's lattice constant is $a_{GaN} = 3.189$ Å. In consequence, when AlN is pseudomorphically grown on GaN, AlN withstands a tensile stress in the (0001) plane and a piezoelectric polarization field arises towards $[000\bar{1}]$. GaN is relaxed and thus has no piezoelectric polarization field. The spontaneous polarization component for both materials is faced towards the $[000\bar{1}]$ direction. The change in

polarization when moving from the AlN layer to the GaN substrate gives rise to a positive sheet charge density at the interface:

$$\sigma/e = (P_{GaN} - P_{AlN})/e = 6.64 \times 10^{13}\ cm^{-2} \tag{2.3.3}$$

where e is the electron charge. In turn, this surface charge induces a 2DEG. The 2DEG formation takes place right beneath the interface, inside the low-bandgap semiconductor. In the case of an N-face substrate, all polarization fields are reversed. Subsequently, the polarization sheet charge is negative and a 2DHG would be induced beneath the interface, at the GaN side.

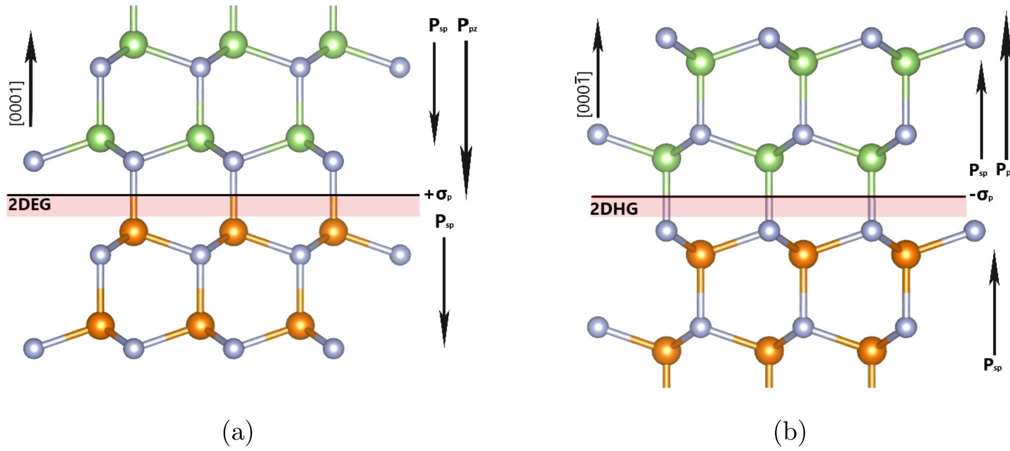

(a) (b)

Fig. 2.4: Polarization induced (a) 2DEG for a Ga-polar (b) 2DHG for an N-polar AlN/GaN interface. Green spheres correspond to Al, orange ones to Ga and grey ones to N.

A schematic energy band profile of the heterojunction is depicted in Fig. 2.5a. Φ_B is the Schottky barrier potential of the metal/AlN junction. The conduction band discontinuity ΔE_c stems from the bandgap difference (ΔE_g) of AlN and GaN, and may be approximated (in the ideal case) by their electron affinity difference. E is the electric field in the AlN barrier of thickness d. By Gauss' law, the electric field in AlN is pointing along the growth direction and of magnitude:

$$E = \frac{\sigma - e\ n_s}{\epsilon_{AlN}} \tag{2.3.4}$$

where σ (C/cm^2) is the polarization-induced surface charge, n_s (cm^{-2}) is the 2DEG density and ϵ_{AlN} is the dielectric constant of AlN. Due the polarization-induced conductivity and the bandgap of each material ($E_g^{GaN} < E_g^{AlN}$), a triangular quantum well is formed at GaN's surface. A flow of mobile charges, results in strong localization of electrons inside that well [18].

From Fig. 2.5a, the 2DEG density can be easily obtained. Setting the bottom of the

well as a reference point, it follows that

$$e\,\Phi_B \; - e\;E\;d \; - \; \Delta E_c \; + \; E_F = 0 \tag{2.3.5}$$

Substituting Eq. 2.3.4 into Eq. 2.3.5 and solving for n_s,

$$n_s = \frac{\sigma}{e} - \frac{\epsilon_{AlN}}{d\;e^2}\,(e\Phi_B - \Delta E_c + E_F) \tag{2.3.6}$$

The complementary band profile for a N-face heterostructure can be obtained by vertically mirroring Fig. 2.5a and exchanging the conduction band for the valence band[1].

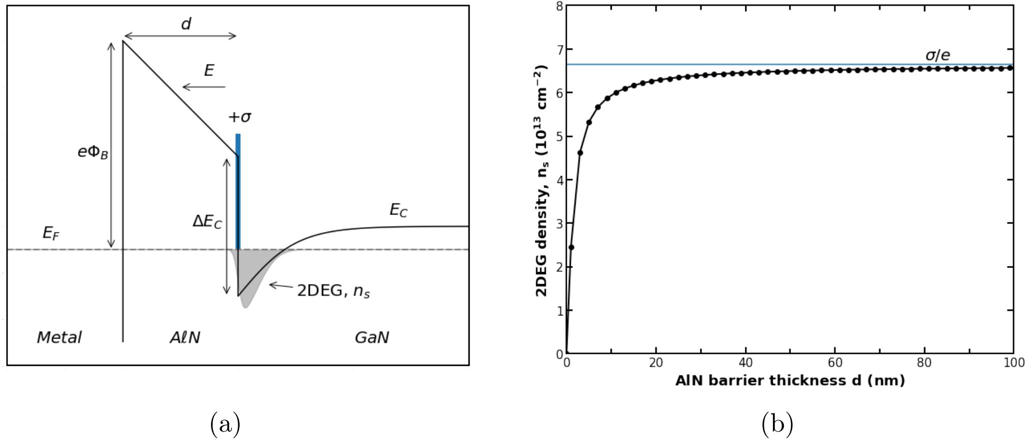

(a) (b)

Fig. 2.5: (a) Conduction band diagram of an AlN/GaN (0001) heterostructure, (b) 2DEG density versus AlN barrier thickness, using self-consistent Schrödinger-Poisson solution software.

In brief, polarization is an important tool for device engineering. Proper manipulation of polarization fields can facilitate the tailoring of emergent phenomena in solids. The most important polarization-induced phenomenon is the accumulation of mobile carriers into a spatially confined area, causing the formulation of two-dimensional electron or hole gases. Crucially, the accumulation of said gases is realized under doping-free conditions and as a result, such structures exhibit high carrier mobilities. These properties render III-V nitrides very attractive candidates for field effect transistors with high current and power-output densities.

2.4 High Electron Mobility Transistors

High Electron Mobility Transistors, or HEMTs, are field effect transistors (FETs) that incorporate a heterostructure, that results to the formation of a high-mobility 2DEG (or 2DHG). In the case of III-nitrides, the polarization induced 2DEG at the interface acts as

[1]Remember that electrons like to sink and holes to float in an electron energy band diagram

the channel of the transistor. Ohmic source and drain, and Schottky gate contacts are then fabricated on the heterostructure to utilize and control the 2DEG.

Generally, a HEMT may exist in two distinct operation types: normally-on and normally-off. In the normally-on type, the transistor's channel is populated by carriers in the absence of an external gate voltage bias (V_{gs}=V_{gate}-V_{source} =0). This means that when a drain-source voltage (V_{ds}) is applied current would flow through the channel, connecting the source-drain contacts, without the need for an additional gate voltage signal. A negative gate-source voltage ($V_{gs}<0$) must be applied to deplete the channel of electrons. Positive values of V_{gs} further enhance the electron density in the channel and thus increase the traversing drain-source current (I_{ds}). Normally-on devices are advantageous in applications where the transistor needs to be in an active or conducting state by default. On the other hand, in the normally-off state, the transistor's channel is non-conducting by default (V_{gs}=0), requiring an external gate voltage to enable conduction. Normally-off devices provide enhanced control and power efficiency, as they require an explicit voltage signal to activate the channel. These devices are particularly useful in applications where precision control, power conservation, or modulation is required. The choice between normally on and normally off transistors depends on the specific needs and requirements of the application at hand. The polarization-based HEMT structures are naturally of normally-on type and special methods are required for normally-off operation to be realized.

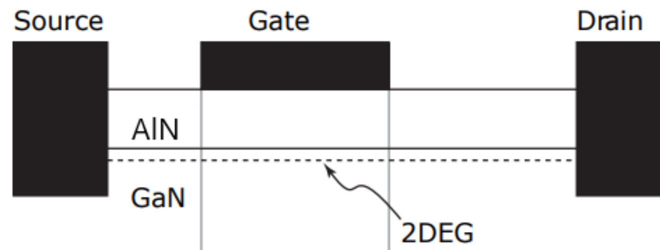

Fig. 2.6: Structure of an AlN/GaN HEMT, showing the 2DEG at the heterointerface. Adapted from [18].

The structural quality of the incorporated heterostructure bears significant effects to transistor efficiency. The buffer layer end-surface should be abrupt and uniform, i.e. with as little surface roughness as possible. Otherwise, owing to subsequent scattering effects, transport properties of the two-dimensional carrier gas deteriorate, decreasing device efficiency. For this reason, layer-by-layer growth is usually implemented. Molecular Beam Epitaxy (MBE) is a novel technique for the consistent development of heterostructures, with abrupt interfaces and precise control over their layers' thickness and composition.

HEMT surfaces also play a crucial role in material properties. Surface atoms could interact with external elements or exhibit intrinsic phenomena, such as surface recon-

struction, that alter the electronic structure of the surface. A charge will in turn affect the accumulated gas of mobile carriers. For example, the entrapment of positive charges (ionized donor-like surface states) would attract more electrons, increasing the density of the exhibited 2DEG. This phenomenon is highly relevant in polar materials, and especially in InN, where a high electron accumulation ($\sim 2.5 \times 10^{13}$ cm^{-2} [19]) is exhibited at its surface, pinning the Fermi level well within its conduction band.

Significant effort has been devoted to the the protection of semiconductor surfaces from and the control of surface states. Surface passivation refers to process of rendering semiconductor surfaces chemically inactive and electronically stable. By thin film deposition of certain materials (III-nitride cap layers, high-k dielectrics, e.g. Si_3N_4), dangling bonds at the surface can be saturated [20, 21].

References

[1] D. J. Griffiths, *Introduction to Electrodynamics.* Prentice Hall, 3rd ed., (1999).

[2] R. Resta *Ferroelectrics*, vol. **136**, pp. 51–55, (1992).

[3] R. D. King-Smith and D. Vanderbilt *Phys. Rev. B*, vol. **47**, pp. 1651–1654, (1993).

[4] O. Ambacher and V. Cimalla in *Polarization Effects in Semiconductors – From Ab Initio Theory to Device Applications* (C. Wood and D. Jena, eds.), ch. Polarization Induced Effects in GaN-based Heterostructures and Novel Sensors, p. 56, Springer Publications, (2008).

[5] G. Martin, A. Botchkarev, A. Rockett, and H. Morkoç *Appl. Phys. Lett.*, vol. **68**, no. 18, pp. 2541–2543, (1996).

[6] F. Bernardini, V. Fiorentini, and D. Vanderbilt *Phys. Rev. B*, vol. **56**, pp. R10024–R10027, (1997).

[7] A. Adikimenakis, M. Androulidaki, E. F. Salhin, K. Tsagaraki, G. Doundoulakis, J. Kuzmik, and A. Georgakilas *J. Phys.: Conf. Ser.*, vol. **1190**, p. 012010, may (2019).

[8] I. Vurgaftman and J. R. Meyer *J. Appl. Phys.*, vol. **94**, no. 6, pp. 3675–3696, (2003).

[9] J. Piprek in *Nitride Semiconductor Devices: Principles and Simulation* (J. Piprek, ed.), ch. Introduction, Wiley-VCH Verlag GmbH & Co. KGaA, (2007).

[10] T. Takeuchi, S. Sota, M. Katsuragawa, M. Komori, H. Takeuchi, H. A. H. Amano, and I. A. I. Akasaki *Jpn. J. Appl. Phys.*, vol. **36**, no. 4A, p. L382, (1997).

[11] E. T. Yu and P. M. Asbeck in *Polarization Effects in Semiconductors – From Ab Initio Theory to Device Applications* (C. Wood and D. Jena, eds.), ch. Local Polarization Effect in Nitride Heterostructures and Devices, p. 219, Springer Publications, (2008).

[12] E. Dimakis, E. Iliopoulos, K. Tsagaraki, A. Adikimenakis, and A. Georgakilas *Applied Physics Letters*, vol. **88**, no. 19, (2006). 191918.

[13] F. Bernardini, V. Fiorentini, and D. Vanderbilt *Phys. Rev. B*, vol. **63**, p. 193201, (2001).

[14] G. Koley et al. in *Polarization Effects in Semiconductors – From Ab Initio Theory to Device Applications* (C. Wood and D. Jena, eds.), ch. Polarization in Wide Bandgap Semiconductors and their Characterization by SPM, p. 56, Springer Publications, (2008).

[15] A. R. Denton and N. W. Ashcroft *Phys. Rev. A*, vol. **43**, pp. 3161–3164, (1991).

[16] E. Iliopoulos, A. Adikimenakis, C. Giesen, M. Heuken, and A. Georgakilas *Appl. Phys. Lett.*, vol. **92**, no. 19, (2008). 191907.

[17] M. Androulidaki, N. T. Pelekanos, K. Tsagaraki, E. Dimakis, E. Iliopoulos, A. Adikimenakis, E. Bellet-Amalric, D. Jalabert, and A. Georgakilas *phys. stat. solidi c*, vol. **3**, no. 6, pp. 1866–1869, (2006).

[18] D. Jena in *Polarization Effects in Semiconductors – From Ab Initio Theory to Device Applications* (C. Wood and D. Jena, eds.), ch. Polarization Effects on Low-Field Transport & Mobility in III-V Nitride HEMTs, p. 162, Springer Publications, (2008).

[19] C. G. Van de Walle, J. L. Lyons, and A. Janotti *phys. stat. sol. (a)*, vol. **207**, no. 5, pp. 1024–1036, (2010).

[20] J. Kuzmik, S. Hascik, M. Kucera, R. Kudela, E. Dobrocka, A. Adikimenakis, M. Micusik, M. Gregor, A. Plecenik, and A. Georgakilas *Appl. Phys. Lett.*, vol. **107**, no. 19, (2015). 191605.

[21] C. Zervos, A. Adikimenakis, P. Beleniotis, A. Kostopoulos, M. Androulidaki, K. Tsagaraki, M. Kayambaki, G. Konstantinidis, and A. Georgakilas *J. Vac. Sci. & Tech. B*, vol. **35**, no. 2, (2017). 021210.

3. Molecular Beam Epitaxy

Material properties, and by extension device efficiency, are highly dependent on their microstructure. For that reason, there has been significant effort devoted to the development of a consistent method to create materials with precise control over composition, doping and thickness. Molecular Beam Epitaxy (MBE) is a critical novel technique for the epitaxial growth of such high-quality thin structures of semiconductors, metals or insulators. MBE is applied in the epitaxy of III-V semiconductors to create artificial semiconductor materials that combine layers of different semiconductors, i.e. heterostructures.

In this chapter, the basic physical mechanisms behind epitaxial growth by MBE are introduced and the conditions under which MBE is realised are briefly explained. Finally, the MBE system used for this work is described.

3.1 Basic Physical Processes

Epitaxial growth by MBE involves the reaction of one or more beams of atoms or molecules with a crystalline surface under ultrahigh vacuum conditions [1]. The beams are created by evaporation or sublimation of atoms and molecules from solid sources (Ga, Al, In, Si, etc.) at high source temperatures or by using components from gas-phase sources (N_2, NH_3). The beam elements are then transported through the vacuum chamber towards the substrate, where they form a crystalline layer in registry with the substrate by bonding with the crystalline substrate atoms, i.e., an epitaxial film [2]. The integration of impinging elements into the overgrown layer is performed over a series of surface processes [3] (see Fig. 3.1):

- adsorption of the constituent atoms or molecules impinging on the substrate surface,
- surface migration and dissociation of the adsorbed molecules,
- incorporation of the constituent atoms into the crystal lattice of the substrate or the epilayer already grown, and
- thermal desorption of the species not incorporated into the crystal lattice.

Growth by MBE is conducted under conditions far from thermodynamic equilibrium and is thus governed by the kinetics of the aforementioned surface processes [3]. Incident beam species initially form weak Van der Waals bonds with the atoms of the overgrown layer. The substrate is maintained at a controlled and elevated temperature, allowing for

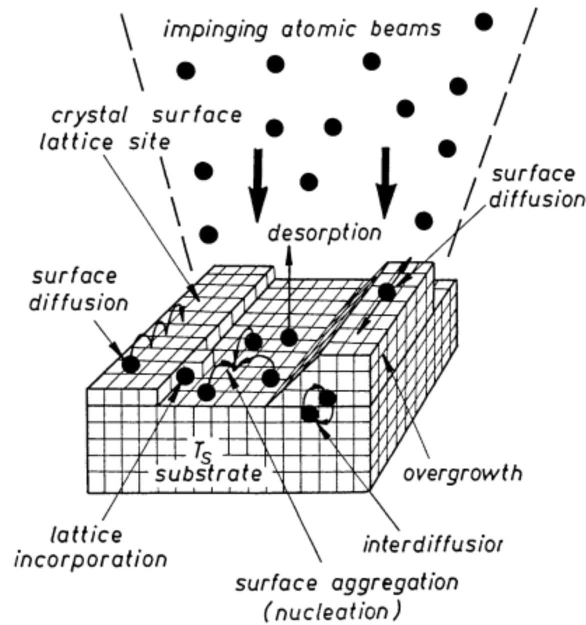

Fig. 3.1: Physical mechanisms of crystal growth by MBE. Reprinted from [3].

the transfer of thermal energy to impinging atoms. Consequently, their surface diffusion is facilitated, which can result in their integration into a lattice site or -conversely- their desorption off the substrate surface. Potential lattice sites involve atom vacancies, step edges, nucleation regions (islands), etc. [4].

Homoepitaxial growth (epitaxy on a substrate of the same material) depends on the diffusion length of atoms on the surface, before they are incorporated in the crystal. At high rate of incident atoms and low substrate temperature, the diffusivity of impinging atoms is low, which leads to the incorporation of said atoms in the crystal before they could move a few atomic sites on the surface. Consequently, crystal disorder will gradually accumulate and the deposited layer could turn amorphous.

In the case of heteroepitaxy, depending on the surface energies of epilayer and substrate materials, as well as the presence of lattice mismatch strain, three growth modes have been distinguished. The first one (Fig 3.2a) is Frank-van der Merve (FM) growth mode, whereby thin epitaxial films are grown layer-by-layer. In this strictly two-dimensional (2D) mode, each layer is fully completed before the next one begins to form. The next growth mode (Fig 3.2b) is named after Volmer–Weber (VW). Here, epitaxial growth is realised by the formation of three-dimensional (3D) islands on the substrate surface, due to nucleation of impinging atoms. These surface aggregations can keep growing independently (e.g. nanowires [5]) or gradually coalesce into a continuous film structure. Finally, Stranski–Krastanov (SK) growth is an intermediate case between FM and VM (Fig 3.2c). SK growth starts with a layer-by-layer (2D) growth mode for a few monolayers,

but then transforms to a 3D growth mode.

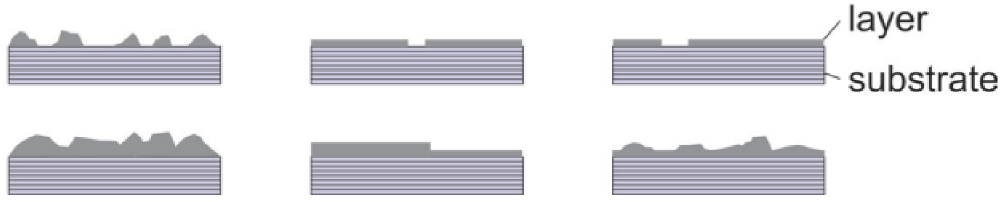

Fig. 3.2: Modes of growth (left to right): Volmer-Weber; Frank-van der Merwe; and Stranski-Krastanov. Reprinted from [6].

The observed growth mode is highly dependent on the growth conditions. Since surface kinetics govern the MBE growth mechanisms, it is expected for substrate temperature to hold a significant role during growth. Crystal growth comes down to saturation of dangling bonds, so the flow of reactant species heavily influences the preferable mode as well. Surface orientation may also bear an effect on which mode is energetically favorable.

3.2 Plasma-Assisted MBE

Plasma-Assisted MBE (PA-MBE) is a critical MBE technique that employs a remote compact plasma source to produce a beam of reactive nitrogen species from a source of inert N_2 gas [7]. The growth of III-V nitride semiconductors is based upon the following synthesis reaction:

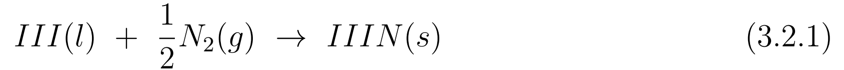

$$III(l) \;+\; \frac{1}{2}N_2(g) \;\rightarrow\; IIIN(s) \qquad (3.2.1)$$

However, this reaction is not favorable under typical MBE growth conditions, because molecular nitrogen is inert, i.e. its energy is insufficient for it to surpass the Gibbs free energy barrier of III-N bonds and be incorporated into the epilayer. Therefore, the use of energetic nitrogen plasma species has been proposed. Activated species involve N_2^* ($A^3\Sigma_u^3$, $B^3\Pi_g$, $a^1\Pi_g$, $C^3\Pi_u$), N_2^+ ($^2\Sigma_g^+$) and N (^4S, ^2P, ^2D) [8].

Each nitrogen plasma species may affect the growth process differently [7]. Therefore, composition-monitoring techniques must be employed to determine the nature of the nitrogen beam.

Major examples of nitrogen plasma sources include an Electron Cyclotron Resonance (ECR) microwave source [9] or a Radio-Frequency (RF) source [10]. The latter holds some advantages over the former; provides higher growth rates, operates at higher vacuum conditions and includes lower molecular ion content [7]. A correlation of optical emission spectra of the nitrogen plasma with GaN growth rate suggests that mainly excited nitrogen molecules contribute in GaN growth [10]. RF-MBE is conducted for this work, employing a RF plasma source.

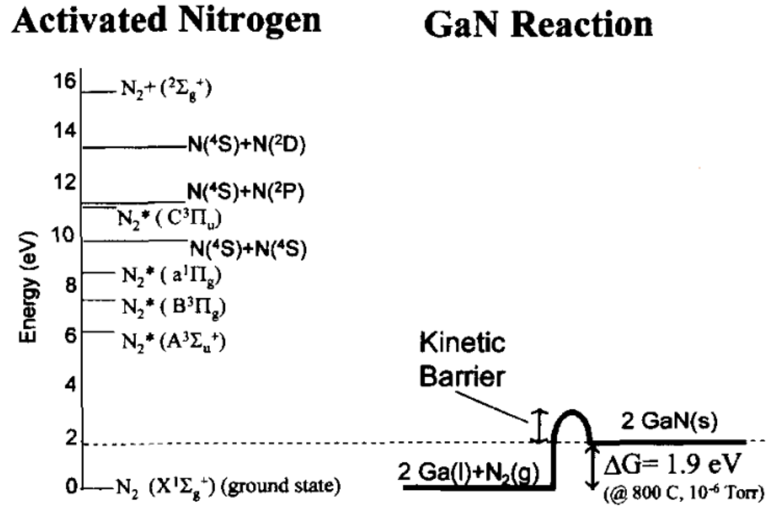

Fig. 3.3: Comparison of the potential energy of activated nitrogen with Gibbs free energy of the GaN synthesis reaction. Reprinted from [8].

3.3 Growth Conditions

Growth conditions are responsible for setting the environment for high-quality crystal development. Vacuum quality, beam fluxes, substrate temperature are all defining parameters for each growth mechanism, and therefore influence growth rate and mode (two- vs. three-dimensional growth).

3.3.1 Vacuum Conditions

Molecular Beam Epitaxy is realised under ultra-high vacuum conditions. They key feature of MBE is the flow of elements towards the substrate with high directivity. If vacuum conditions are inadequate, the atomic beams may encounter residual gas molecules, on their way to the substrate. Such scattering processes degrade the beam nature of the mass flow.

Therefore, the mean free path - or the average distance traversed between successive collisions- of the reactant beam must be greater than the distance between the beam sources and the substrate. Considering the gas inside the growth chamber as a mixture of the beam and the residual gas, the relation between the mean free path (denoted λ) and residual gas pressure can be derived [11].

$$\lambda^{-1} = \sqrt{2}\pi n_b d_b^2 + \sqrt{2}\pi n_g d_{bg}^2 \sqrt{1 + v_g^2/v_b^2} \tag{3.3.1}$$

with

$$d_{bg} = \frac{d_b + d_g}{2}$$

where n_i, d_i, v_i are the concentration, diameter and average velocity of the molecules. The subscripts b and g correspond to the molecular beam and the residual gas, respectively. Taking into account that the residual gas velocities are typically much smaller that those of the molecular beams ($v_g \ll v_b$), the velocity ratio term can be omitted.

For an ideal gas, it holds true that $n = p/k_B T$, where p is pressure, k_B is the Boltzmann constant ($k_B = 1.381 \times 10^{23} JK^{-1}$) and T is temperature. Substituting this into Eq. 3.2.1, the partial pressure of the residual gas can be obtained [3, 11]:

$$p_g = k_B T \frac{\lambda^{-1} - \sqrt{2}\pi n_b d_b^2}{\pi d_{bg}^2} \tag{3.3.2}$$

A typical distance between beam sources and substrate is 20-30 cm, so by Eq. 3.3.2, a pressure of 10^{-4} $Torr$ ($T = 300K$, $d_{b,g} \sim 3$ Å, $n_b \sim 10^{16} m^{-3}$) is barely sufficient for successful growth by MBE.

Evidently, the beam nature of impinging elements can be preserved in high vacuum conditions. Nevertheless, further vacuum restrictions are imposed if impurity integration in the overgrown layer is to be considered. Each constituent species - e.g. C, H, O - of the residual gas may collide with the substrate, resulting in unintentional impurity concentrations in the crystallized epilayer. The rate w_i of an incident species i per unit surface can be expressed as a function of its partial pressure p_i, its molecular weight M_i and the residual gas temperature T [12]:

$$w_i = p_i \sqrt{\frac{N_A}{2\pi k_B M_i T}} \tag{3.3.3}$$

where $N_A = 6.02 \times 10^{22}$ is the Avogadro constant. Usually, the residual gas pressures inside the growth chamber are maintained at around $10^{-9} - 10^{-10}$ Torr. In most cases, pressure during growth is maintained at approximately 10^{-7} Torr.

3.3.2 Substrate Temperature

Substrate temperature is one the most crucial parameters in growth by MBE. It is used to control the growth kinetics and optimize the quality of the grown epilayers. The diffusion of impinging atoms along the substrate surface is strongly dependent on the substrate temperature. By maintaining the substrate at an elevated temperature, the diffusivity of the beam elements is increased, facilitating their interactions with potential lattice sites and in turn their integration into the crystal. However, too high substrate temperatures can push the epilayer growth rate towards the opposite direction. As previously mentioned, arriving atoms have a finite probability of acquiring sufficient energy to overcome the barrier set by the attractive forces and leave the substrate. The desorption rate of

impinging atoms increases with temperature. This means that an increased temperature reduces their time spent on the overgrown layer and thus shrinks their temporal window to be absorbed into a lattice site. Of course, the reduction of atoms adhering to the substrate is equivalent to a slower growth rate. What is more, high temperatures can lead to the sublimation of already integrated crystal atoms, further reducing the epilayer growth rate. Therefore, temperature control is of pivotal significance for epitaxial growth. It must be appropriately and constantly monitored to maintain a balance between the aforementioned competing processes, which maximizes the growth rate.

3.3.3 Beam Fluxes and III/V Flux Ratio

Another important aspect of successful MBE growth is the control of arrival rates of epilayer-constituent atoms. The beams are created using Knudsen's evaporation technique [13], in which evaporation occurs as effusion from an isothermal enclosure with a small aperture. This apparatus, called Knudsen (Effusion) Cell or K-cell, is further discussed in subsection 3.5, where the MBE system used for this work is described. Considering the effusion cell's orifice of area A, the total number atoms of vaporized material escaping the cavity per unit time is [1]:

$$\Gamma = pA\sqrt{\frac{N_A}{2\pi M k_B T}} \tag{3.3.4}$$

where p is the pressure inside the effusion cell, M is the atomic mass of the evaporated species and T is temperature of the cell.

By controlling the beam fluxes during growth, one can properly manipulate the ratio of incoming group-III elements to nitrogen, which is a crucial parameter when developing III-V nitride structures. The III/V ratio is a defining factor for the growth mode exhibited during epitaxy [7]. Under III-rich conditions (III/V flux ratio$>$1), growth is usually two-dimensional, resulting in smooth and uniform overgrown surfaces. III-rich growth is usually accompanied by the formation of pure III-metal atomic adlayers or, if III/V$\gg$1, metal droplets on the substrate surface [14]. On the other hand, N-rich conditions (III/V flux ratio$<$1) facilitate 3D island formation and thus a three-dimensional growth mode prevails. It must be noted that substrate temperature significantly affects the aforementioned processes. Through temperature, diffusivity, and desorption and decomposition rates can be controlled. For example, an extremely high III/V ratio can be countered by a high temperature that limits the adsorption of III-metal atoms on the substrate. In general, the growth of III-V nitride semiconductors is usually realised under metal-rich conditions, since they facilitate the diffusion of impinging atoms and in turn improve crystal quality [15, 16]. Regarding RF-MBE, the flux of the group-III elements is controlled by the temperature of the respective Knudsen cells, while the arriving rate of the nitrogen is

controlled by the operation settings of the RF plasma source.

3.4 Lattice Dislocations

The thermodynamics of epitaxial layers depend on the coherency of those with their underlying substrate [17]. During epitaxy, a solid film is grown on a crystalline substrate in which the atoms of the overgrown layer mimic the arrangement of the substrate atoms.

The most common crystallographic defects in III-V nitride semiconductors are lattice dislocations. Lattice dislocations are linear defects that contain an abrupt change in the arrangement of atoms. They can be fully described by the dislocation line vector $\vec{L}$ and the Burgers vector $\vec{b}$. The former points in the local direction of the dislocation line, and the latter is defined as the distance and direction of atomic displacement necessary for the dislocation to be formed. There are two main types of lattice dislocations: edge and screw (Fig. 3.4). In edge dislocations, the burgers vector is perpendicular to the line vector, while in screw dislocations the two vectors are parallel to each other. Edge dislocations contain the removal from or the introduction to the crystal of a half-plane of atoms. Consequently, the surrounding planes are deformed around the edge of the half-plane so that the crystal structure is perfectly ordered on either side. Screw dislocations occur when consecutive atomic half-planes {hkl} are displaced towards the [hkl] direction, by a distance that is equal to the distance between successive planes. Dislocations found in real materials are typically of mixed character, meaning that they contain characteristics of both. When lattice dislocations run though the entire overgrown layer they are also called threading dislocations.

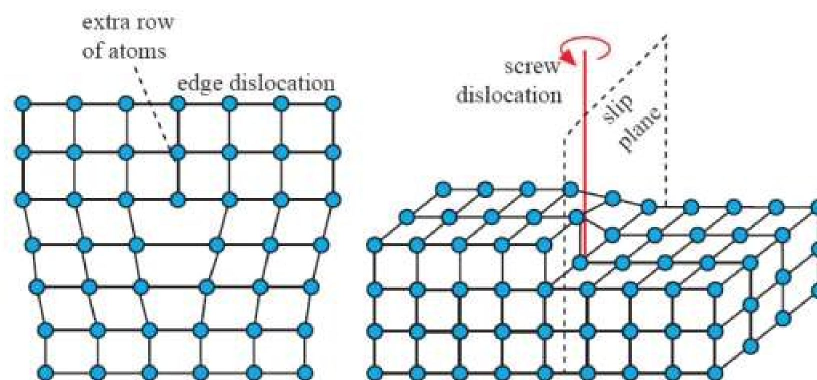

Fig. 3.4: Schematic diagrams of an edge (left) and a screw (right) dislocation. Reprinted from [18]

3.4.1 Lattice Mismatch

In heteroepitaxy, the most crucial problem epitaxial growth needs to face is strain in the overgrown layers caused by lattice mismatch between the substrate and epilayers. The development of heterostructures, i.e. layered crystal compounds of different materials, is always faced with the incoherence of constituent elements. The extent to which combined materials have (in)compatible crystals for heteroepitaxy can be quantified by what is called the lattice mismatch. It is important to note that a difference in thermal expansion coefficients could affect the structural integrity of the heteroepitaxial layers after growth completion and mateial cooling to room temperature.

By default, in heterostructures the equilibrium in-plane lattice constants of the overgrown layer a_{epi} is different from that of the substrate, a_{sub}. The lattice mismatch is defined as:

$$f = \frac{a_{sub} - a_{epi}}{a_{epi}} \tag{3.4.1}$$

When lattice mismatch occurs, it is accommodated by strain and/or structural defects in the layer. A thin epilayer can be pseudomorphically grown until a certain critical thickness. The deformed overlayer is subjected to a (biaxial) strain field, which holds the grown crystal structure in registry with the substrate. As the epilayer growth continues, the occurrence of lattice defects might be favorable over the increasing elastic energy in a pseudomorphic structure. Big lattice mismatch means that the combined materials are very incompatible or equivalently, their coherent growth is quickly (after a few atomic layers [19]) followed by the introduction of relaxation mechanisms. Such is the case for InN when grown on GaN or AlN substrates, with the lattice mismatch being $\sim 11\%$ and $\sim 14\%$, respectively.

3.4.2 Stain Relaxation Mechanisms

The overgrown layer can assume its equilibrium lattice constant (strain relaxation) through either elastic or plastic strain relaxation mechanisms.

The former entail the gradual -natural- restoration of the epilayer's pure-phase characteristics. Elastic relaxation mechanisms accompany the Volmer-Weber or Stranski-Krastanov growth modes, resulting in the formation of 3D islands, where the structure is not spatially restricted.

Plastic relaxation mechanisms permanently deform the epitaxial structure. The stress caused by the lattice misfit can be released by forming a network of regularly spaced misfit dislocations at the epilayer/substrate interface [20]. Misfit dislocations are edge dislocations and are defined as lines of disregistry of the equilibrium atomic arrangement at the interface between the substrate and the overgrown layer. After a critical epilayer

thickness, the deformation energy due to pseudomorphic growth is greater than the defect formation energy. Consequently, misfit dislocations could arise and the epilayer assumes its natural lattice constant.

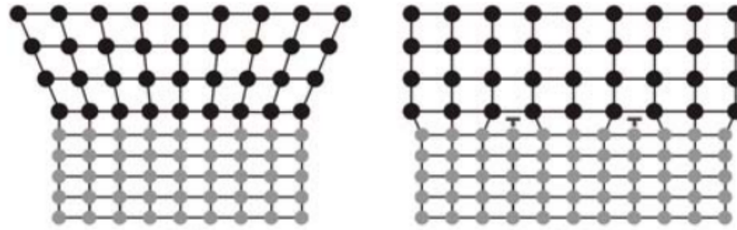

Fig. 3.5: Elastic (left) and plastic (right) relaxation mechanisms in lattice mismatched heterostructures. Reprinted from [21].

3.5 Experimental PA-MBE Arrangement

The epitaxial-growth experimental arrangement used for this work is RIBER 32 MBE system, equipped with an Oxford HD25 RF nitrogen plasma source (see Fig. 3.6). The system consists of a load, a transfer and a growth chamber. The chambers are seperated by gate valves and completely isolated from each other. By the utilization of independent vacuum forming and measuring systems at each chamber, distinct vacuum conditions can be preserved at each one. This way, the exposure of the growth chamber to increased ambient pressure is limited during sample loading. The samples are moved through these chambers on a rail by a cassette of multiple holders, thus allowing multiple sample loading.

3.5.1 Load Chamber

The load chamber is the first checkpoint of the epitaxial growth process. A mechanical and a turbomolecular pump are used to evacuate the load chamber and maintain the pressure around 10^{-8} Torr. Our loading system incorporates an additional entry room to limit the load chamber's exposure to atmospheric pressure. Consequently, chamber contamination is limited and evacuation time is reduced. During loading and unloading, the pressure inside the entry room is increased by admitting nitrogen gas before exposing it to air. The load chamber is also equipped with a substrate heating stage for its outgassing (or degassing). By controlled sample heating, adsorbed contaminants are desorbed off the surface. Cleaning temperatures depend on the sample at hand and potential species of contamination.

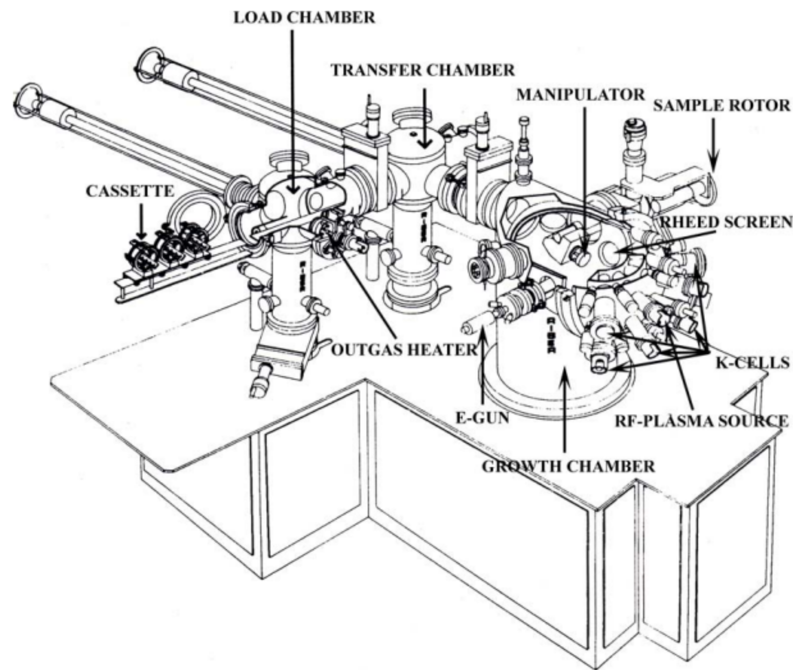

Fig. 3.6: Schematic illustration of a 32-Riber PA-MBE production system.

3.5.2 Transfer Chamber

Once ready, the sample moves onto the transfer chamber. Evacuation is realized by ion and Ti sublimation pumps, which sustain ultra high vacuum conditions (10^{-11} Torr). The transfer chamber serves as an intermediate station between load and growth chambers. This helps preserve vacuum conditions in the growth chamber and limits its contamination.

3.5.3 Growth Chamber

The final chamber of MBE is the growth chamber. The growth chamber comprises a manipulator, Knudsen cells (or K-cells), a nitrogen RF plasma source and a RHEED system (discussed in the following chapter). The combinatorial operation of turbomolecular pump, ion and Ti sublimation pumps is employed for the evacuation of the growth chamber. Additionally, the growth chamber's walls are hollow and filled with liquid nitrogen (cryopanels). Consequently, residual gas molecules can be adsorbed on said panels, further improving vacuum conditions. Pre-growth pressure is usually maintained at 10^{-11} Torr, whereas during growth there is an pressure increase to mid 10^{-6} Torr. Finally, the chamber is spherical with its entry and K-cells on opposite ends. The spherical shape enables the near identical nature of the various beams striking the overgrown layer, which facilitates growth control and homogeneity.

Inside the growth chamber, the substrate wafer is positioned on a sample-holding

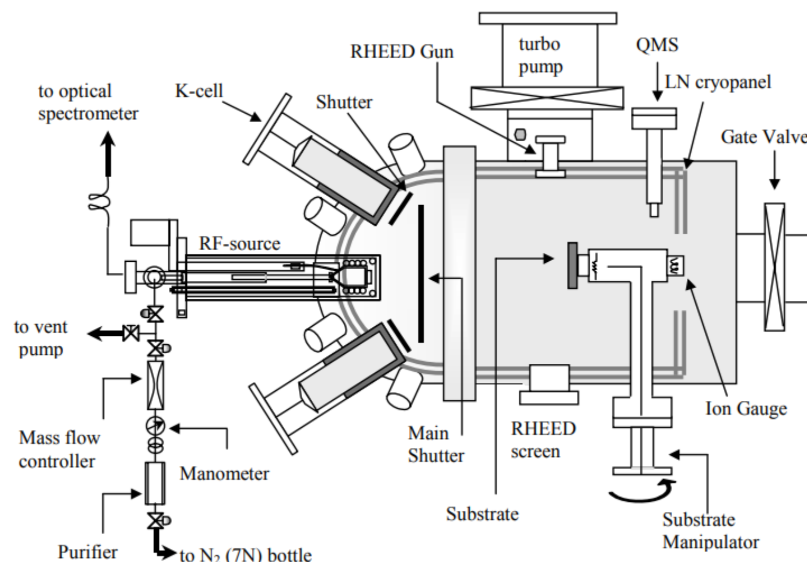

Fig. 3.7: Schematic illustration of the growth chamber and its constituent parts. Reprinted from [7].

apparatus, called manipulator. The manipulator can be turned between the chamber entry and the K-cells. Utilizing a mechanical arm, the sample is carried over from the transfer chamber and placed on the manipulator. The latter is then rotated to face the K-cells. The manipulator can also be axially rotated, in order to facilitate uniform beam arrival and homogeneous growth conditions along the sample surface. What is more, the manipulator is attached to a thermocouple in order to control growth temperature. Finally, an ion gauge is positioned behind the manipulator. It is used to both monitor the pressure during growth and to calibrate the flux of the molecular beams. As analyzed above, the flux of impinging species is controlled by the K-cell temperature and be expressed in terms of its partial pressure. The ion gauge's peculiar positioning stems from the need to limit the deposition of impinging elements on the manipulator's sample-holding side, during the aforementioned calibration.

The atomic beams of group-III elements (In, Al, Ga) are generated by the Knudsen cells. The K-cells, as previously mentioned, are isothermal crucibles with a small orifice. Fig. 3.9 demonstrates a typical K-cell. The cell is attached to the MBE growth chamber by its flange, from where a couple of support rods lead to its main body. The latter consists of a crucible, heating filaments and a thermocouple; all surrounded by a protective thermal shield. The crucible is made of pyrolytic boron nitride (PBN), which is most suitable for the sublimation of group-III elements due to the limited chemical reactivity between the two. Said sublimation is realised by heating the crucible (through the filaments). The conical shape of the isothermal enclosure ensures proper beam directivity and dispersion

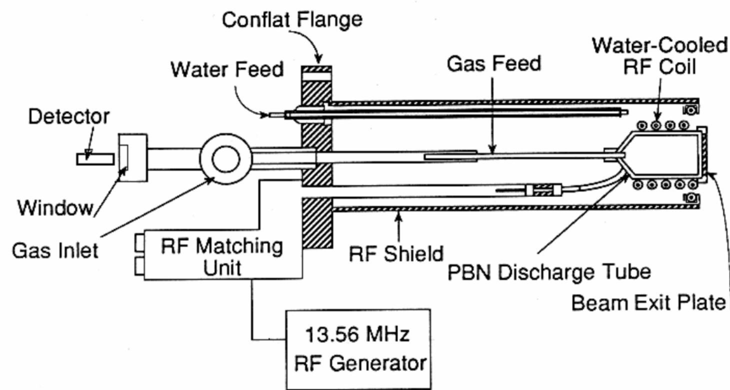

Fig. 3.8: Schematic drawing of the Oxford Applied Research HD25 RF plasma source.

which in turn improve growth rate and homogeneity on the substrate surface. In order to further improve growth uniformity, the substrate is also set to constant rotation.

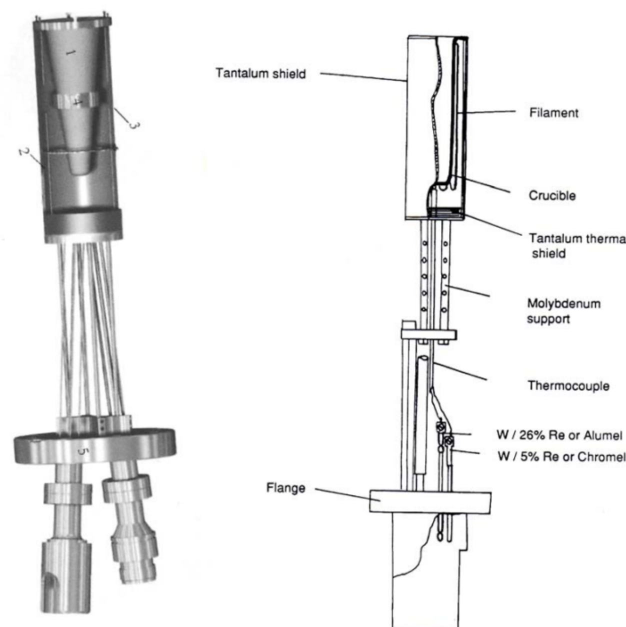

Fig. 3.9: A *Veeco* Knudsen cell used in MBE (left) and its schematic illustration (right). (1) PBN crucible, (2) heating filament, (3) tantalum thermal shield, (4) thermocouple attachment point, and (5) flange. Reprinted from [22].

The provision of energetic nitrogen in the epilayer is accomplished by a radio-frequency (RF) plasma source. Nitrogen is introduced into an PBN tube wrapped with a water-cooled copper coil. By Faraday's law, RF energy at 13.56 MHz is inductively coupled through the coil to create the plasma. The PBN discharge tube is capped with an exit plate, with multiple small orifices allowing the exit of nitrogen reactive species, while a stable plasma is preserved within the PBN tube. The RF source operates with a typical maximum power of 600 W into a 50-Ω load.

References

[1] A. Y. Cho in *The Technology and Physics of Molecular Beam Epitaxy* (E. H. C. Parker, ed.), Plenum Press, (1985).

[2] J. R. Arthur *Surface Science*, vol. **500**, (2002).

[3] M. A. Herman and H. Sitter, *Molecular Beam Epitaxy: Fundamentals and Current Status.* Springer-Verlag, 2nd ed., (1996).

[4] B. Lewis and J. C. Anderson, *Nucleation and Growth of Thin Films.* New York: Academic, (1978).

[5] G. Doundoulakis et al. *Nanotechnology*, vol. **30**, no. 28, p. 285304, (2019).

[6] M. Zhong, *Epitaxy.* Rijeka: IntechOpen, (2018).

[7] A. I. Georgakilas, H. M. Ng, and P. Komninou in *Nitride Semiconductors - Handbook on Materials and Devices* (P. Rutennara, M. Albrecth, and J. Neugerbauer, eds.), ch. Plasma-Assisted Molecular Beam Epitaxy of III–V Nitrides, Weinheim, Germany: Wiley-VCH, (2003).

[8] N. Newman *J. Cryst. Growth*, vol. **178**, no. 1, pp. 102–112, (1997).

[9] T. Moustakas, T. Lei, and R. Molnar *Physica B: Cond. Matt.*, vol. **185**, no. 1, pp. 36–49, (1993).

[10] E. Iliopoulos, A. Adikimenakis, E. Dimakis, K. Tsagaraki, G. Konstantinidis, and A. Georgakilas *J. Cryst. Growth*, vol. **278**, no. 1, pp. 426–430, (2005).

[11] S. Dushmann, *Scientific Foundations of Vacuum Techniques.* New York: Wiley, (1934).

[12] L. B. Loeb, *The Kinetic Theory of Gases.* New York: McGraw-Hill, 2nd ed., (1934).

[13] M. Knudsen and W. J. Fisher *Phys. Rev. (Series I)*, vol. 31, pp. 586–588, (1910).

[14] J. E. Northrup, J. Neugebauer, R. M. Feenstra, and A. R. Smith *Phys. Rev. B*, vol. **61**, pp. 9932–9935, (2000).

[15] E. J. Tarsa, B. Heying, X. H. Wu, P. Fini, S. P. DenBaars, and J. S. Speck *J. Appl. Phys.*, vol. **82**, no. 11, pp. 5472–5479, (1997).

[16] F. Widmann, B. Daudin, G. Feuillet, N. Pelekanos, and J. L. Rouvière vol. **73**, no. 18, pp. 2642–2644, (1998).

[17] J. Tsao, *Materials Fundamentals of Molecular Beam Epitaxy.* Elsevier Science, (2012).

[18] D. McNamara. PhD thesis, (2009).

[19] E. Dimakis, E. Iliopoulos, K. Tsagaraki, T. Kehagias, P. Komninou, and A. Georgakilas *J. Appl. Phys.*, vol. **97**, no. 11, (2005). 113520.

[20] J. Matthews and A. Blakeslee *J. Crys. Growth*, vol. **27**, pp. 118–125, (1974).

[21] E. Dimakis. PhD thesis, (2007).

[22] A. Adikimenakis. PhD thesis, (2009).

4. Characterization Techniques

Characterization techniques refer to experimental methods for the investigation of the structural, electronic and optical properties of materials and devices. Through those, the chemical composition, structure and surface morphology, defects, dislocations, as well as mobile carrier concentrations and mobilities can be determined.

A critical advantage of the MBE experimental arrangement is the ability to oversee and analyze the growth process by several in situ diagnostic techniques. Typical examples include Reflection High-Energy Electron Diffraction (RHEED) [1], Auger electron spectroscopy (AES) [2] and Secondary Ion Mass Spectroscopy (SIMS) [3, 4].

Material properties are also investigated by a plethora of ex situ evaluation techniques. Structural characterization techniques include, but are not limited to, Scanning or Transmission Electron Microscopy (SEM, TEM) [5, 6], Atomic Force Microscopy (AFM) [7] and X-Ray Diffraction (XRD) [8]. Photoluminescence (PL) spectroscopy [9] is used to study the optoelectronic properties of the layers. Electrical properties are usually investigated by Hall Effect measurements [10], and Capacitance-Voltage (C-V) or Current-Voltage (I-V) characterization of test devices [11].

This chapter is a brief overview of the in-growth and post-growth characterization techniques used for this work. These are RHEED, AFM and Hall-Effect measurements.

4.1 Reflection High-Energy Electron Diffraction

As already discussed, the key feature of MBE is the precise dimensional and compositional control over material microstructure on an atomic level. This precision, however, would be infeasible without an adequately accurate characterization technique, that is compatible with the growth process.

Reflection High-Energy Electron Diffraction provides structural information in real time for the surface atomic planes, while simultaneously not disturbing the flow of molecular beams toward the overgrown layer [12]. This is the reason behind the ubiquitous application of RHEED in MBE systems.

As the name suggests, RHEED is based on the diffraction of an electron beam from a crystalline arrangement (Fig. 4.1). The beam is produced by electric-field acceleration of electrons emitted from a heated filament (RHEED gun) and is directed to the substrate surface at a low angle ($1^o - 3^o$). The fundamental principle behind RHEED [1] is the condition that difference between the wave vectors $\vec{k_0}$ and $\vec{k'}$ of the incident and diffracted

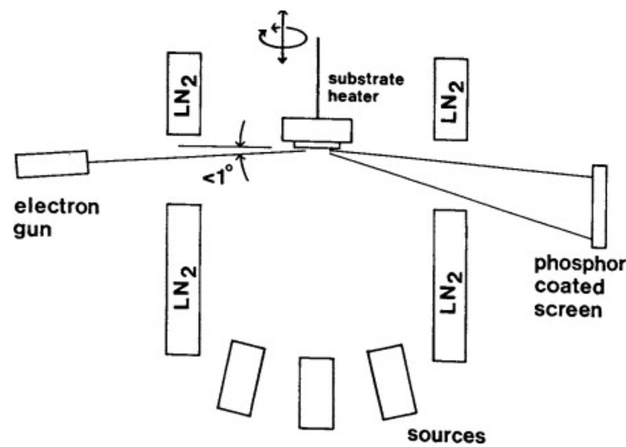

Fig. 4.1: Experimental arrangement of the electron gun, sample and fluorescent screen of a RHEED system. Reprinted from [13].

beams, respectively, is equal to the reciprocal-lattice vector $\vec{G}$:

$$\vec{k'} - \vec{k_0} = \vec{G} \tag{4.1.1}$$

where the reciprocal-lattice vector $\vec{G}$ is related to any lattice position vector $\vec{R}$ by [14]:

$$\vec{G} \cdot \vec{R} = 2\pi n \ , \ n \in \mathbb{Z} \tag{4.1.2}$$

Considering elastic scattering, i.e. ignoring the loss of energy of the primary beam, the absolute magnitude of momentum is unchanged, that is $|\vec{k_0}| = |\vec{k'}|$. Attaching $\vec{k_0}$ to a reciprocal lattice point, the sphere around it with radius $|\vec{k_0}|$ is defined as the Ewald Sphere [15]. Reflection occurs for those $\vec{k'}$ that connect the origin of the sphere with a reciprocal lattice point on the sphere. Due to the narrow angle between the substrate surface and the incident electron beam, the diffraction of the latter is realised over very few atomic layers beneath the surface. Approximately, the electron beam is reflected by a two-dimensional atomic net and the periodic part of the crystal beneath the surface is neglected. Omitting the third real space dimension, the respective reciprocal space dimension is undefined [16]. The corresponding two dimensional reciprocal lattice then consists of parallel rods perpendicular to the surface.

The magnitude of the wave vector for high energy electrons, accelerated by a potential V is equal to:

$$k_0 = \frac{1}{\hbar}\sqrt{2m_0qV + \frac{q^2V^2}{c^2}} \tag{4.1.3}$$

where m_0 and q are the electron rest mass and charge, respectively, $\hbar$ is the reduced Plank constant and c is the speed of light. After being reflected on the substrate surface, the scattered electron beams are projected on a fluorescent screen.

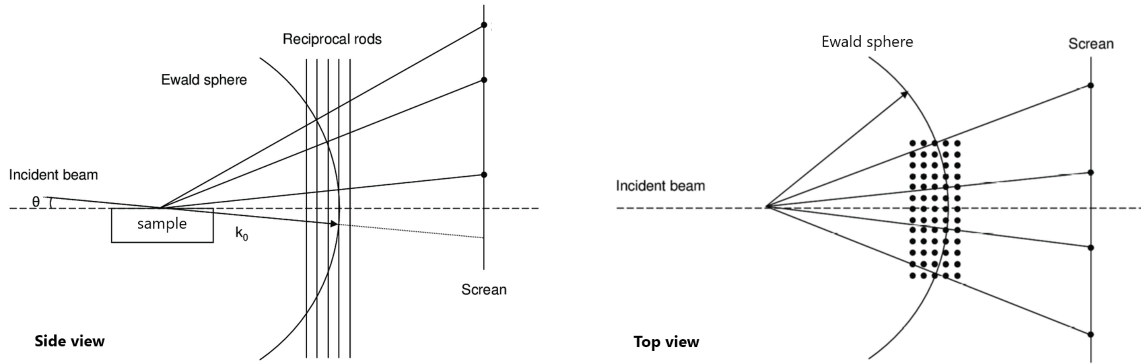

Fig. 4.2: Ewald sphere construction and diffraction geometry of RHEED [1].

Electron reflection on a smooth surface leads to patterns constituted by elongated streaks which are normal to said surface [1]. The radius of the Ewald sphere is greatly larger than the distance between reciprocal lattice rods, resulting in the Ewald sphere being cut by multiple reciprocal lattice rods. For a number estimate, the distance between successive reciprocal space rods is usually equal to $1-2$ $\mathring{A}^{-1}$ [12], while for an acceleration voltage $V = 12$ keV (as used for this work), the magnitude of the incident wave vector is $k_0 \approx 52.5$ $\mathring{A}^{-1}$ [12]. Additionally, the Ewald sphere has a finite thickness, due to electron energy spread and to beam convergence, and the rods have finite thickness due to lattice imperfections and thermal vibrations [1]. Consequently, each intersection between the sphere and a rod occurs in a (continuous) series of points along the rod. As a result the incident electron beam will degenerate into parallel streaks, which are naturally perpendicular to the substrate plane.

However, the diffraction process in RHEED is generally not a true reflection [12]. Most overgrown surfaces are rough, i.e. they exhibit atom vacancies, adatoms, lattice step edges nucleation regions (islands), etc.. In this general case, the diffraction pattern is produced in transmission through the surface asperities. The emergent RHEED image is spotty, with each spot corresponding to a reciprocal lattice site.

During the growth of an epilayer, if growth is realized through a layer-by-layer growth mode, wherein 2D islands nucleate and coalesce, the RHEED image will oscillate in intensity. When the first few atoms are deposited onto a smooth substrate surface, said surface will roughen. The occurring surface asperities will act as additional scattering centers, reducing the intensity of pattern features. As lattice sites of an atomic plane are filled with impinging beam atoms, i.e. the surface flatness is recovered, the RHEED pattern intensity increases.

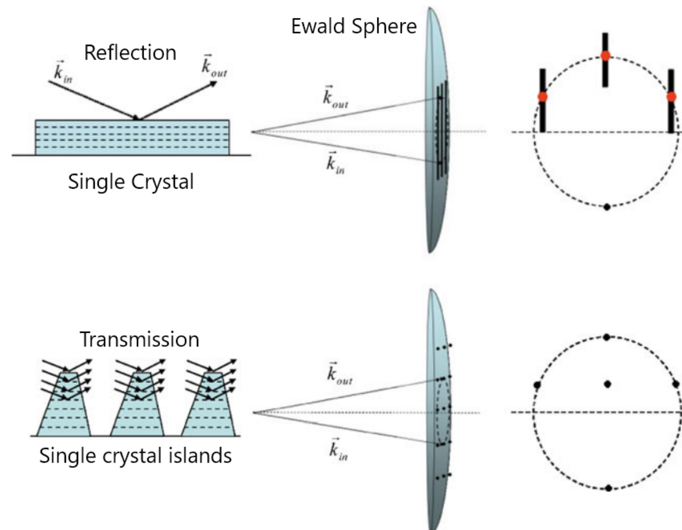

Fig. 4.3: Schematics of electron scattering geometries, film morphologies, and crystalline structures for single crystal and single-crystal islands. Corresponding Ewald sphere constructions and RHEED patterns are shown. Adapted from [17].

4.2 Atomic Force Microscopy

Atomic Force Microscopy (AFM) is a powerful post-growth characterization technique that can image almost any type of surface with atomic resolution perpendicular to the surface. Introduced by Binnig et al. [19], AFM incorporates a probe (tip), positioned at the end of a cantilever, and an optical system using a laser to detect the tip's deflections, as shown in Fig. 4.5. When the tip is brought into proximity with the sample and moved along its surface, forces between the two result in the tip's vertical displacement and thus the deflection of the cantilever. The laser, being reflected on the latter, deviates and allows the topographic profiling of the sample. The tip radius is typically on the order of nanometers, allowing a spatial resolution down to the atomic level.

There are various scanning modes used in AFM studies. Popular working modes include contact, non-contact and tapping mode (see Fig. 4.6). Each mode entails its own advantages and disadvantages over other operation techniques and it is up to the research to choose the appropriate one for each occasion.

Contact mode is the basis of most AFM systems [7]. The tip is constantly in physical contact with the sample. The cantilever deflection induced by surface topography is maintained at a preset load force by a feedback loop, whose response is used to obtain a topographic image.

In non-contact mode, the AFM probe is set to an oscillatory motion slightly above the substrate [21]. In this case, the quantity generally measured is the force interaction between the tip and the surface. The topographic analysis is realised by measuring either

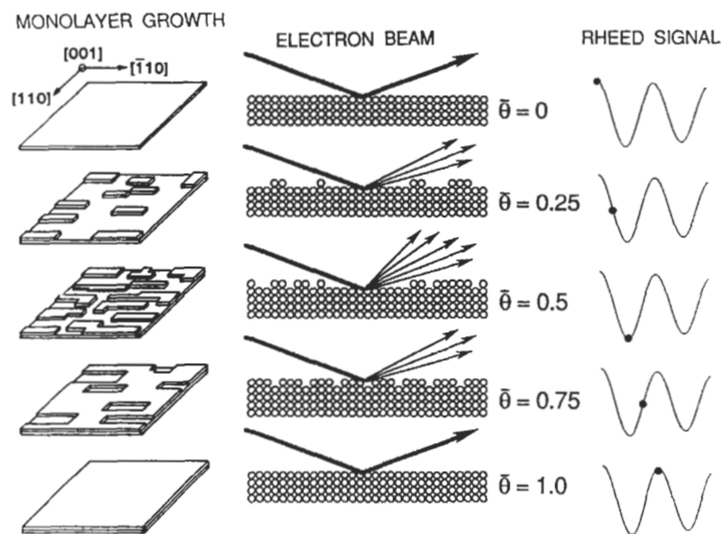

Fig. 4.4: Real space representation of the formation of a single complete monolayer in layer-by-layer growth through 2D island nucleation. $\bar{\theta}$ is the fractional layer coverage. Reprinted from [18].

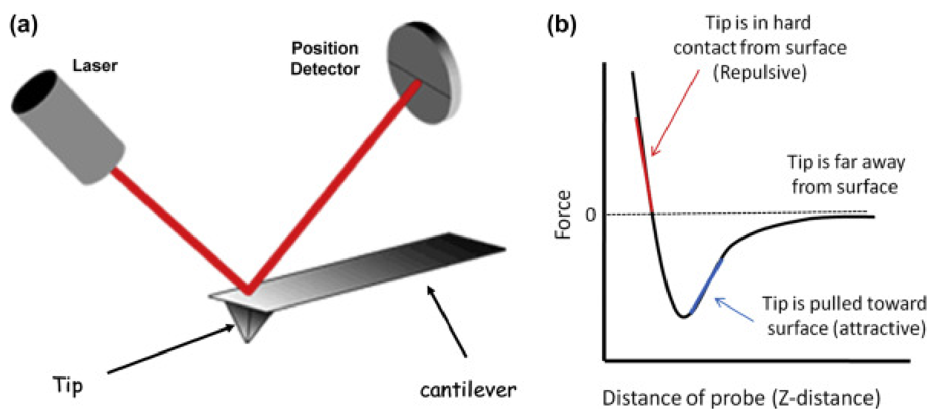

Fig. 4.5: (a) Principle of atomic force microscope (AFM) imaging, (b) variation of interaction force versus distance between the AFM tip and substrate. Reprinted from [20].

the change in oscillation amplitude at a constant frequency near resonance (amplitude modulation) or the change in resonant frequency, implementing a feedback loop that maintains the cantilever on resonance (frequency modulation).

In tapping mode, the cantilever again vertically oscillates near resonance frequency [21]. Consequently, the tip is brought into contact with the sample only at the downward end of its periodic displacement. The topographic image is generated by monitoring the deviations in amplitude of the cantilever's oscillatory motion. Additionally, due to limited tip-sample interaction, i.e. they withstand limited lateral forces, this AFM working mode is less destructive to both.

Beyond surface analysis, AFM can be employed for electrical, mechanical, and chemical characterization by force spectroscopy, i.e. measuring the forces generated between the

Fig. 4.6: Schematic illustration of typical AFM scanning modes. Reprinted from [21].

tip and the sample surface as a function of their mutual distance (Fig. 4.5b), as well as for engineering of material properties by surface manipulation.

4.3 Hall Effect Measurements

Since its discovery, the Hall effect [22], in combination with conductance measurements, has been a crucial means for the determination of semiconductor electrical properties (carrier type, concentration and mobility). The Hall Effect refers to the production of a potential difference, called Hall voltage (V_H), along a (semi)conductor traversed by an electric current when subjected to a magnetic field perpendicular to said current. The direction of the potential difference is perpendicular to both the magnetic field and the current.

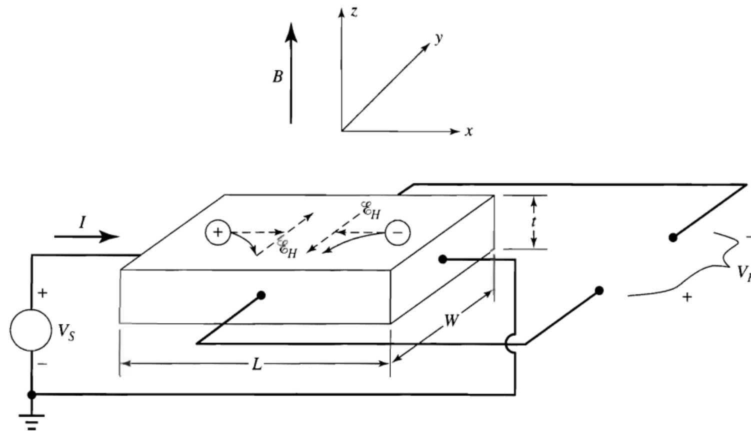

Fig. 4.7: Schematic of the Hall effect. A current flows along the positive x-direction. A magnetic field B along the positive z-direction deflects holes and electrons along the negative y-direction. The polarity of V_H depends of the material's conductivity type. Reprinted from [23].

In essence, mobile carriers are subjected to the Lorentz force:

$$\vec{F} = q(\vec{E} + \vec{v}_d \times \vec{B}) \tag{4.3.1}$$

where q is the electron charge, E is the applied electrostatic field, v_d is the carrier drift

velocity and B is the applied magnetic field. By expanding Eq. 4.3.1, one can notice that carriers are no longer restricted to moving along the x-axis. Due to the applied magnetic field, considering $\vec{B} = B\hat{z}$, carriers deflect along the y-direction. Subsequently, charge accumulates at the respective sides of the conductor and a y-component of the electric field is established. This charge-induced field can be related to a potential difference along said axis, which is defined as the Hall voltage.

In order to understand this technique, it is meaningful to first define some important magnitudes. Resistivity is defined as:

$$\rho = \frac{1}{q(\mu_n n - \mu_p p)} \tag{4.3.2}$$

where q is the electron charge, n and p are the electron and hole concentrations, respectively, and $\mu_{n/p}$ are the corresponding carrier mobilities. For simplicity, let us consider a material whose majority mobile carriers are electrons ($n \gg p$). The complementary equations for holes can be similarly derived. Eq. 4.3.2 can then be simplified into:

$$\rho = \frac{1}{q\mu_n n} \tag{4.3.3}$$

The Hall voltage is given by [22]:

$$V_H = -\frac{BI}{qnW} \tag{4.3.4}$$

The term $-1/qn$ is defined as the Hall coefficient (R_H) and is equal to[1]:

$$R_H = \frac{V_H W}{BI} \tag{4.3.5}$$

Measuring the Hall voltage, induced by given magnetic field and current, one can yield the free-carrier type, concentration and mobility. Usually, the Van der Pauw measurement technique [24, 25] is implemented, which averages the aforementioned parameters over a set of measurements, with and without the application of a magnetic field. The Van der Pauw technique overcomes the rigid geometrical restrictions of the material at hand. Following Fig. 4.8, conductivity measurements are carried out by connecting a voltage source to two successive contacts and by measuring the induced voltage difference between the remaining pair of contacts. Measurements are repeated over all possible contact pairs under both forward and reserve bias voltage. For each measurement, a resistance is

[1] The Hall coefficient is also defined as $R_H = -r/qn$, to account for the dependency of carrier scattering times on their energy. More specifically, r is defined as $r = \langle\tau^2\rangle/\langle\tau\rangle^2$, where τ is the characteristic scattering time.

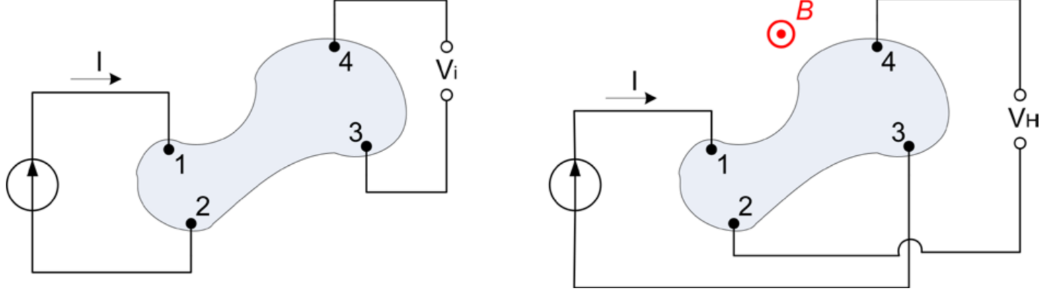

Fig. 4.8: Van der Pauw measurement technique for a sample of arbitrary shape for resistivity (left) and Hall effect (right).

yielded:

$$R_{\mathrm{ij,kl}} = \frac{V_{\mathrm{k}} - V_{\mathrm{l}}}{I_{\mathrm{i}\rightarrow\mathrm{j}}} \tag{4.3.6}$$

The resistivity will then be equal to [24]:

$$\rho = \frac{\pi W}{8\ln 2}\Big[(R_{12,43} + R_{21,34} + R_{23,14} + R_{32,41})f_A + (R_{43,12} + R_{34,21} + R_{14,23} + R_{41,32})f_B\Big] \tag{4.3.7}$$

where f_A and f_B are correction parameters that mitigate sample asymmetries [24].

For Hall effect measurements, a current source is connected between two opposite contacts and the induced voltage difference between the remaining contacts is determined. Measurements are conducted for all possible contact combinations, both with and without an applied magnetic field. The Hall coefficient is then calculated:

$$R_H = \frac{W}{B}\left(\frac{R_{31,42} + R_{42,13}}{2}\right) \tag{4.3.8}$$

where

$$R_{\mathrm{ij,kl}} = \frac{(V_{\mathrm{k}} - V_{\mathrm{l}})_B - (V_{\mathrm{k}} - V_{\mathrm{l}})_0}{I_{\mathrm{i}\rightarrow\mathrm{j}}} \tag{4.3.9}$$

Index B denotes measurements carried out with an applied magnetic field and 0 without one. Electron (index n) and hole (index p) mobility can then be extracted using resistivity and Hall coefficient results:

$$\mu_{n/p} = \frac{|R_H|}{\rho_{n/p}} \tag{4.3.10}$$

The majority carrier type is determined by the Hall coefficient sign and the respective concentration is calculated by:

$$n\ (\text{or } p) = \frac{1}{q|R_H|} \tag{4.3.11}$$

References

[1] W. Braun, *Applied RHEED: Reflection High-Energy Electron Diffraction During Crystal Growth.* Springer-Verlag Berlin Heidelberg, (1999).

[2] T. A. Carlson, *Photoelectron and Auger Spectroscopy.* New York: Plenum, (1975).

[3] A. Benninghoven, J. Okano, R. Shimizu, and H. W. Werner in *Secondary Ion Mass Spectrometry SIMS IV*, Springer Series in Chemical Physics, (Osaka, Japan), Springer Berlin, Heidelberg, (1983).

[4] K. Ploog and A. Fischer *Appl. Phys.*, vol. **13**, pp. 111–121, (1977).

[5] L. E. Murr, *Electron and Ion Microscopy and Microanalysis: Principles and Applications.* Boca Raton: CRC Press, 2nd ed., (1991).

[6] R. D. Heidenreich, *Fundamentals of Transmission Electron Microscopy.* New York: Wiley-Interscience, (1964).

[7] R. Reifenberger, *Fundamentals of Atomic Force Microscopy Part I: Foundations.* World-Scientific, (2015).

[8] B. D. Cullity, *Elements of X-Ray Diffraction.* Reasing, MA: Addison-Wesley, (1967).

[9] M. D. Lumb, *Luminescence Spectroscopy.* New York: Academic, (1978).

[10] E. H. Putley, *The Hall Effect and Related Phenomena.* London: Butterworth, (1960).

[11] M. Sze, *Physics of Semiconductor Devices.* New York: Wiley-Interscience, (1969).

[12] M. A. Herman and H. Sitter, *Molecular Beam Epitaxy: Fundamentals and Current Status.* Springer-Verlag, 2nd ed., (1996).

[13] R. A. Kubiak, S. M. Newstead, and P. Sullivan, “1 - the technology and design of molecular beam epitaxy systems,” in *Molecular Beam Epitaxy* (R. F. Farrow, ed.), pp. 1–113, Park Ridge, NJ: William Andrew Publishing, (1995).

[14] J. R. Christman, *Fundamentals of Solid State Physics.* New York: Wiley, (1988).

[15] P. P. Ewald *Ann. Der Physik*, vol. **54**, p. 519, (1917).

[16] P. Pukite, C. Lent, and P. Cohen *Surf. Sc.*, vol. **161**, no. 1, pp. 39–68, (1985).

[17] G.-C. Wang and T.-M. Lu, *RHEED Transmission Mode and Pole Figures: Thin Film and Nanostructure Texture Analysis.* New York: Springer, (2014).

[18] O. Milton, *The Materials Science of Thin Films.* Academic Press, (1992).

[19] G. Binnig, C. F. Quate, and C. Gerber *Phys. Rev. Lett.*, vol. **56**, pp. 930–933, (1986).

[20] V. Sudarsan, “Chapter 4 - materials for hostile chemical environments,” in *Materials Under Extreme Conditions* (A. Tyagi and S. Banerjee, eds.), pp. 129–158, Amsterdam: Elsevier, (2017).

[21] R. Asmatulu and W. S. Khan, *Synthesis and Applications of Electrospun Nanofibers.* Elsevier, (2019).

[22] E. H. Hall *Amer. J. Math.*, vol. **2**, no. 3, pp. 287–292, (1879).

[23] R. S. Muller and T. I. Kamins, *Device Electronics for Integrated Circuits.* Wiley, 3rd ed., (2002).

[24] L. J. Van der Pauw *Phillips Research Reports*, vol. **13**, pp. 1–9, (1958).

[25] L. J. Van der Pauw *Phillips Research Reports*, vol. **20**, pp. 220–224, (1958).

5. Schrödinger-Poisson Solver

The quest for understanding and harnessing quantum phenomena has led to the development of powerful theoretical frameworks. One such framework is the self-consistent solution of the Schrödinger-Poisson equations, a fundamental approach used to unravel the intricate interplay between quantum mechanics and electrostatics. Semiconductor nano-structures, characterized by their remarkably small dimensions and unique electronic properties, offer a fertile ground for investigating quantum effects at the nanoscale. By self-consistently solving the Schrödinger-Poisson (SCSP) equations, one may delve into the behavior of electrons and holes in these confined systems, accounting for the influence of their own charge distribution on the overall electrostatic potential. This iterative computational technique lies at the heart of unraveling the underlying physics and designing novel devices with tailored functionalities.

In this chapter, the principles of self-consistently solving the Schrödinger and Poisson equations are discussed, introducing the SCSP software implemented for this work. Assumptions and approximations made in SCSP calculations are also listed.

5.1 The Equations

The one-dimensional Schrödinger equation is:

$$-\frac{\hbar^2}{2}\frac{d}{dx}\left(\frac{1}{m^*(x)}\frac{d\psi(x)}{dx}\right)+V(x)\psi(x)=E\psi(x) \tag{5.1.1}$$

where $\hbar$ is the reduced Plank's constant, m^* is the carrier effective mass, E is the energy eigenvalue with ψ being the corresponding wavefunction, and V is the potential energy.

The one-dimensional Poisson equation is:

$$\frac{d}{dx}\left(\varepsilon_s(x)\frac{d\phi(x)}{dx}\right)=-\rho(x) \tag{5.1.2}$$

where ε_s is the position dependent dielectric tensor, ϕ denotes the electrostatic potential and ρ is the charge density. Generally, the charge density is composed of holes p, electrons n, ionized donors N_D^+ and acceptors N_A^-, as well as fixed charges ρ_{fix}:

$$\rho(x)=q\left[p(x)-n(x)+N_D^+(x)-N_A^-(x)+\rho_{\text{fix}}(x)\right] \tag{5.1.3}$$

Contributions to the fixed charges ρ_{fix} are polarization charges ρ_{pol} due to piezo- and

pyroelectric polarization as well as fixed surface and volume charges $\rho_{\text{surf/vol}}$:

$$\rho_{\text{fix}}(x) = \rho_{\text{pol}}(x) + \rho_{\text{surf/vol}}(x) \tag{5.1.4}$$

The determination of the polarization charges is discussed in Section 2.1.

The term "self-consistent" implies that both the electronic wavefunctions and the electrostatic potential are determined in a mutually dependent manner. Therefore, the main obstacle is that the Schrödinger equation is dependent on the electrostatic potential, while the Poisson equation is dependent on the wavefunctions ψ_n:

$$H(\phi(x))\psi_n(x) = E_n\psi_n(x) \tag{5.1.5}$$

and

$$\frac{d}{dx}\left(\varepsilon_s(x)\frac{d\phi(x)}{dx}\right) = -\rho(\psi_1, \psi_2, \dots) \tag{5.1.6}$$

Solving the coupled Schrödinger and Poisson equations requires the determination of a self-consistent solution for the charge densities or equivalently for the electrostatic potential. In other words, the charge distribution generated by the wavefunctions matches the electrostatic potential, and the electrostatic potential properly accounts for the charge distribution.

5.2 The Nextnano Software

Nextnano [1] is a modeling software for nanoscale devices, which facilitates the design and understanding of semiconductor structures and devices. The first step to solving the coupled differential equations, is their discretization and mapping onto a grid [2]. This is achieved by implementing the box integration finite differences scheme. This discretization scheme is flux conserving in the presence of material discontinuities as they naturally occur in the simulation of heterostructures. The discretization of those partial differential equations results either in linear systems of equations or large matrix eigenvalue problems that can be solved by iterative algorithms.

The iterative solution process implemented is the predictor-corrector approach developed by Trellakis et al. [3]. The exact carrier densities p(x) and n(x) from Eq. (5.1.3) are replaced by predictors depending on the electrostatic potential [2]:

$$\tilde{p}[\phi](x) = \sum_{i \in VB} g_v^i \sum_j p_{v,j}^i(x) f([E_{v,j}^i - q(\phi(x) - \phi_{\text{prev}}) - E_F(x)]/kT) \tag{5.2.1}$$

$$\tilde{n}[\phi](x) = \sum_{i \in CB} g_c^i \sum_j p_{c,j}^i(x) f([-E_{c,j}^i - q(\phi(x) - \phi_{\text{prev}}) + E_F(x)]/kT) \tag{5.2.2}$$

where ϕ_{prev} denotes the electrostatic potential from the previous iteration step, g_l^i account for spin and valley degeneracies, and $p_{l,j}^i$ is the occupation probability density of each state j, for electrons ($l = c$) and holes ($l = v$). The i index runs over all included valence (or conduction) bands. $f(E)$ is the Fermi-Dirac distribution, E_v (E_c) is the valence (conduction) band energy and E_F denotes the Fermi level. Eqs. 5.2.1 and 5.2.2 are correct only in equilibrium. The iterative algorithm can be summarized as follows [3]:
For k=1,2,... and given (initial prediction) ϕ_1

1. Solve $H(\phi_k)\psi_n^{(k)} = E_n^{(k)}\psi_n^{(k)}$ for a set of N_{ev} of eigenfunctions $\psi_1^{(k)}, \psi_2^{(k)}, \ldots, \psi_{N_{\text{ev}}}^{(k)}$ and corresponding eigenenergies $E_1^{(k)}, E_2^{(k)}, \ldots, E_{N_{\text{ev}}}^{(k)}$,
2. Solve the non-linear Poisson equation $\frac{d}{dx}\left(\varepsilon_s(x)\frac{d\phi_{k+1}(x)}{dx}\right) = -\rho(\phi_k, \{\psi_n^{(k)}\})$.

This process is terminated when the calculated potential and eigenfunctions converge, i.e. the predictors assume the correct values. The unique solution of the Poisson equation requires specifying boundary conditions. Boundary conditions are set at the boundaries of the nanostructure.

Simply put, in the self-consistent solution approach, the electrostatic potential is initially assumed, and based on that, the wavefunctions and the charge density are calculated using the Schrödinger equation. The obtained charge density then influences the potential, which is subsequently adjusted by Poisson's equation. This iterative process continues until a self-consistent solution is reached, wherein the electronic wavefunctions and the electrostatic potential are in agreement with each other.

5.3 Material Parameters and Simulation Conditions

Material parameters used in SCSP calculations are listed in Table 5.1. Alloy parameters are calculated as explained in Section 2.2.4. Specifically, for $In_xAl_{1\text{-}x}N$, the bandgap energy and spontaneous polarization are considered equal to [4, 5, 6]:

$$E^g_{\text{InAlN}}(x) = 0.63x + 6.25(1-x) - 3.10x(1-x) \tag{5.3.1}$$

and

$$P^{sp}_{InAlN}(x) = -0.042x - 0.090(1-x) + 0.070x(1-x) \tag{5.3.2}$$

It must be mentioned that Eq. 5.3.1 might be inaccurate, as the related bowing parameter is considered independent of the molar fraction x. In In-containing ternary alloys, the bowing parameter has been found to depend on In-composition [7].

Conduction band discontinuities and polarization-related parameters incorporated in the calculations were set according to the literature [8, 9, 10]. Band discontinuities

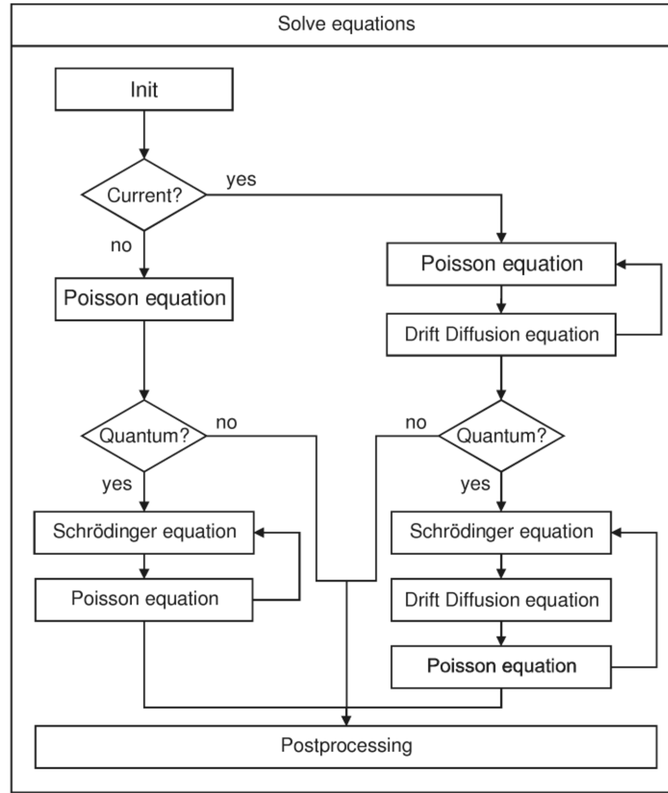

Fig. 5.1: Flow chart of SCSP equation solving algorithm. Reprinted from [2].

are taken into account by considering a common reference level of energy (0 eV) for the values of the conduction band minima and valence band maxima [1, 2]. In essence, band discontinuities were calculated by aligning the charge neutrality levels of the different materials.

Spontaneous polarization values of -0.042C/m^2, -0.034C/m^2 and -0.090C/m^2 were used for InN, GaN and AlN respectively [6]. Pseudomorphic growth is approximated by including a sheet charge induced by a piezoelectric polarization discontinuity. The piezoelectric polarization is calculated using Eq. 2.2.7, repeated here for reader's convenience:

$$P_{pz,3} = 2\frac{a - a_0}{a_0}\left(e_{31} - e_{33}\frac{C_{13}}{C_{33}}\right) \tag{5.3.3}$$

For the boundary conditions, the Ni/Insulator barrier height was calculated according to the ideal theory of a Schottky junction, $q\Phi_B = q\Phi_m - X$, where $q\Phi_m \approx 5.1$ eV is the work function of Ni and X is the electron affinity of each insulator. The deviations from the charge neutrality levels as set by Refs. [8, 9, 10] are negligible. Charge neutrality (flat bands) was considered as the boundary condition at the bottom surface of the buffer layer.

Table 5.1: Material parameters used in SCSP equation solver. Data retrieved from Refs. [4-9].

	E_{gap} (eV)	VBO (eV)	$\epsilon_{\|\|}$	$\epsilon_{\perp}$	P_{sp} (C/m^2)	N_D (cm^{-3})
InN	0.63	-0.38	14.4	13.1	-0.042	10^{18}
GaN	3.40	-0.73	10.1	9.28	-0.034	10^{16}
AlN	6.25	-1.53	8.57	8.67	-0.090	10^{14}
Si_3N_4	5.3	-1.94	7.0			
HfO_2	5.8	-2.63	25.0			
SiO_2	9.0	-4.57	3.9			
Al_2O_3	8.8	-4.52	11.5			

Finally, all simulations are realized considering equilibrium conditions (E_F=0) and room temperature (T= 300K). The donor concentrations were set to $N_D^{InN} = 10^{18}$ cm^{-3}, $N_D^{GaN} = 10^{16}$ cm^{-3}, and $N_D^{AlN} = 10^{14}$ cm^{-3}.

Table 5.2 lists the bandgap energies, valence band offsets (VBO), dielectric constants, spontaneous polarization constants and donor concentrations that were used by the one-dimensional SCSP solver to model the aforementioned MIS systems.

References

[1] S. Birner, T. Zibold, T. Andlauer, T. Kubis, M. Sabathil, A. Trellakis, and P. Vogl *IEEE Transactions on Electron Devices*, vol. **54**, no. 9, pp. 2137–2142, (2007).

[2] T. Zibold. PhD thesis, (2007).

[3] A. Trellakis, A. T. Galick, A. Pacelli, and U. Ravaioli *J. Appl. Phys.*, vol. **81**, no. 12, pp. 7880–7884, (1997).

[4] O. Ambacher and V. Cimalla in *Polarization Effects in Semiconductors – From Ab Initio Theory to Device Applications* (C. Wood and D. Jena, eds.), ch. Polarization Induced Effects in GaN-based Heterostructures and Novel Sensors, p. 56, Springer Publications, (2008).

[5] E. Iliopoulos, A. Adikimenakis, C. Giesen, M. Heuken, and A. Georgakilas *Appl. Phys. Lett.*, vol. **92**, no. 19, p. 191907, (2008).

[6] I. Vurgaftman and J. R. Meyer *J. Appl. Phys.*, vol. **94**, no. 6, pp. 3675–3696, (2003).

[7] M. Androulidaki, N. T. Pelekanos, K. Tsagaraki, E. Dimakis, E. Iliopoulos, A. Adikimenakis, E. Bellet-Amalric, D. Jalabert, and A. Georgakilas *phys. stat. solidi c*, vol. **3**, no. 6, pp. 1866–1869, (2006).

[8] J. Robertson and B. Falabretti *J. Appl. Phys.*, vol. **100**, no. 1, (2006). 014111.

[9] S.-H. Wei and A. Zunger *Appl. Phys. Lett.*, vol. **72**, no. 16, pp. 2011–2013, (1998).

[10] C. Van de Walle and J. Neugebauer *nature*, vol. **423**, p. 626–628, (2003).

6. Results & Discussion

The utilization of InN in modern devices must deal with multiple impediments. InN materials exhibit high bulk electron concentration in the range of 10^{17}-10^{18} cm^{-3}. The reason behind the unintentional n-type conductivity of InN is unclear [1]. The traditional candidates are donor impurities, such as oxygen or hydrogen, and donor-type native defects, such as nitrogen vacancies [1]. Threading dislocations have also been suggested as a source of unintentional n-type doping in InN [2, 3].

Beyond a high bulk carrier concentration, InN surfaces exhibit electron accumulation layers [4, 5], which pin the Fermi level within the conduction band, increasing the near-surface electron concentration compared to the bulk value. The conduction band minimum of InN is below the charge neutrality level and, consequently, positively charged donor-like surface states occur [6]. A subsequent downward band-bending induces an electron accumulation at the surface.

An additional problem is the large lattice mismatch between InN and either AlN or GaN buffer layers ($> 10\%$). InN has a larger in-plane lattice constant than GaN and AlN, and thus pseudomorphic InN heterostructures will exhibit an in-plane compressive strain and a tensile strain in the [0001]-direction. The presence of misfit dislocations quickly (after the first monolayer [7]) turns favorable over the coherent growth of InN on the substrate and a high density of threading dislocations occurs in the grown InN film. The relaxed InN layers have their own lattice constant and piezoelectric polarization effects, which may influence device engineering, are weakened or totally vanish.

Scattering on threading dislocations degrades the transport properties of these InN layers, rendering them problematic for use as transistor channel. However, the study of these heterostructures is meaningful to understand how the concentration and distribution of carriers could be controlled. In this work, InN nano-heterostructures are examined. Thin InN films have been grown on either GaN or AlN templates, using a RIBER 32 PA-MBE system, equipped with an Oxford HD25 nitrogen RF plasma source. Self-Consistent Schrödinger-Poisson (SCSP) equation solving software has been implemented for the energy band and charge distribution profiling of such structures for the prediction of their behaviour.

6.1 Substrate Preparation

Before the deposition of InN on the substrates, the latter must undergo certain preparation stages that ensure surface cleanliness and homogeneity, but also limit the contamination of

the growth chamber by unwanted species. In other words, adsorbed atomic or molecular elements are removed from the surface and a smooth, pure GaN or AlN substrate endlayer is formed for the subsequent epitaxial growth of InN.

The preparation procedure is similar for both GaN and AlN templates and consists of ex situ (before the sample's introduction into the MBE system) and in situ (inside the vacuum chambers) treatments. The first step entails the cleaning of the substrate surface by immersion into a set of solutions. For the removal of organic molecules and greases, the sample is subjected to acetone, which is subsequently removed by propanol. Finally, the substrate is washed down by distilled water and dried by nitrogen gas. The substrate is then glued on the sample holder using indium as adhesive material and introduced into the MBE load chamber. Inside the latter, the sample is submitted to a degassing process.

The sample is then moved into the growth chamber, where it undergoes the final preparation stage. Under ultra-high vacuum conditions (10^{-11} Torr), the holder is heated again for the decomposition of any surface oxide layer and the desorption of any residual alien atoms or molecules from the substrate. Immediately after, a thin layer of the same material is grown on the substrate under metal-rich conditions. This way, its endlayer is rendered as smooth, uniform and pure as possible before we initiate the deposition of InN on it. Extra attention must be paid at the growth of AlN. Under Al-rich growth conditions, the formation of AlN droplets is likely. The desorption of those, however, is very difficult due the extremely high temperatures needed for the task. Finally, after the substrate preliminary growth is complete, the sample is maintained at an elevated temperature for a few minutes, in order to rid the substrate of the gallium or aluminum adlayers, by desorption. Growth progress was monitored by in-situ RHEED, operated at 15 kV. Streaky patterns would indicate a smooth substrate surface, without 3D islands and roughness. Temperature is then lowered to initiate the epitaxial growth of InN.

6.2 Thin InN Film Growth

After the aforementioned ex-situ substrate degreasing and in-situ heating, the temperature was reduced to approximately 450°. 5 nm thin InN layers have been grown directly on the GaN and AlN substrate, under In-rich conditions (flux ratio III/V=2), which favor layer-by-layer InN growth and uniform coverage of the substrate.

As previously explained, an indium adlayer is constantly present under such growth conditions. The thickness of said adlayer is increased over time, which could eventually lead to the formation of InN droplets, destroying the InN film's continuity and homogeneity. In GaN growth under metal-rich conditions (flux ratio III/V>1), the substrate temperature is sufficient to desorb excess Ga while GaN decomposition is negligible. On the contrary, InN crystal decomposes in vacuum at a temperature $\sim$ 100°C lower than the temperature

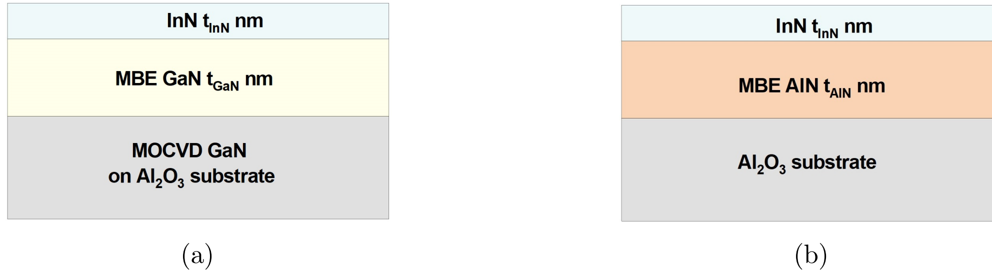

(a) (b)

Fig. 6.1: Schematic cross section of the (a) InN/GaN and (b) InN/AlN (0001) structures grown by RF-MBE.

needed for InN to desorb from the surface [7]. Thus, the removal of excess In atoms from the epilayer surface is infeasible without the destruction of the deposited InN layers. To overcome this obstacle and avoid the formation of In droplets, surface nitridation is periodically implemented. This way, nitrogen plasma elements interact with indium adatoms, converting the purely metallic overlayer into InN. Again, growth progress was monitored by in-situ RHEED, operated at 15 kV. RHEED observations during growth revealed a streaky pattern for the surface of the overgrown InN(0001) layer, suggesting an atomic smooth surface.

6.3 Conductivity and Hall-Effect Measurements

Conductivity and Hall-effect measurements for 5 nm of InN grown on GaN template (sample S1) resulted in a sheet resistance (R_{sh}) of 1.5×10^3 Ω/sq, a sheet electron density (N_s) of 8.2×10^{13} cm^{-2} and a Hall mobility (μ) of 51 cm^2/V s. Test device fabrication is under way for the remaining samples. The very low mobility measured is attributed to the very high average electron concentration ($\sim 10^{20}$ cm^{-3}) and to the high density of defects in the relaxed InN layer. The InN layers on AlN buffer could not be measured, due to unclear reasons that are under investigation.

6.4 Atomic Force Microscopy

Atomic force microscopy revealed that continuous, ultra-thin (of very few nm) InN films can be grown on GaN, with atomic-smooth surfaces and uniform thickness, which is characteristic of two-dimensional, step-flow growth by MBE. Fig. 6.2 is an indicative AFM micrograph of a 2×2 μm^2 scanned area of 5 nm InN/GaN-buffer. The root mean square (rms) roughness of the surface is 0.3 nm.

Table 6.1: Description of experiments of PA-MBE growth of InN nano-heterostructures.

Sample ID	Substrate	Preliminary Growth	t_{InN}	T_{Growth}(InN)
S1.	GaN/Al_2O_3 (MOCVD)	350 nm GaN (∼ 670°C)	5 nm	440°C
S2.	GaN/Al_2O_3 (MOCVD)	350 nm GaN (∼ 670°C)	5 nm	430°C
S3.	GaN/Al_2O_3 (MOCVD)	300 nm GaN (∼ 670°C)	2 nm	430°C
S4.	GaN/Al_2O_3 (MOCVD)	300 nm GaN (∼ 670°C)	3 nm	430°C
S5.	GaN/Al_2O_3 (MOCVD)	400 nm GaN (∼ 670°C)	5 nm	430°C
S6.	Al_2O_3	400 nm AlN (∼ 750°C)	5 nm	430°C
S7.	AlN/Al_2O_3 (MOCVD)	100 nm AlN (∼ 750°C)	5 nm	430°C

6.5 Energy Band and Charge Distribution Profiling

One dimensional self-consistent Schrodinger-Poisson (SCSP) calculations have been carried out to simulate planar InN heterostructures, as well as MIS systems with different insulator materials. This work aims to understand how the concentration and distribution of carriers in a thin InN layer is affected by heterostructure design, i.e. type of buffer layer, polarization, unintentional doping, surface Fermi level pinning for bare InN surfaces or type of dielectric for MIS structures.

The *nextnano software for semiconductor nanodevices* [8] was utilized for the 1D modeling of InN-based structures. Thin InN films (2, 5, 10, 15 nm) were considered on GaN and AlN buffer layers. For MIS structures, the presence of 10 nm of amorphous insulating materials on top of the InN epilayer was evaluated. Namely, silicon nitride (Si_3N_4), hafnium dioxide (HfO_2), silicon oxide (SiO_2) and aluminum oxide (Al_2O_3) were examined. Nickel (Ni) gate contacts were considered on top of the insulator

Simulations of MIS structures have been carried out by several groups. Ganguly et al. [9] and Zervos et al. [10] have studied Ni / Al_2O_3 / AlN / GaN (0001) and Ni /

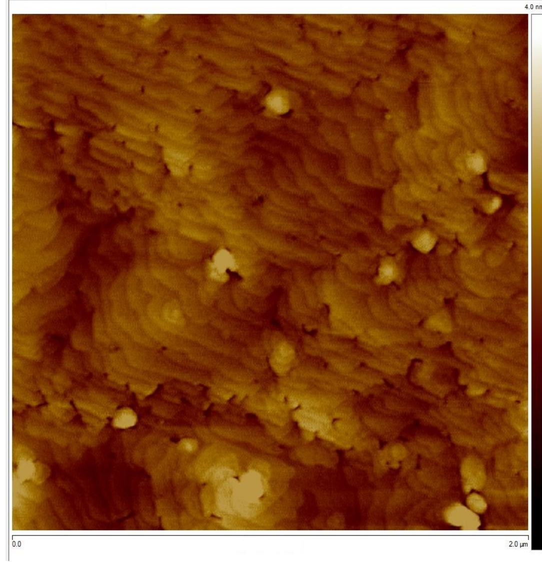

Fig. 6.2: AFM micrographs showing the surface of InN epitaxially grown on GaN (0001). The rms roughness was 0.3 nm. Surface atomic steps can be observed.

Si_3N_4 / InN / GaN (0001) MIS systems, respectively, and by the C-V profiling of the structures, observed a decreasing trend of the threshold voltage with dielectric thickness (V_T got more negative). This phenomenon and the corresponding equilibrium carrier density in the formed channel could stem from the presence of a fixed positive charge at the insulator/semiconductor interface (Q_{if}) that would compensate negative polarization charges at the III-nitride surfaces (GaN or InN). Both groups estimated the required amount of Q_{if} by utilizing a SCSP equation solver. Specifically, Ganguly et al., in order to reproduce experimental results, calculated $Q_{if} \sim 6 \times 10^{13}\text{cm}^{-2}$, which is almost equal to the polarization-induced surface charge of the strained AlN layer, further supporting their initial suggestion. However, Zervos et al. calculated a Q_{if} value of $4.4 \times 10^{13}\text{cm}^{-2}$, which is almost double the surface polarization charges of the relaxed InN layer.

Here, we repeat the calculations realised by Zervos et al., for the Si_3N_4/InN/GaN heterostructure, using updated values for the spontaneous polarization of each III-nitride material as well as for the bandgap energy of InN, as shown in Table 5.1. We conclude that a near-identical value Q_{if} (presented below) is necessary for SCSP calculations to match the experimental data of Zervos et al.

In the following simulations, two cases are examined, wherein the interface charge is initially ignored and then assumed to be an intrinsic phenomenon of junctions between amorphous (non-polar) dielectrics and polar semiconductors. That is, we assume that the calculated value of Q_{if} is not specific to Si_3N_4/InN/GaN but could rather be present in all insulator/InN interfaces. With this in mind, we shall examine Ni/insulator/InN/GaN-or-AlN MIS structures that utilize Si_3N_4, SiO_2, Al_2O_3, or HfO_2 as dielectric material.

Additionally, in order to overcome the great lattice mismatch between InN and either GaN or AlN, an $In_xAl_{1-x}N$ intermediate layer has been suggested between InN and the buffer layer. InN/$In_{0.8}Al_{0.2}N$ and graded InN/$In_xAl_{1-x}N$ structures are computationally modeled on GaN and AlN substrates.

6.5.1 The InN/GaN Heterostructure

InN/GaN(0001)-based structures were first examined by SCSP calculations. Conduction band discontinuity at the hetero-interface is equal to $\Delta E_C^{InN/GaN} = 2.4$ eV. For bare InN(0001) surfaces, the Fermi level was initially positioned 0.9 eV above the conduction band minimum at the surface of InN [6, 1]. InN was assumed to be fully relaxed on the GaN buffer layer, i.e. only spontaneous polarization effects were considered.

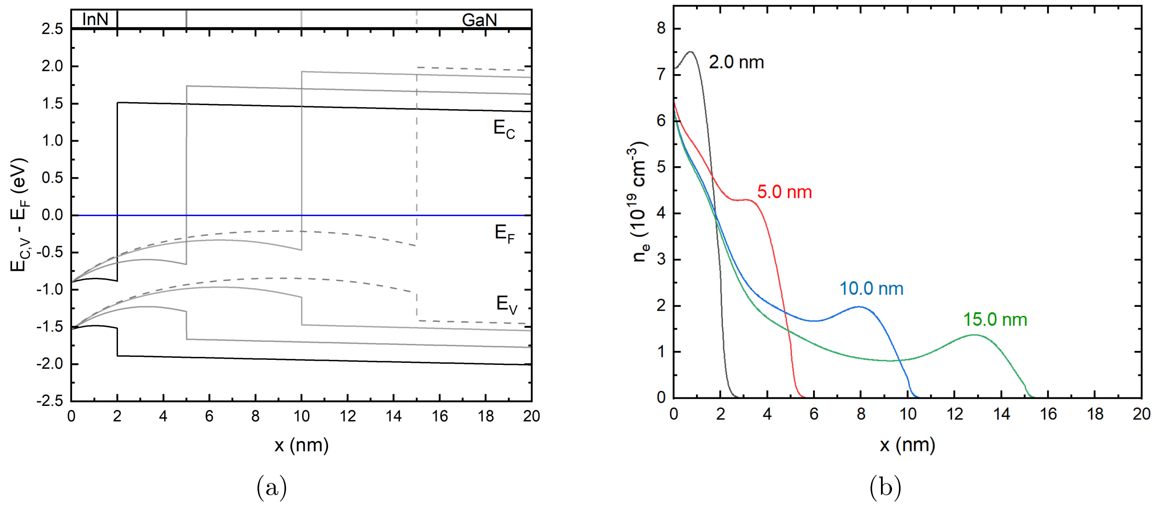

Fig. 6.3: (a) Simulated band diagrams and (b) electron concentration profiles for the InN (2, 5, 10, 15 nm)/GaN structures.

Fig. 6.3 depicts the energy band and carrier distribution profiling of the structures for 2, 5, 10 and 15 nm InN layer thicknesses. A double-peak electron distribution is exhibited. As expected, the first peak is observed at the InN surface, due to the Fermi level pinning above the conduction band. The second peak is exhibited at the InN/GaN interface, where the InN conduction band drops with respect to the Fermi level. The spontaneous polarization discontinuity induces a positive sheet charge at the InN/GaN interface, which in turn leads to an electron accumulation. The InN/GaN interface also induces a large barrier for electron motion toward the substrate, as electron distribution quickly vanishes within GaN (∼1 nm). The calculated 2DEG densities range from 1.3 to 2.6×10^{13} cm^{-2} (increasing with InN layer thickness). This differs from the value obtained by Hall-effect measurements ($N_s \sim 8 \times 10^{13}$ cm^{-2}), for the case of 5 nm. This disagreement might stem from the high series resistances and inhomogeneities in the ultra thin InN heterostructure,

due to strain relaxation in the latter. It can also be attributed to a low donor density considered for InN. The effects of higher donor densities are examined in Section 6.5.6.

Si_3N_4/InN/GaN

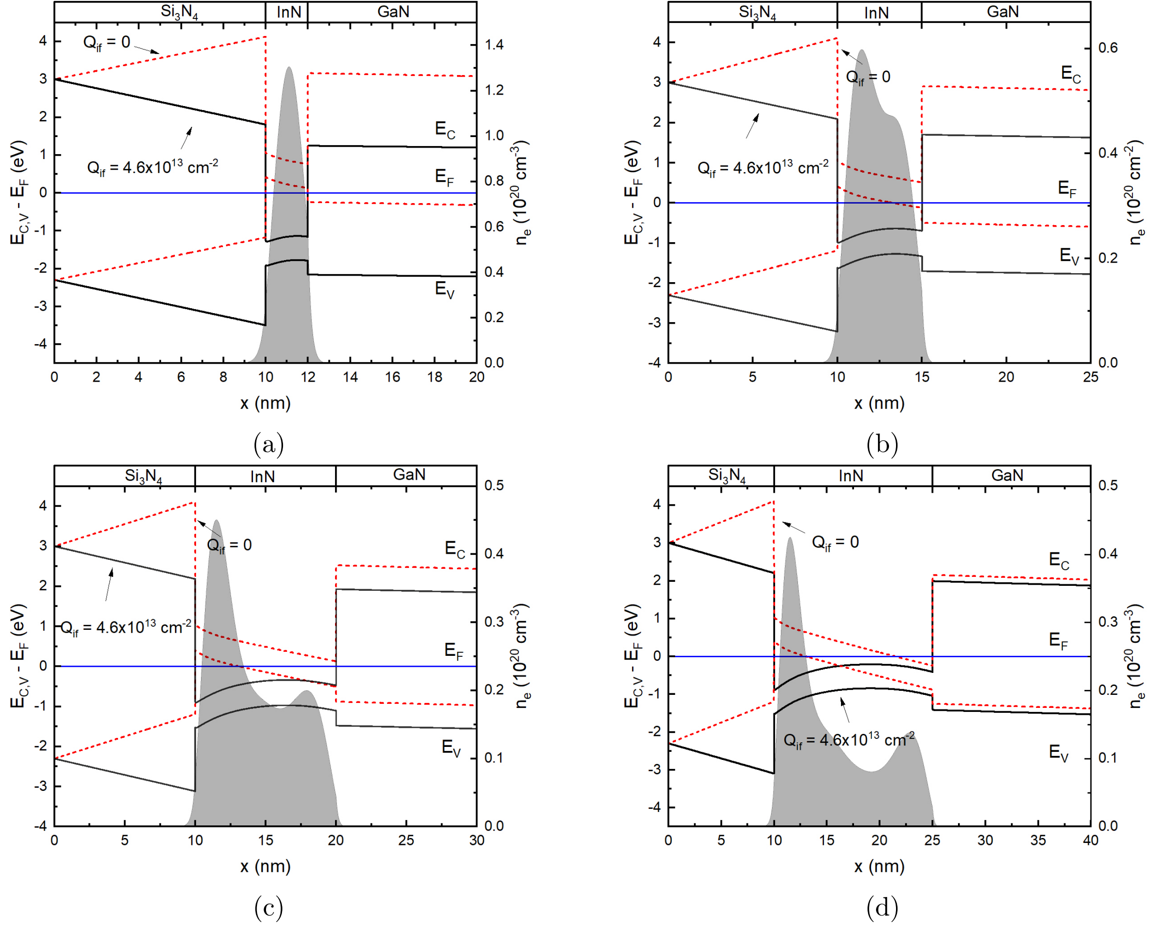

Fig. 6.4: Energy band diagrams and electron concentration (including Q_{if}) for the Ni/Si_3N_4/InN/GaN MIS structure, for (a) 2nm, (b) 5nm, (c) 10nm and (d) 15 nm InN layer thicknesses.

First, the effects of silicon nitride (Si_3N_4) are evaluated. The Ni/Si_3N_4 surface barrier height used is equal to $q\Phi_B = 3.0$ eV. The conduction band discontinuity at the Si_3N_4/InN interface is equal to ΔE_C=3.1 eV [11]. Fig. 6.4 shows the simulated band diagrams for the MIS systems across various InN thicknesses, both with and without the positive sheet charge $Q_{if} = 4.6 \times 10^{13}$ cm^{-2} at the Si_3N_4/InN interface.

If no interface charge is considered, the InN layer is fully depleted of electrons for every InN layer thickness except 15nm. The Fermi level for the cases of 2, 5 and 10 nm, is positioned below the conduction band of InN. In the case of 15 nm, a very shallow quantum well (QW) is formed at the InN/GaN interface. An extremely low 2DEG density of 2.6×10^{11} cm^{-2} is calculated at said hetero-interface. No matter the InN layer thickness, the valence band of InN crosses the Fermi level at the Si_3N_4/InN interface, which causes

the formation of a 2DHG. Its density is calculated to be $\sim 1.5 \times 10^{13}$ cm^{-2}. Assuming the additional positive charge Q_{if} at the Si_3N_4/InN interface, the InN conduction band minima drop beneath the Fermi level. The positive sheet charge induces a 2DEG in the InN layer that increases with InN thickness. ranging $2.1 - 2.4 \times 10^{13}$ cm^{-2}.

HfO_2/InN/GaN

Hafnium dioxide (HfO_2) is next examined. The Ni/HfO_2 surface barrier is set to $q\Phi_B = 2.7$ eV [11]. The conduction band discontinuity at the HfO_2/InN interface is considered equal to ΔE_C=2.9 eV.

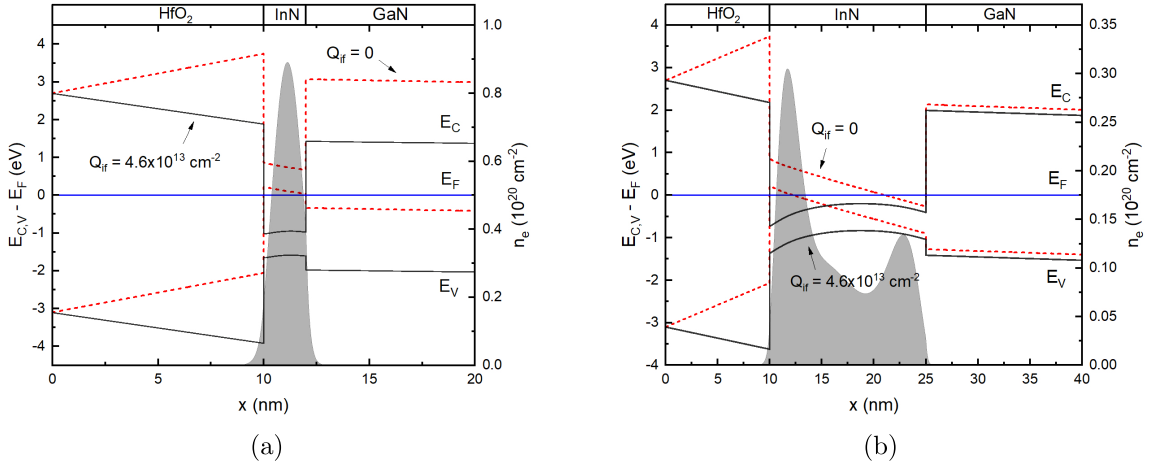

Fig. 6.5: Energy band diagrams and electron concentration (including Q_{if}) for the the Ni/HfO_2/InN/GaN MIS structure, for (a) 2nm and (b) 15 nm InN layer thicknesses.

Similarly, ignoring the positive sheet charge Q_{if}, the Fermi level is within the InN bandgap, for layer thicknesses of 2, 5 and 10 nm. For 15 nm, a shallow 2DEG confining QW is formed at the InN/GaN interface. The induced 2DEG density is approximately equal to 6×10^{11} cm^{-2}. The presence of a 2DHG is also predicted for every InN layer length, with a density $\sim 5 \times 10^{12}$ cm^{-2}. Considering Q_{if}, the Fermi level is pinned within the conduction band of InN. The predicted 2DEG densities are $1.4 - 2.0 \times 10^{13}$ cm^{-2}, increasing with InN thickness.

Al_2O_3/InN/GaN

For amorphous Al_2O_3, the Ni/Al_2O_3 Schottky barrier height is set to $q\Phi_B = 4.1$ eV. Al_2O_3/InN conduction band discontinuity is equal to $\Delta E_C = 4.0$ eV.

The predicted behaviour is near identical with the previous cases. If no sheet charge is considered at the Al_2O_3/InN interface, a 2DHG is predicted to form near the insulator, the density of which is approximately 1.4×10^{13} cm^{-2}, across all InN layer lengths. For 15 nm of InN, the Fermi level crosses the conduction band of InN near the InN/GaN interface,

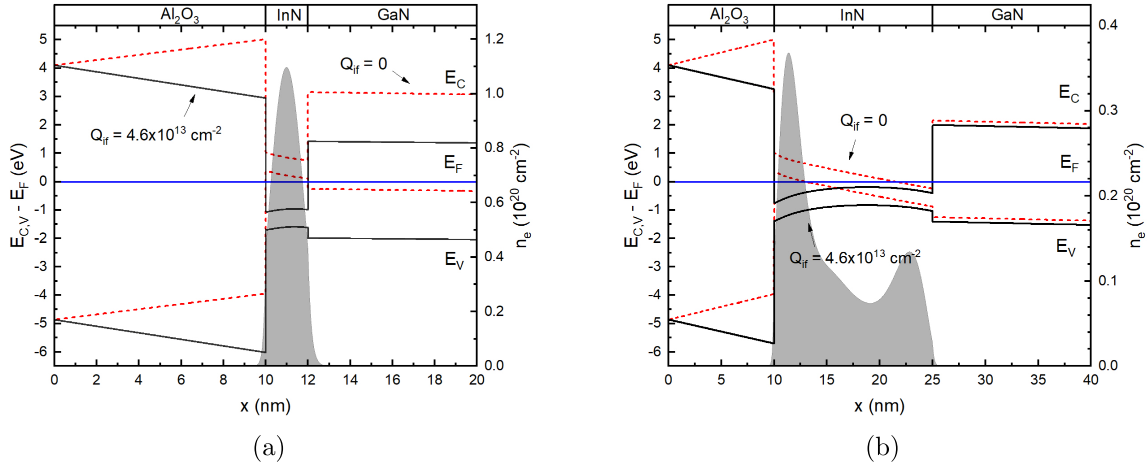

Fig. 6.6: Energy band diagrams and electron concentration (including Q_{if}) for the the $Ni/Al_2O_3/InN/GaN$ MIS structure, for (a) 2nm and (b) 15 nm InN layer thicknesses.

and a low concentration 2DEG is formed of approximately 3×10^{11} cm^{-2}. When Q_{if} is taken into consideration, the Fermi level is pinned above the conduction band minima of InN. The subsequent 2DEG densities range $1.8 - 2.1 \times 10^{13}$ cm^{-2}, increasing with InN thickness.

SiO_2/InN/GaN

Finally, the effects of silicon dioxide (SiO_2) on the InN/GaN heterostructure are examined. The potential barrier at the Ni/SiO_2 Schottky contact is set to $q\Phi_B = 4.2$ eV. The conduction band discontinuity at the SiO_2/InN interface is equal to $\Delta E_C = 4.3$ eV. The simulated band profiles are shown in Fig. 6.7.

Ignoring Q_{if}, the presence of a 2DHG of density $\sim 1.7 \times 10^{13}$ cm^{-2} is again predicted near the SiO_2/InN interface. For the 15nm InN thickness case, the 2DEG confined at the shallow QW formed at the InN/GaN interface has a concentration of approximately 2×10^{11} cm^{-2}. Now, assuming the presence of the positive sheet charge Q_{if} at the SiO_2/InN interface, the calculated densities of the predicted 2DEG are $2.2 - 2.5 \times 10^{13}$ cm^{-2}.

Conclusions

No matter the interface charge between the insulating material and indium nitride and regardless of the insulating material used, a QW is formed near the InN/GaN interface for 15 nm of InN, due to the spontaneous polarization discontinuity between the two materials. In other words, there could be a critical thickness of InN, under which the Fermi level is positioned within the InN bandgap, preventing the accumulation of electrons. It should be noted, however, that defect-induced charges [3] have been ignored at the InN/GaN interface. A more detailed study of potential donor-like states of dislocations is presented

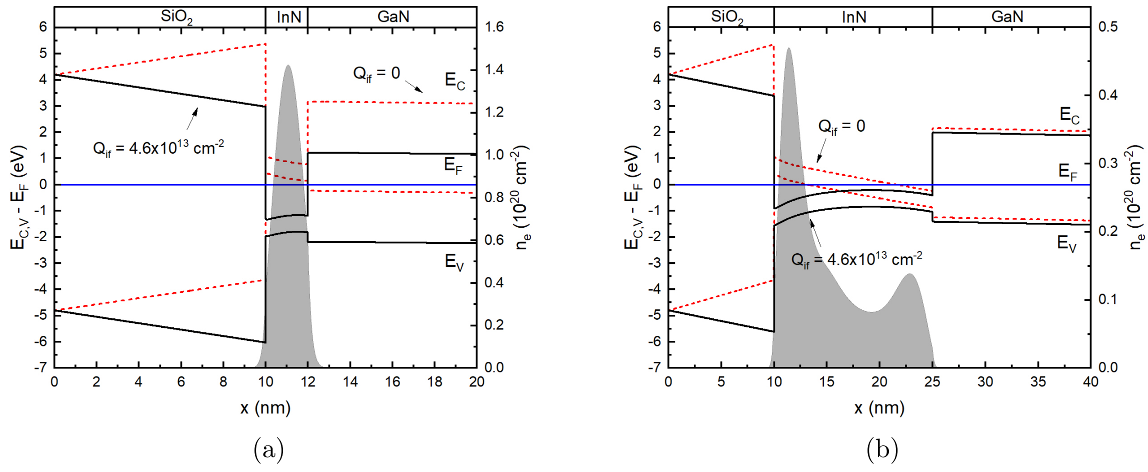

(a) (b)

Fig. 6.7: Energy band diagrams and electron concentration (including Q_{if}) for the the Ni/SiO_2/InN/GaN MIS structure, for (a) 2nm and (b) 15 nm InN layer thicknesses.

in Section 6.5.5.

What is more, hafnium dioxide seems to better control the polarization induced 2DHG/2DEG at the InN layer (see Fig. 6.8). 2DHG densities are approximately equal to $\sim 0.6 \times 10^{13}$ cm^{-2}, while 2DEG densities, when Q_{if} is included, range from 1.4 to 1.8×10^{13} cm^{-2}, for InN thicknesses scaling from 2 to 15 nm. This is expected, owing to the very large dielectric constant of HfO_2. Consequently, the band bending of InN is less severe and the subsequent QWs are shallower. In turn, the induced free-carrier gases are of lower density.

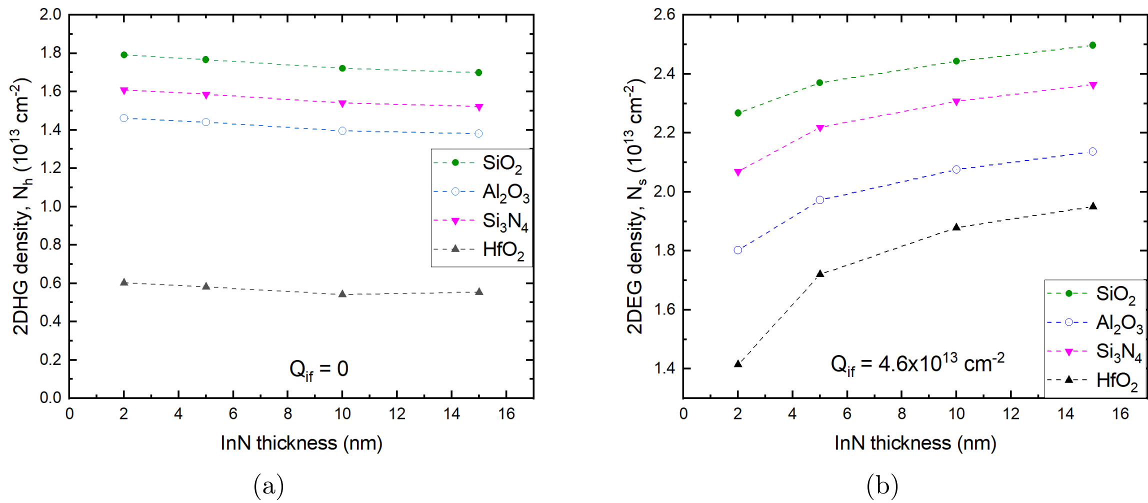

(a) (b)

Fig. 6.8: Calculated (a) hole and (b) electron gas density for every Ni/Insulator/ InN/GaN MIS structure versus InN layer thickness, (a) without and (b) with the interface positive sheet charge Q_{if}.

6.5.2 The InN/AlN Heterostructure

InN/AlN(0001)-based structures are now examined by SCSP equation solving calculations. The conduction band discontinuity between InN and AlN is equal to $\Delta E_C = -4.3$ eV [11]. Similarly, the Fermi level is pinned 0.9 eV above the conduction band minimum at the InN surface [6, 1]. Fig. 6.9 shows the energy band and charge distribution profiling of the bare heterostructures for 2, 5, 10 and 15 nm InN layer thicknesses. The formation of

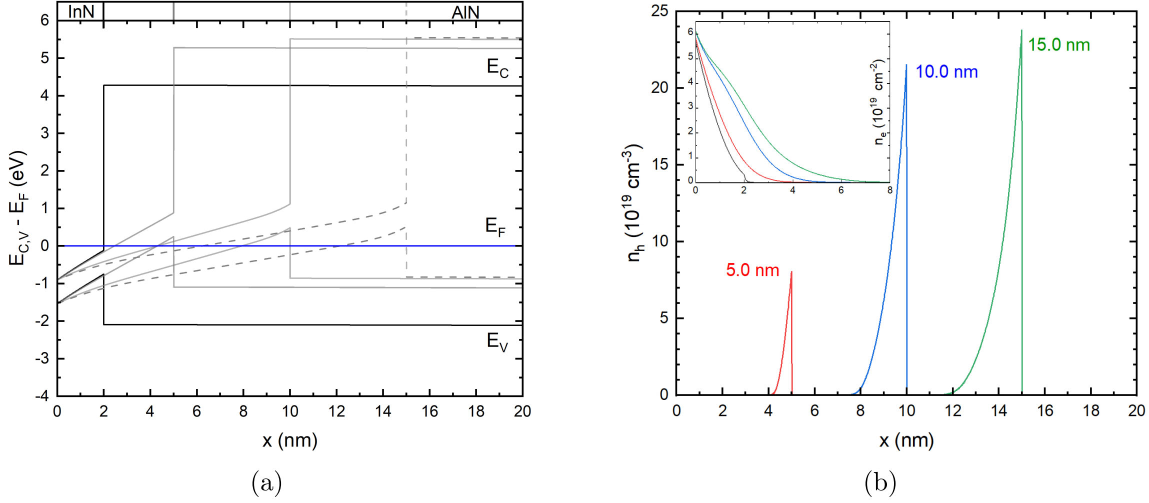

Fig. 6.9: (a) Simulated band diagrams and (b) hole concentration profiles for the InN (2, 5, 10, 15 nm)/GaN HEMT structure. There is no hole accumulation for the case of 2nm. Inset diagram shows the electron distribution.

both a 2DEG and a 2DHG is predicted at the InN layer. The 2DEG stems, of course, from the aforementioned Fermi level position, and is relatively confined within the first few nanometers from the surface. The 2DEG densities range $0.5 - 1.4 \times 10^{13}$ cm^{-2}, as the InN thickness is increased. The 2DHG is induced by the large spontaneous polarization discontinuity between InN and AlN. In fact, the spontaneous polarization constant of AlN is greater (more negative) than that of InN, as $P^{sp}_{AlN} = -0.090$ C/m^{-2} and $P^{sp}_{InN} = -0.042$ C/m^{-2}. Consequently, a negative sheet charge arises at the InN/AlN interface, which in turn leads to hole accumulation ($N_h = 0.2 - 2.1 \times 10^{13}$ cm^{-2}). However, the Fermi level does not cross the InN valence band when the corresponding thickness is 2nm. In this case, only a 2DEG is exhibited.

Si_3N_4/InN/AlN

The Ni/Si_3N_4/InN/AlN MIS system is first examined. Whether the positive sheet charge Q_{if} is considered or not, the aforementioned polarization-induced 2DHG is always present near the InN/AlN interface. If Q_{if} is ignored, the Fermi level is positioned within the valence band across the entirety of InN, and an additional hole concentration peak

is observed near the Si_3N_4/InN interface. The total 2DHG density across the InN layer is calculated to be $\sim 5.0 \times 10^{13}$ cm^{-2}. Including $Q_{if} = 4.6 \times 10^{13}$ cm^{-2}, the ultra-thin 2nm and 5nm epilayers are still fully depleted of electrons. The 2DHG at the other end, however, is present and of density equal to 0.8×10^{13} cm^{-2} and 1.0×10^{13} cm^{-2} respectively. The 10nm and 15nm InN layers are predicted to accumulate electrons at the Si_3N_4/InN contact. The 2DEG densities are, respectively, 0.5×10^{13} cm^{-2} and 0.9×10^{13} cm^{-2}. 2DHG concentrations are approximately equal to 1.6×10^{13} cm^{-2} and 2.1×10^{13} cm^{-2}.

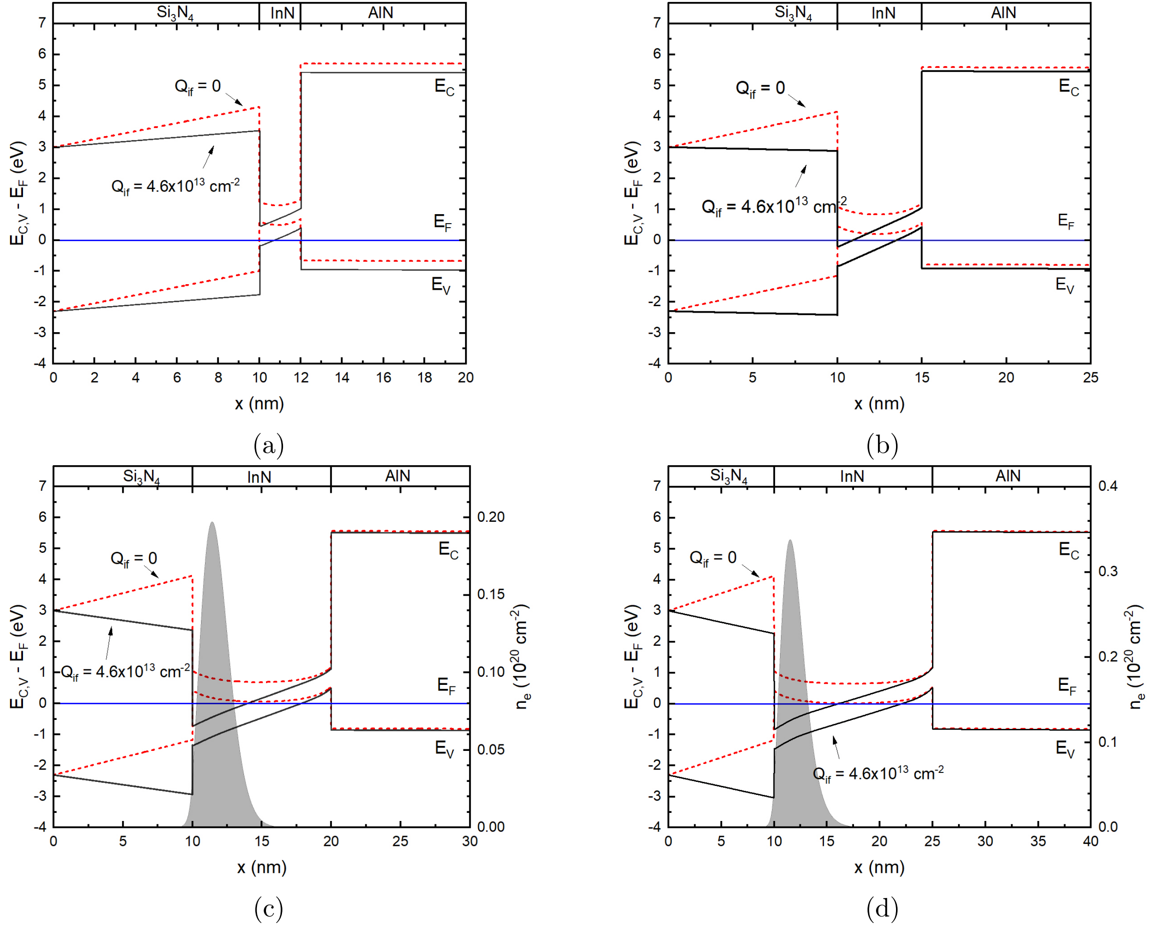

Fig. 6.10: Energy band diagrams and electron concentration (including Q_{if}) for the the Ni/Si_3N_4/InN/AlN MIS structure, for (a) 2nm, (b) 5 nm, (c) 10 nm and (d) 15 nm InN layer thicknesses.

HfO_2/InN/AlN

The results for hafnium dioxide are similar with the previously discussed case of Si_3N_4. Omitting Q_{if}, the 2DHG densities are predicted to be approximately 4.0×10^{13} cm^{-2}, and no electron accumulation is observed. Including Q_{if}, 2DEG formation is achieved only for the cases of 10nm and 15nm of InN. The corresponding densities are 0.3×10^{13} cm^{-2} and

0.6×10^{13} cm^{-2}. The unavoidable 2DHG concentrations range from 0.3×10^{13} cm^{-2} to 2.1×10^{13} cm^{-2}, increasing as the InN layer gets thicker.

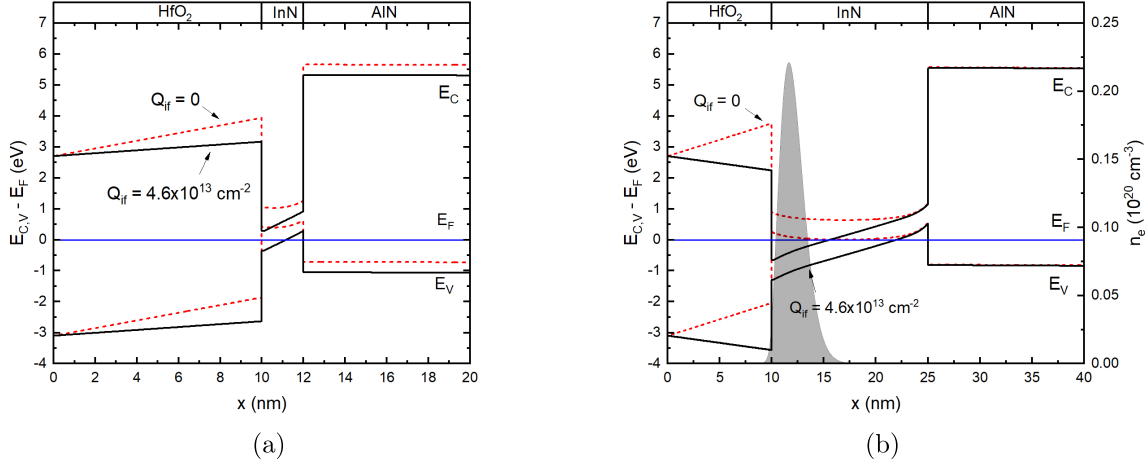

Fig. 6.11: Energy band diagrams and electron concentration (including Q_{if}) for the the Ni/HfO_2/InN/AlN MIS structure, for (a) 2nm and (b) 15 nm InN layer thicknesses.

Al_2O_3/InN/AlN

The effects of aluminum oxide are evaluated next. Again, the Fermi level is pinned below the valence band maxima of InN, if no positive sheet charge is considered at the Al_2O_3/InN interface, causing the accumulation of holes. The calculated densities of the predicted 2DHG are equal to $\sim 5 \times 10^{13}$ cm^{-2}. Taking Q_{if} into account, a QW is formed at the Al_2O_3/InN interface for InN thicknesses of 10nm and 15nm. The subsequent 2DEG densities are 0.4×10^{13} cm^{-2} and 0.8×10^{13} cm^{-2}, respectively. The 2DHG concentrations at the opposite end are estimated to be $0.8 - 2.1 \times 10^{13}$ cm^{-2}.

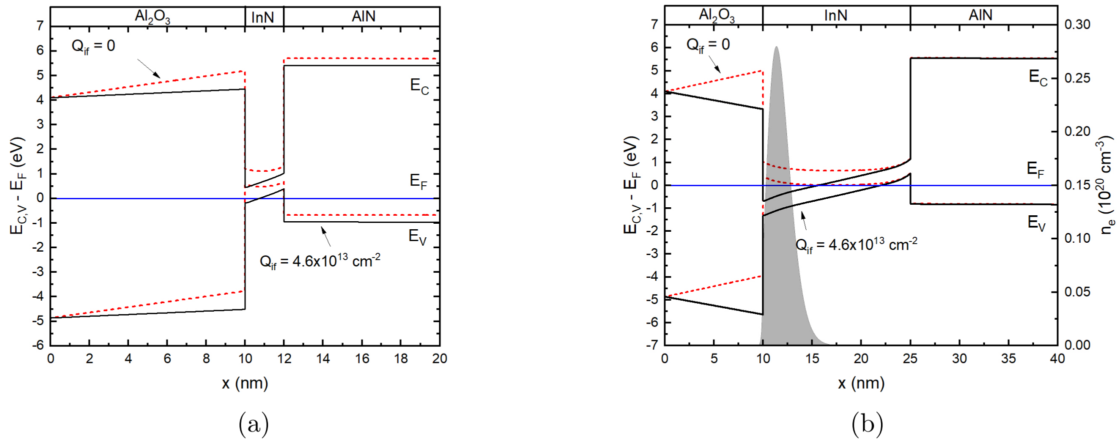

Fig. 6.12: Energy band diagrams and electron concentration (including Q_{if}) for the the Ni/Al_2O_3/InN/AlN MIS structure, for (a) 2nm and (b) 15 nm InN layer thicknesses.

SiO_2/InN/AlN

Finally, the Ni/SiO_2/InN/AlN MIS structure is examined. Ignoring Q_{if}, the observed 2DHG densities are approximately equal to 5.2×10^{13} cm^{-2}, while no electrons seem to accumulate at the InN layer. Including Q_{if}, a 2DEG is observed only for 10nm and 15nm layer thicknesses, and is of density 0.6×10^{13} cm^{-2} and 1.1×10^{13} cm^{-2}, respectively. 2DHG densities near the InN/AlN interface range $0.9 - 2.1 \times 10^{13}$ cm^{-2} with InN thickness.

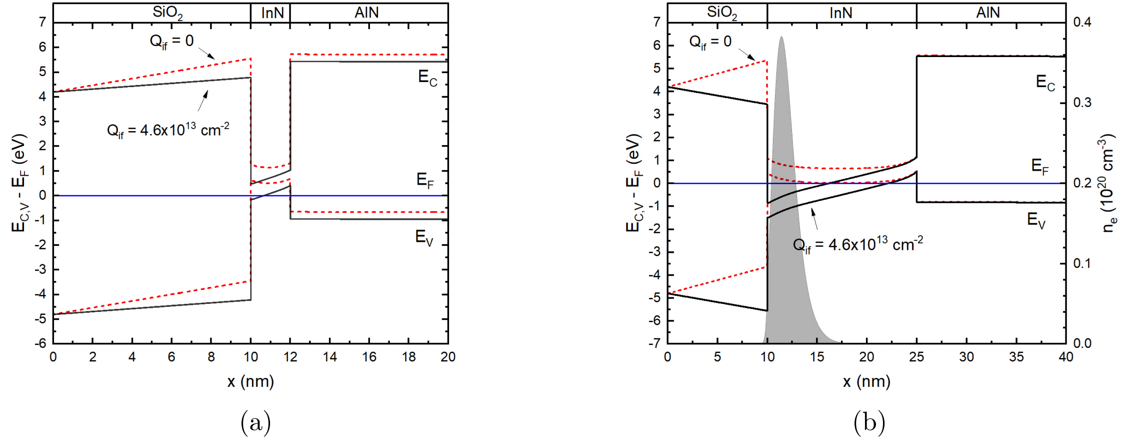

(a) (b)

Fig. 6.13: Energy band diagrams and electron concentration (including Q_{if}) for the the Ni/SiO_2/InN/AlN MIS structure, for (a) 2nm and (b) 15 nm InN layer thicknesses.

Conclusions

Interestingly, p-type conductivity is predicted for InN, when the aforementioned dielectrics are deposited on it. When InN is epitaxially grown on AlN, the large spontaneous polarization discontinuity between InN and AlN induces a negative sheet charge at the corresponding interface. In turn, a two-dimensional hole gas is formed in InN near AlN. The formation of said 2DHG seems to be inevitable for the structures examined above. No matter the thickness of the InN epilayer, or the dielectric deposited on it, a valence band QW is always predicted at the InN/AlN interface. When considering a positive sheet charge at the insulator/InN interface, hafnium oxide seems, again, to be the most appropriate material for the control of the induced two-dimensional electron gas. Its effectiveness extends to the case of no interface charges as well, as the respective polarization-induced 2DHG exhibits the lowest concentration. A higher donor density in InN (e.g. $N_D = 10^{19}$ cm^{-3}) slightly lowers the 2DHG density (and increases the 2DEG density), but fails to completely prevent its formation.

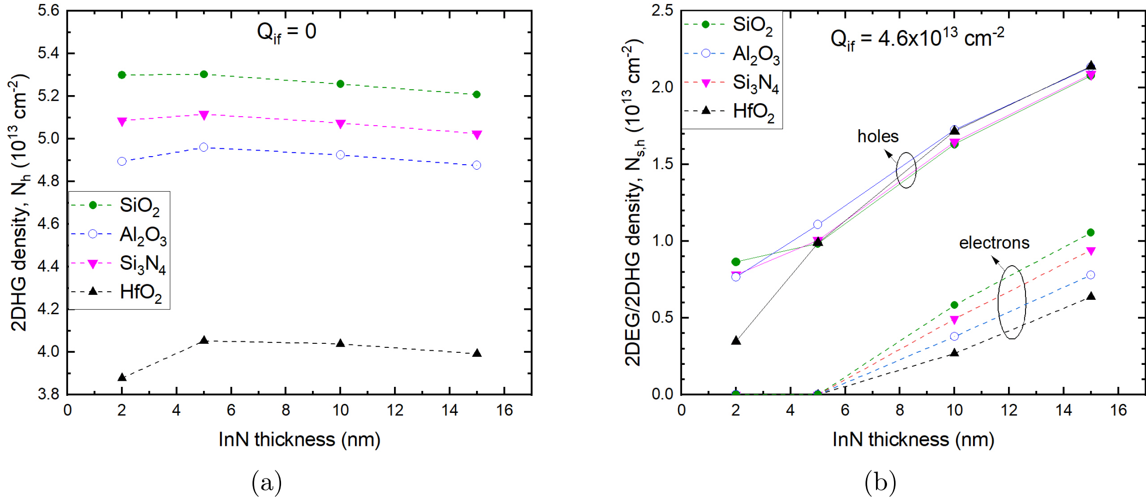

Fig. 6.14: Calculated free-carrier gas density for every Ni/Insulator/InN/AlN MIS structure versus InN layer thickness, (a) without and (b) with the interface positive sheet charge Q_{if}.

6.5.3 The InN/In$_x$Al$_{1-x}$N/GaN Heterostructure

As previously explained, a significant problem InN-on-GaN heterostructures face is the very large lattice mismatch of the constituent materials. From the first monolayer of epitaxial growth, InN tends to relax by introducing misfit dislocations [7]. An InAlN interlayer could help to overcome this obstacle, as the subsequent interfaces would be of less lattice mismatch and thus fewer misfit and threading dislocations. First, the effects of an $In_{0.8}Al_{0.2}N$ intermediate layer between InN and GaN are examined. The lattice mismatch between $In_{0.8}Al_{0.2}N$ and GaN remains high (~8%) and a high density of threading dislocations will form in the InAlN layer, which would be reduced as the layer grows thicker. The mismatch between InN and $In_{0.8}Al_{0.2}N$ is equal to approximately 2%, which could allow the pseudomorphic growth of thin InN layers on the InAlN buffer. In that case, no misfit or threading dislocations would arise at the InN surface and layer, respectively. As a result, fewer misfit dislocations are introduced into the heterostructure, thus increasing structural quality and device efficiency.

In the SCSP calculations that follow, $In_{0.8}Al_{0.2}N$ is considered relaxed on GaN, owing to the aforementioned large mismatch value. Due to the 2% lattice mismatch between InN and $In_{0.8}Al_{0.2}N$, a thin InN film could be considered fully strained on $In_{0.8}Al_{0.2}N$. Consequently, a piezoelectric polarization component is exhibited in InN, which is faced toward the [0001] crystallographic direction ($P^{pz}_{InN} > 0$). The alloy bandgap and conduction band discontinuities are calculated as explained in Section 5.3. Specifically, $E_{gap}(In_{0.8}Al_{0.2}N)=$ 1.34 eV, $\Delta E_C(InN/In_{0.8}Al_{0.2}N) = -0.44$ eV and $\Delta E_C(In_{0.8}Al_{0.2}N/GaN) = -1.96$ eV. Donor concentration in $In_{0.8}Al_{0.2}N$ is set equal to $N_D = 5\times10^{17}$ cm^{-2}. Three interlayer thicknesses are examined: 280 nm, 400 nm and 800 nm. Fig. 6.15 shows the energy band profiling for

the first case, incorporating 2-15nm InN epilayers.

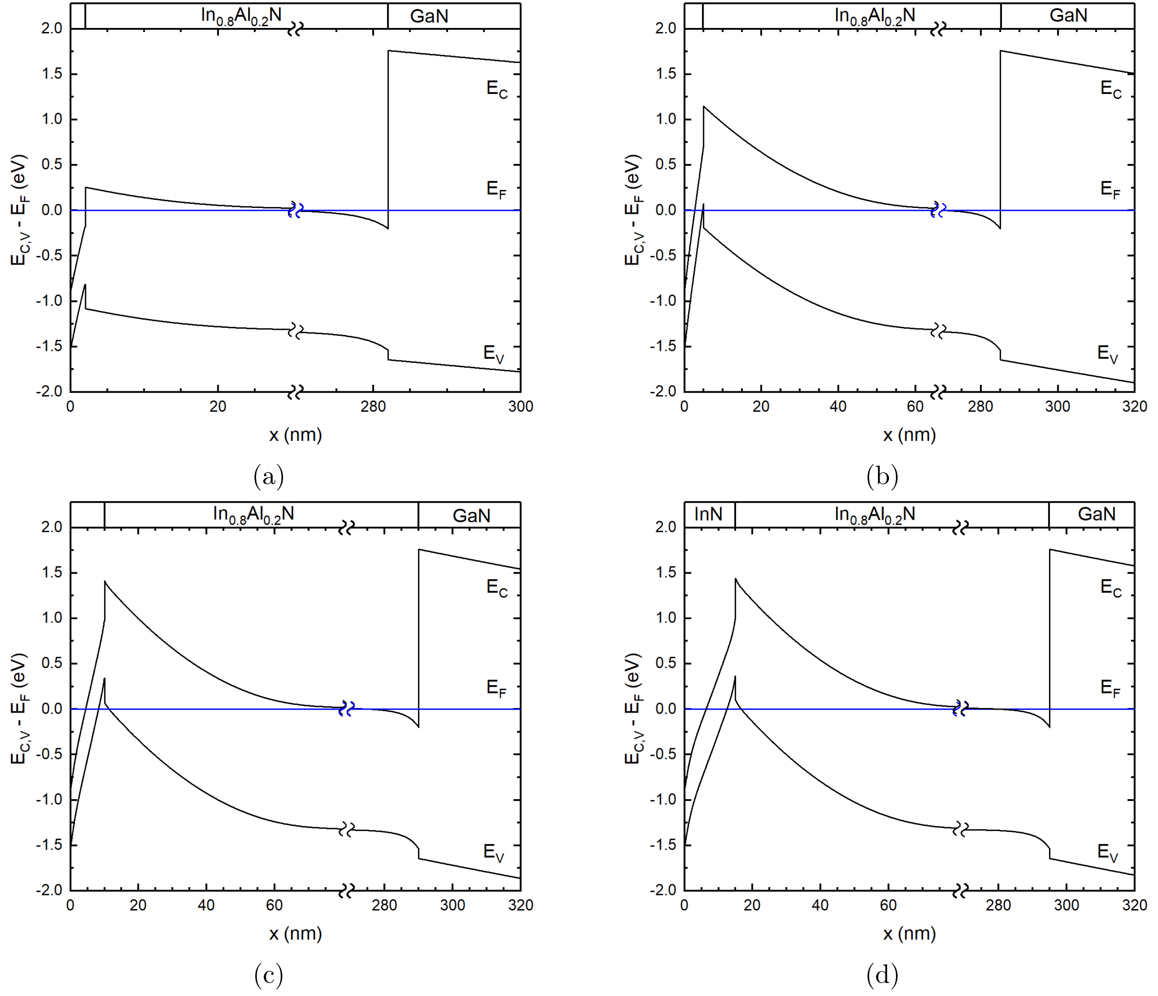

Fig. 6.15: Energy band diagrams of t_d InN/ 280nm $In_{0.8}Al_{0.2}N$/ GaN structures, for (a) $t_d = 2$nm, (b) $t_d = 5$nm, (c) $t_d = 10$nm, and (d) $t_d = 15$nm. Axis break-points denote flat-band region starting and ending points.

The piezo-polarization discontinuity between InN and $In_{0.8}Al_{0.2}N$ induces a negative sheet charge on their interface, equal to $\sigma_{pz} = -2.9 \times 10^{13}$ cm^{-2}. As a result, a hole accumulation is predicted at said interface, as the Fermi crosses the valence band, for each InN thickness except 2nm. For 5nm of InN, an extremely shallow valence band QW is formed, which induces a low-density 2DHG of the order of 10^{11} cm^{-2}. The 2DHG densities for 10nm and 15nm InN are 1.1×10^{13} cm^{-2} and 1.5×10^{13} cm^{-2}, respectively. The surface 2DEG density, due to the Fermi level pinning withing the conduction band, are approximately equal to $0.7 - 1.4 \times 10^{13}$ cm^{-2}, increasing with InN thickness. A second QW is formed at the InAlN/GaN interface (at the InAlN side), owing to spontaneous polarization discontinuity. Positive charges ($\sigma_{sp} = 4 \times 10^{12}$ cm^{-2}) are induced on the hetero-interface, which cause an electron accumulation of the order of 10^{13} cm^{-2}.

For the cases examined above, the InAlN layer thickness (280,400, or 800 nm) bears no effect on the calculated electron and hole gas densities in the corresponding QWs. In the region of thicknesses used in the SCSP calculations, InAlN gets to assume its flat-band profile, so each interface is independent of each other. However, due to the very high donor density assumed in InAlN, larger interlayer thicknesses would overall increase the calculated concentration of electrons throughout the structure.

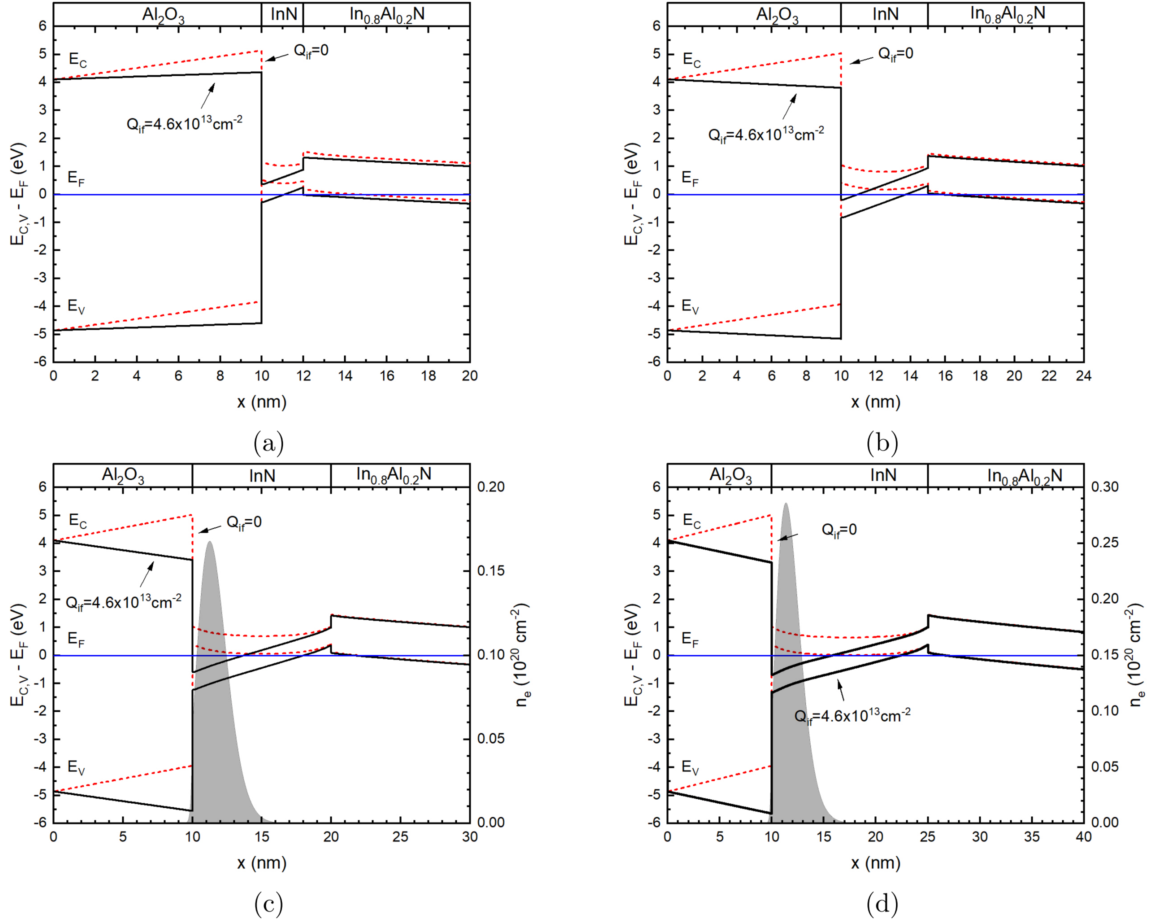

Fig. 6.16: Energy band diagrams and electron concentration (including Q_{if}) for the the Ni/Al_2O_3/InN/$In_{0.8}Al_{0.2}N$/GaN MIS structure, for (a) 2nm, (b) 5nm, (c) 10nm and (d) 15 nm InN layer thicknesses.

The effect of InN surface capping by amorphous Al_2O_3 deposition are evaluated next, as a representative case of MIS insulator materials. Again, two distinct cases are examined, wherein the positive sheet charge Q_{if} is or is not considered at the Al_2O_3/InN interface. Ignoring Q_{if}, the InN layer is fully depleted of electrons. Nevertheless, the Fermi level is pinned within the valence band of InN, leading to a hole accumulation equal to 4.3×10^{13} cm^{-2}. When Q_{if} is assumed, an electron accumulation is predicted near the Al_2O_3/InN interface, for the cases of 10nm and 15nm of InN. The respective 2DEG densities are 0.4×10^{13} cm^{-2} and 0.8×10^{13} cm^{-2}. The polarization induced negative charge on the

$InN/In_{0.8}Al_{0.2}N$ interface causes the formation of a 2DHG of density $0.3 - 1.6 \times 10^{13}$ cm^{-2}, increasing with InN thickness. Similarly, for the three InAlN thicknesses examined (280,400, 800 nm), said thickness does not affect the calculated 2DEG and 2DHG densities formed in each QW.

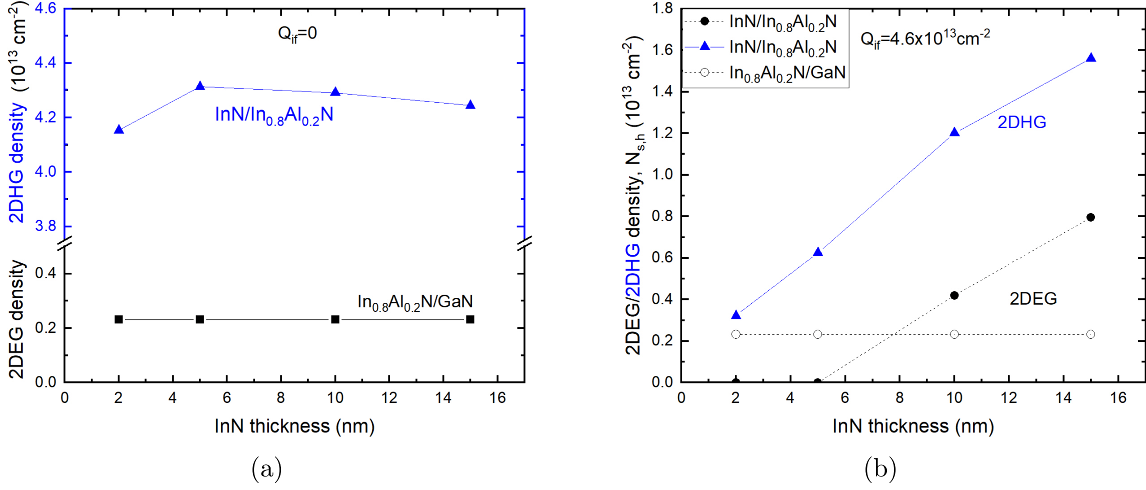

Fig. 6.17: Calculated 2DEG and 2DHG densities for the $Ni/Al_2O_3/InN/In_{0.8}Al_{0.2}N/GaN$ MIS structure versus InN layer thickness, (a) without and (b) with the positive sheet charge Q_{if} at the insulator/InN interface.

Graded $In_xAl_{1-x}N$

The incorporation of a graded set of $In_xAl_{1-x}N$ interlayers could produce gradual strain relaxation from the GaN to the $In_{0.8}Al_{0.2}N$ lattice constant. A sequence of interfaces of less lattice mismatch may reduce the total density of threading dislocations that reach the finally grown InN layer. In addition, the pseudomorphic growth of InN on the final $In_{0.8}Al_{0.2}N$ layer would prevent the presence of misfit dislocations at the back barrier interface, as well as the relaxation side effect of threading dislocation introduction.

Here, four InAlN layers between InN and GaN are considered. Specifically, the HEMT structure examined is $InN/In_{0.8}Al_{0.2}N/In_{0.6}Al_{0.4}N/\ldots/$ $In_{0.2}Al_{0.8}N/GaN$. Each layer is of the same thickness t_{epi} ($= 70, 100, 200$ nm). All InAlN layers are considered relaxed, but InN is assumed to be fully strained on $In_{0.8}Al_{0.2}N$.

The InN endlayer seems to be unaffected by the InAlN epilayer thickness. The electron and hole accumulation predicted at the InN surface and the $InN/In_{0.8}Al_{0.2}N$, respectively, bear the same densities as the ones calculated for the case of $InN/In_{0.8}Al_{0.2}N/GaN$: $10^{12} - 10^{13}$ cm^{-2}. The 2DHG is predicted only for 10 and 15 nm of InN.

Beyond the surface carrier accumulation, the graded structure at hand could potentially exhibit multiple conductive channels, as each interface tends to form its own two-dimensional gas of free carriers. Moving from top to bottom (starting from $In_{0.8}Al_{0.2}N$),

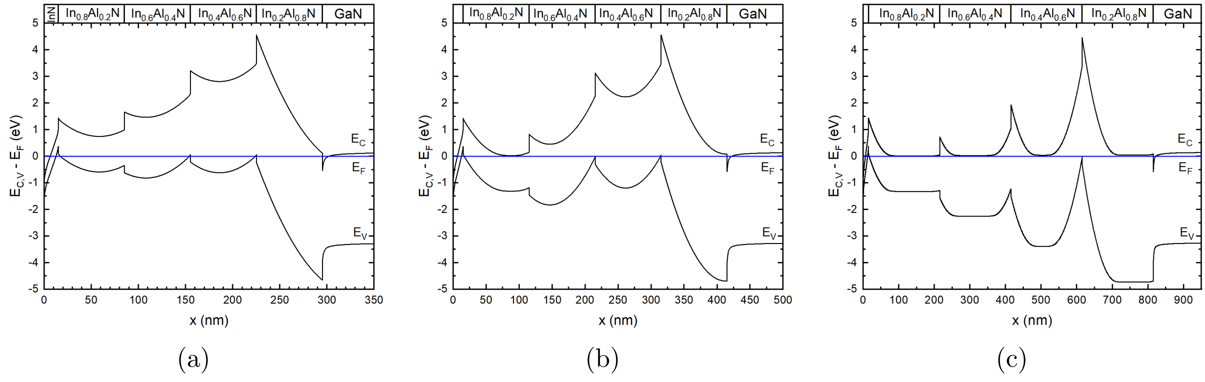

Fig. 6.18: Energy band diagrams for the the 15nm InN/$4 \times t_{epi}$ $In_xAl_{1-x}N$/GaN HEMT structure, for t_{epi} = (a) 70nm, (b) 100nm, and (c) 200nm.

as the molar fraction of AlN increases, the spontaneous polarization does so too. Due to the polarization discontinuity, a negative sheet charge arises at each interface between two InAlN layers, which in turn attracts holes. This phenomenon is severe in the case of $t_{epi} = 70$ nm, wherein the band profile of each InAlN layer fails to reach its respective flat-band state and a p-type conductivity is established throughout the InAlN layers[1]. 2DHG's of the order of 10^{12} cm^{-2} are accumulated at the $In_{0.6}Al_{0.4}N/In_{0.4}Al_{0.6}N$ and $In_{0.4}Al_{0.6}N/In_{0.2}Al_{0.8}N$ interfaces, which decrease as $In_xAl_{1-x}N$ thickness increases. For $t_{epi} = 100$ nm, the respective 2DHG densities drop to 10^{11} cm^{-2} and 10^{12} cm^{-2}, while for $t_{epi} = 200$ nm no hole accumulation is predicted near the aforementioned interfaces.

A QW is formed at the interface between GaN and $In_{0.2}Al_{0.8}N$. The polarization of GaN is smaller than that of $In_{0.2}Al_{0.8}N$, inducing a positive sheet charge at their interface and a 2DEG arises, of density equal to 10^{13} cm^{-2}. For the cases examined, the InAlN-epilayer thickness has negligible effects on the latter. All aforementioned free-carrier gas densities are independent of InN thickness.

Moving on, the Ni/Al_2O_3/InN/ (graded) $In_xAl_{1-x}N$/GaN MIS system is examined, for the various InN and InAlN layer thicknesses. The effects of the insulator extend only to the InN layer. Regarding the free-carrier concentration in the latter, results are identical to those calculated considering a unique $In_{0.8}Al_{0.2}N$ layer on GaN substrate (see Fig. 6.16). If no positive sheet charge is considered at the Al_2O_3/InN interface, the InN layer is depleted of electrons but exhibits a hole accumulation of approximately 4×10^{13} cm^{-2}, regardless of InAlN layer thickness. Assuming Q_{if}, the 2DHG density is lowered to $0.4 - 1.6 \times 10^{13}$ cm^{-2}. For 10nm and 15nm of InN, a 2DEG is predicted of density 0.4 and 0.8×10^{13} cm^{-2}, respectively.

[1]Remember that a high donor density of 5×10^{17} cm^{-3} was assumed for InAlN, which should put the Fermi level very close to the conduction band at flat-band regions.

6.5.4 The InN/$In_xAl_{1-x}N$/AlN Heterostructure

The same scenarios are examined using an aluminum nitride substrate. The predicted energy band profile for the top contact is, as expected, identical to the one derived from the analysis for the GaN substrate. Taking a closer look at the $In_{0.8}Al_{0.2}N$/AlN interface,

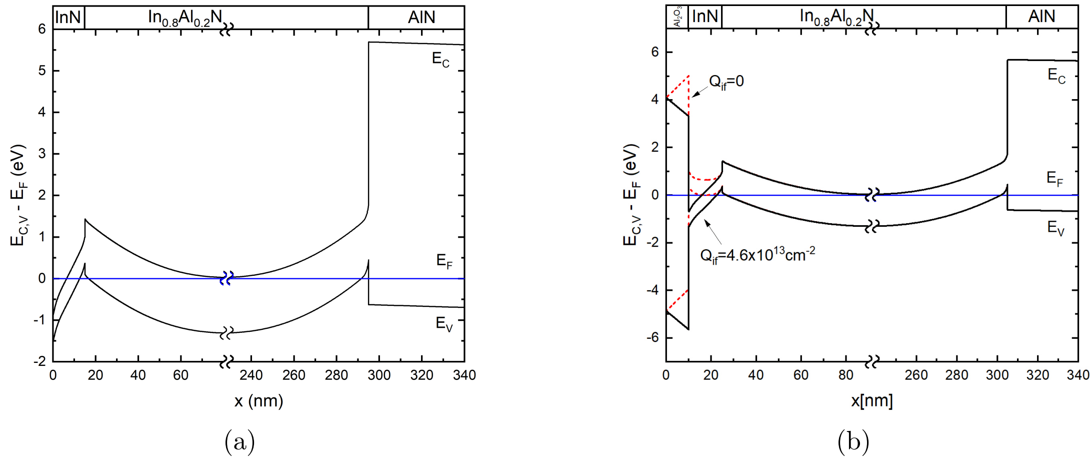

(a) (b)

Fig. 6.19: Energy band diagrams of (a) 15nm InN/ 280nm $In_{0.8}Al_{0.2}N$/AlN and (b) Ni/10nm Al_2O_3/15nm InN/ 280nm $In_{0.8}Al_{0.2}N$/AlN structures. Axis break-points denote flat-band region starting and ending points.

the formation of a two-dimensional hole gas is predicted. The spontaneous polarization discontinuity between the two layers induces a negative sheet charge on the interface, which in turn induces a 2DHG of density 2.5×10^{13} cm^{-2}.

Graded $In_xAl_{1-x}N$

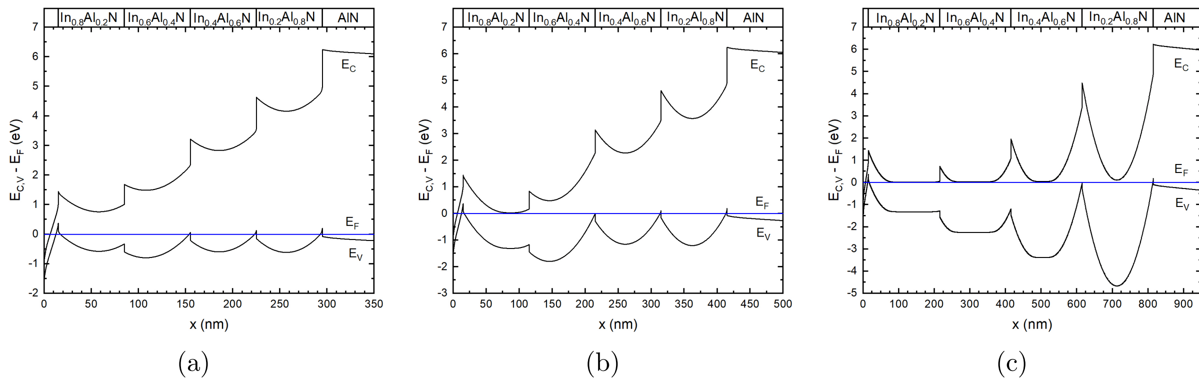

(a) (b) (c)

Fig. 6.20: Energy band diagrams for the the 15nm InN/4 $\times$ t_{epi} $In_xAl_{1-x}N$/AlN HEMT structure, for t_{epi} = (a) 70nm, (b) 100nm, and (c) 200nm.

Again, free-carrier concentrations in InN are independent of InAlN epilayer thickness. They exhibit the exact same values ($0.7-1.4\times10^{13}$ cm^{-2} for electrons and $\sim 10^{13}$ cm^{-2} for holes), indicating that the AlN buffer layer does not affect the InN endlayer. The carrier

concentrations at each interface between InAlN layers is also found to be independent of the buffer layer used. Of course, the electron accumulation predicted at $In_{0.2}Al_{0.8}$/GaN is now exchanged for a hole accumulation at the $In_{0.2}Al_{0.8}N$/AlN interface, whose density is of the order of 10^{13} cm^{-2} and slightly decreases as the InAlN layer get thicker.

When considering the MIS structure examined above, the predicted behaviour is analogous. That is, the insulator's effect are strictly limited to InN.

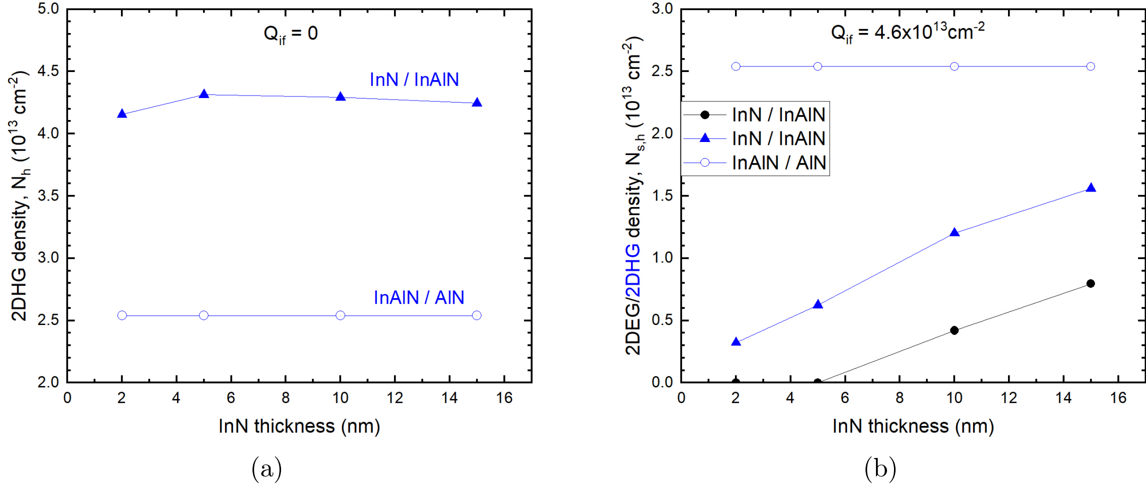

Fig. 6.21: Calculated 2DEG and 2DHG densities for the $Ni/Al_2O_3/InN/In_{0.8}Al_{0.2}N/AlN$ MIS structure versus InN layer thickness, (a) without and (b) with the interface positive sheet charge Q_{if}.

Conclusions

In summary, when InAlN is used as an intermediate layer between InN and the substrate, the latter seems to be of no importance to the charge distribution profile of InN, for the InAlN thicknesses examined. An $In_{0.8}Al_{0.2}N$ interlayer seems to facilitate the electron depletion of InN, thanks to piezoelectric polarization-induced sheet charge at the respective interface. However, a hole-gas seems to also be present in InN under these conditions. What is more, additional conductive channels are predicted at each interface of the structures above, which increase the overall free-carrier concentration in the device.

6.5.5 The Effects of Misfit Dislocations

The results above indicate that when InN is grown on AlN, a hole accumulation is predicted (in the ideal case) at the InN/AlN interface by the related polarization discontinuity. However, the presence of holes could be hidden by their low mobility, resulting to negligible contribution of holes to the layer's conductance in comparison to the electrons. What is more, no direct evidence of the 2DHG was observed by Hall-effect measurements, similar to other works [12, 13]. The disagreement between SCSP calculations and Hall effect

measurements might stem from additional sources of positive charge that attract electrons, as the SCSP calculations performed so far have taken into account only polarization-induced sheet charges.

Crystal defects have been suggested as sources of unintentional donor-like states in InN. A correlation between threading dislocation (TD) density and electron concentration has been previously reported [2, 3]. Misfit dislocations (MDs) might also contribute to charge redistribution in InN. As edge dislocations, MDs may act as sources of donor-like states, which when ionized are positively charged. The heteroepitaxial growth of InN on GaN has been found to generate a network of three equally spaced arrays of 60° misfit dislocations in the InN/GaN interface [14], which are introduced every 9 InN $\{10\bar{1}0\}$ atomic planes in the continuous film. A misfit dislocation spacing of D = 2.75 nm was measured.

We expect the results to be similar for InN-on-AlN heterostructures. The total length of dislocation lines per cm^2 is of the order of 10^{14} nm. In the following SCSP calculations, MDs are assumed to act as donors. Various charge state values examined, ranging from +1 per 100 nm to +1 per 2 nm. Equivalently, a positive sheet charge Q_{MD} is considered at the InN/AlN interface, ranging from 10^{12} to 5×10^{13} cm^{-2}.

Assuming there is no interface charge at the HfO_2/InN interface, the predicted 2DHG in InN seems to vanish for high values of charge contribution by MDs ($\sim +1e/3$ nm). For the case of 15 nm of InN, a low-density 2DHG is still present, which is confined near the HfO_2/InN interface, due to the respective polarization charge. A 2DEG is predicted at the InN/AlN interface for the cases of 5, 10 and 15 nm of InN for similar charge state values.

If the positive sheet charge $Q_{if} = 4.6 \times 10^{13}$ cm^{-2} is considered at the HfO_2/InN interface, the MD charge value above which no holes are accumulated is significantly lower. Specifically, for the 2 nm InN film, almost no holes are accumulated within it, as the 2DHG density starts from $\sim 0.3 \times 10^{13}$ cm^{-2}. In addition, the 2nm InN channel seems to be fully depleted of carriers for Q_{MD} range, from 0.5 to 1.5×10^{13} cm^{-2}. In the case of 5nm of InN, for $Q_{MD} = 10^{13}$ cm^{-2}, the 2DHG vanishes, and the formation of a 2DEG is now predicted. For 10 and 15 nm of InN, the results are similar. The predicted 2DHG is prevented for $Q_{MD} = 2 \times 10^{13}$ cm^{-2}. Up until that value, there is constant 2DEG density, which is located near near the HfO_2/InN interface, due to Q_{if}. Further increase of Q_{MD} leads to a higher electron accumulation.

6.5.6 The Effects of Donor Concentration

By Hall effect measurements on the bare 5nm InN-on-GaN (0001) heterostructure, the 2DEG density whithin the InN channel was determined to be $N_s = 8.2 \times 10^{13}$ cm^{-2}. However, SCSP calculations predicted a lower density for the accumulated electron gas of

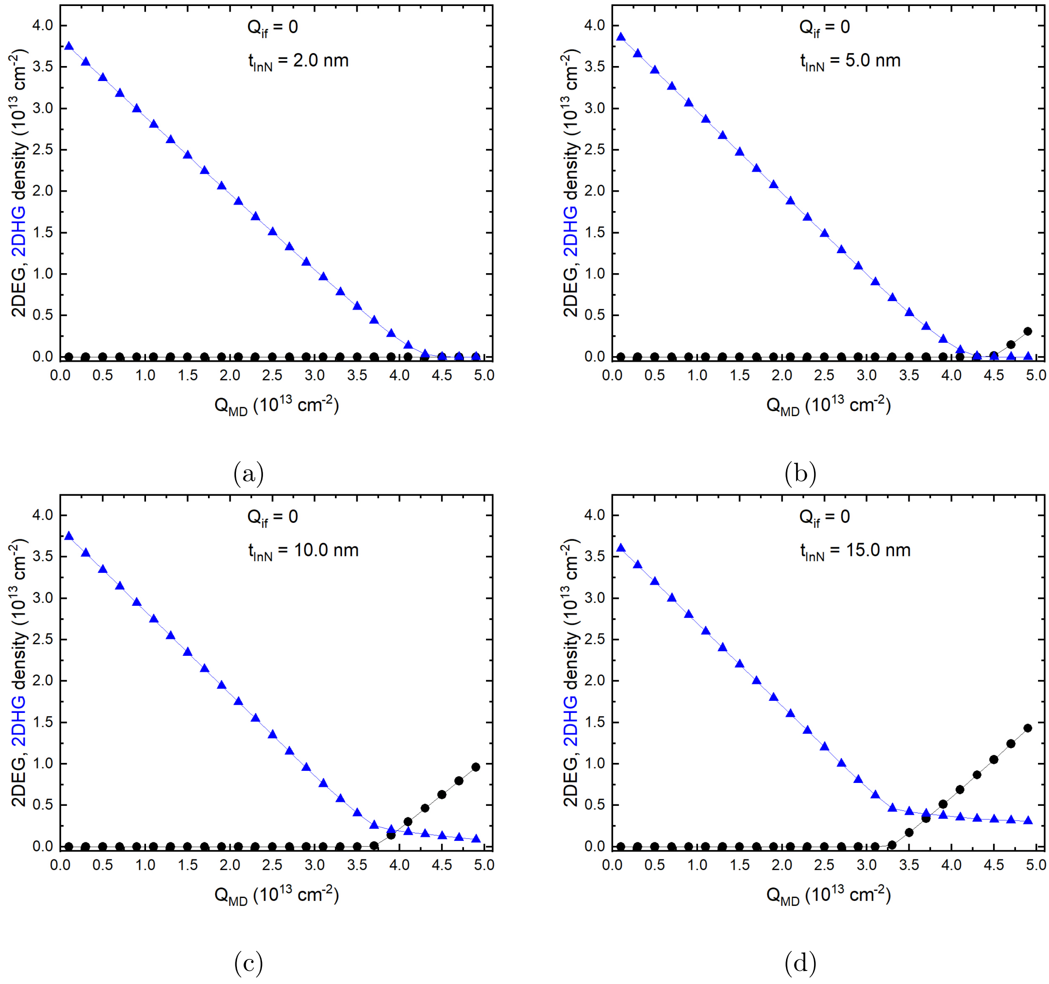

Fig. 6.22: 2DEG and 2DHG densities versus misfit dislocation charge for the Ni/HfO_2/InN/AlN MIS structure for (a) 2nm, (b) 5nm, (c) 10nm and (d) 15 nm InN layer thicknesses, with no Q_{if} at the HfO_2/InN interface.

$N_s = 2.2 \times 10^{13}$ cm^{-2}. This disagreement could be due to an underestimation of the bulk donor concentration within InN.

In the following SCSP calculations, potential values of InN donor density are investigated. Assuming N_D^{InN} ranges from 10^{18} cm^{-3} to 5×10^{20} cm^{-3}, the aforementioned bare and MIS heterostructures are revisited, using 5 nm of InN on either GaN or AlN buffer layers. Indicatively, Al_2O_3 is used as the insulating material in the examined MIS structures. Similarly, the structures are examined with and without the positive sheet charge $Q_{if} = 4.6 \times 10^{13}$ cm^{-2} at the Al_2O_3/InN interface.

The bare InN film on GaN or AlN buffer layers is examined first. The Fermi level is pinned 0.9 eV above the conduction band minimum of the InN surface. The predicted 2DEG densities are relatively constant for donor densities up to 10^{19} cm^{-3} for both buffer layers. The aforementioned 2DEG density observed in the InN/GaN structure by Hall-effect measurements is acquired by considering a donor density of $\sim 2 \times 10^{20}$ cm^{-3}

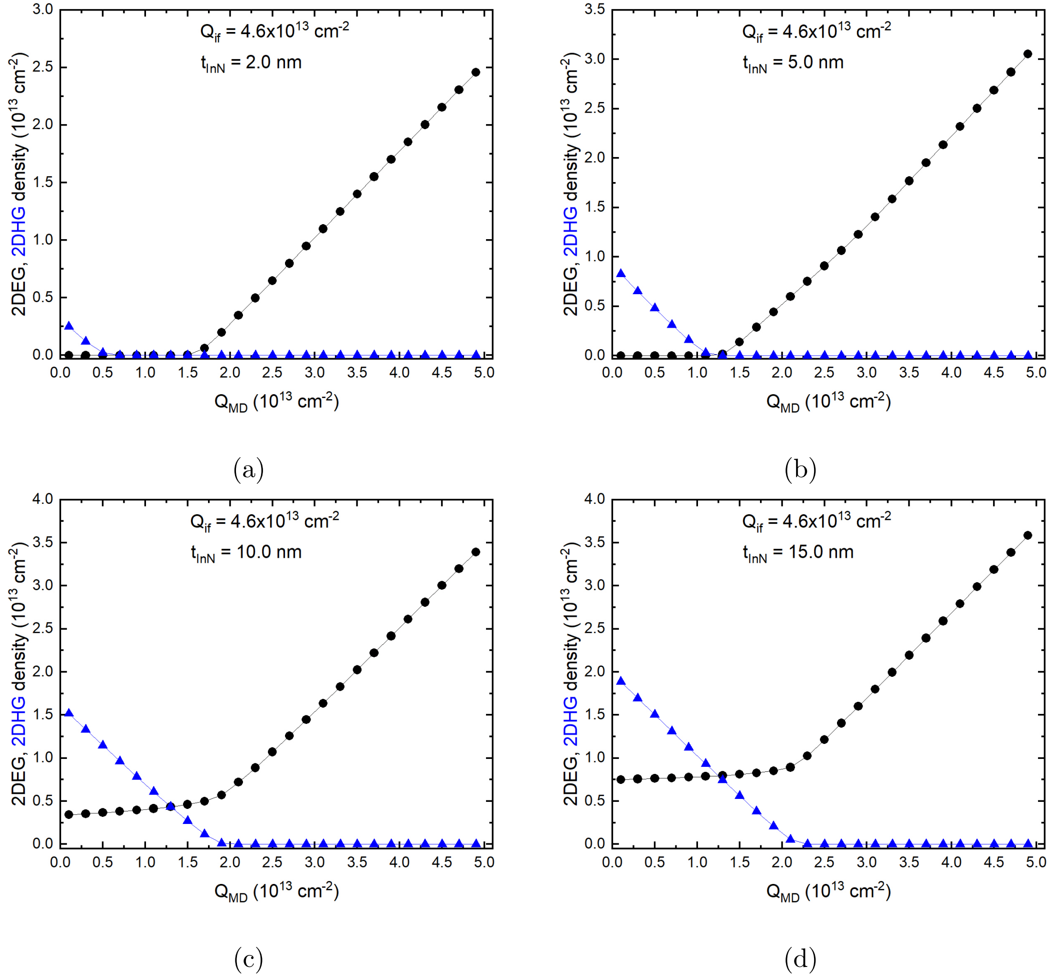

Fig. 6.23: 2DEG and 2DHG densities versus misfit dislocation charge for the Ni/HfO_2/InN/AlN MIS structure for (a) 2nm, (b) 5nm, (c) 10nm and (d) 15 nm InN layer thicknesses,inluding Q_{if} at the HfO_2/InN interface.

in the InN layer. This extremely high donor concentration may be plausible considering the highly defective InN layer, due to large lattice mismatch.

When InN is grown on AlN, assuming $N_D = 10^{18}$ cm^{-3}, the formation of a 2DHG was predicted at the InN/AlN interface, of density approximately equal to 3×10^{12} cm^{-2}. Said hole accumulation seems to be prevented for InN donor densities greater than $\sim 3 \times 10^{19}$ cm^{-3}. Up until that donor concentration, the density of the surface 2DEG remains unaffected ($\sim 10^{13}$ cm^{-2}).

As far as the Ni/Al_2O_3/InN/GaN structure is concerned, assuming there is no positive sheet charge at the Al_2O_3/InN interface, the channel is predicted to be fully depleted of electrons for donor densities up to $\sim 3 \times 10^{19}$ cm^{-3}. Additionally, the predicted 2DHG vanishes around that region of values. The behavior of the Ni/Al_2O_3/InN/AlN MIS system is almost identical, with the sole difference being that the critical donor density value is $\sim 10^{20}$ cm^{-3}.

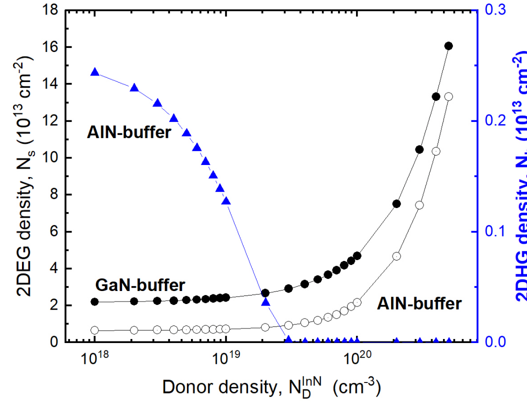

Fig. 6.24: Calculated 2DEG density versus InN donor density for the InN/GaN and InN/AlN heterostructures.

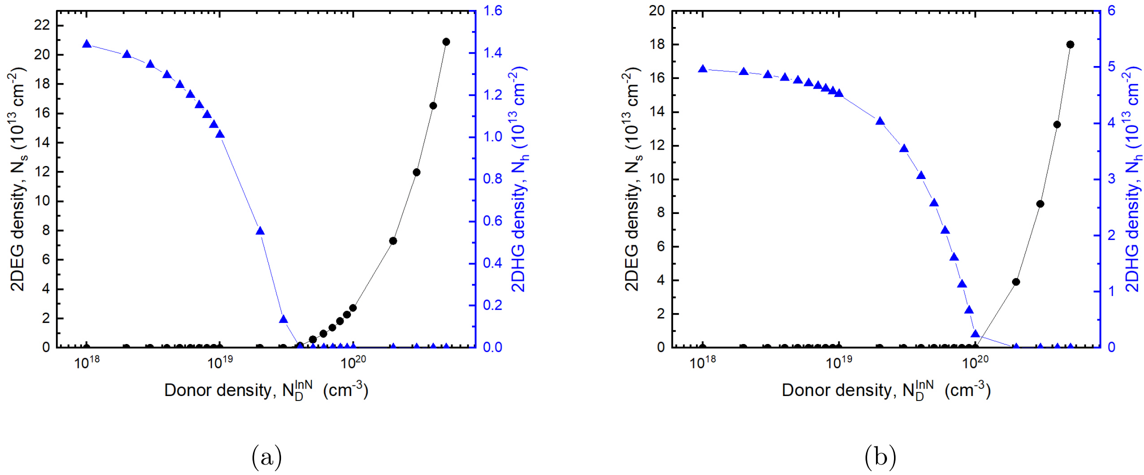

Fig. 6.25: Calculated 2DEG and 2DHG densities for the (a) Ni/Al_2O_3/InN/GaN and (b) Ni/Al_2O_3/InN/AlN MIS structures versus InN donor density. No positive charge was considered at the Al_2O_3/InN interface.

Including the positive sheet charge Q_{if} at the Al_2O_3/InN interface, there is no hole accumulation in InN when using a GaN buffer, and as expected electron accumulation is increased with donor density. Considering the AlN buffer, the previously predicted 2DHG vanishes for a donor density value of approximately 4×10^{19} cm^{-3}, while at the same value a 2DEG arises.

At this point, it is important to note that for the Ni/10 nm Si_3N_4/ 2nm InN/GaN MIS system studied by Zervos et al. [10], an InN bulk donor density of 10^{20} cm^{-3}, reduces the necessary (for SCSP calculations to be consistent with experimental data) interface charge to 2.6×10^{13} cm^{-2}, which is remarkably close to the polarization-induced sheet charge at the Si_3N_4/InN interface.

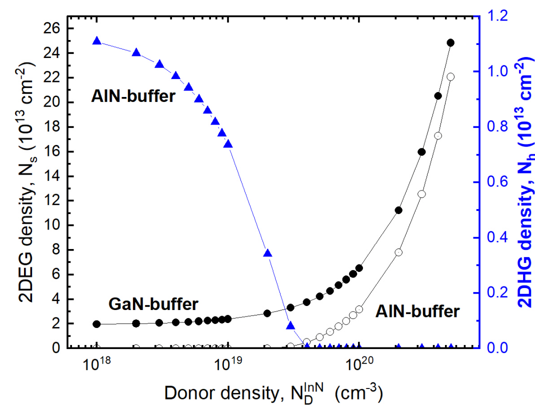

Fig. 6.26: Calculated 2DEG and 2DHG densities for the Ni/Al_2O_3/InN/GaN(AlN) MIS structures versus InN donor density. A positive charge of 4.6×10^{13} cm^{-2} was considered at the Al_2O_3/InN interface.

References

[1] C. G. Van de Walle, J. L. Lyons, and A. Janotti *phys. stat. sol. (a)*, vol. **207**, no. 5, pp. 1024–1036, (2010).

[2] L. F. J. Piper, T. D. Veal, C. F. McConville, H. Lu, and W. J. Schaff *Appl. Phys. Lett.*, vol. **88**, no. 25, (2006).

[3] A. Adikimenakis, P. Chatzopoulou, G. P. Dimitrakopoulos, T. Kehagias, K. Tsagkaraki, M. Androulidaki, G. Doundoulakis, J. Kuzmik, and A. Georgakilas *J. Solid State Sci.*, vol. **9**, (2020). 015006.

[4] H. Lu, W. J. Schaff, L. F. Eastman, and C. E. Stutz *Appl. Phys. Lett.*, vol. **82**, no. 11, pp. 1736–1738, (2003).

[5] I. Mahboob, T. D. Veal, C. F. McConville, H. Lu, and W. J. Schaff *Phys. Rev. Lett.*, vol. **92**, p. 036804, (2004).

[6] P. D. C. King, T. D. Veal, A. Adikimenakis, H. Lu, L. R. Bailey, E. Iliopoulos, A. Georgakilas, W. J. Schaff, and C. F. McConville *Appl. Phys. Lett.*, vol. **92**, no. 17, (2008). 172105.

[7] E. Dimakis, E. Iliopoulos, K. Tsagaraki, T. Kehagias, P. Komninou, and A. Georgakilas *J. Appl. Phys.*, vol. **97**, (2005). 113520.

[8] S. Birner, T. Zibold, T. Andlauer, T. Kubis, M. Sabathil, A. Trellakis, and P. Vogl *IEEE Transactions on Electron Devices*, vol. **54**, no. 9, pp. 2137–2142, (2007).

[9] S. Ganguly, J. Verma, G. Li, T. Zimmermann, H. Xing, and D. Jena *Appl. Phys. Lett.*, vol. **99**, no. 19, (2011). 193504.

[10] C. Zervos, A. Adikimenakis, P. Beleniotis, A. Kostopoulos, M. Kayambaki, K. Tsagaraki, G. Konstantinidis, and A. Georgakilas *Appl. Phys. Lett.*, vol. **108**, no. 14, (2016). 142102.

[11] S.-H. Wei and A. Zunger *Appl. Phys. Lett.*, vol. **72**, no. 16, pp. 2011–2013, (1998).

[12] A. Bairamis, C. Zervos, A. Adikimenakis, A. Kostopoulos, M. Kayambaki, K. Tsagaraki, G. Konstantinidis, and A. Georgakilas *Appl. Phys. Lett.*, vol. **105**, no. 11, (2014). 113508.

[13] G. Li, B. Song, S. Ganguly, M. Zhu, R. Wang, X. Yan, J. Verma, V. Protasenko, H. Grace Xing, and D. Jena *Appl. Phys. Lett.*, vol. **104**, no. 19, (2014). 193506.

[14] T. Kehagias, E. Iliopoulos, A. Delimitis, G. Nouet, E. Dimakis, A. Georgakilas, and P. Komninou *physica status solidi (a)*, vol. **202**, no. 5, pp. 777–780, (2005).

7. Conclusions

One dimensional self-consistent Schrödinger-Poisson (SCSP) calculations has been carried out for the equilibrium energy band and charge distribution profiling of planar InN heterostructures on GaN, AlN and InAlN (0001) buffer layers, along the growth axis, to gain insight on the design of III-nitride field effect transistors with InN channel. The formation of MIS contacts with four different dielectrics (Si_3N_4, HfO_2, Al_2O_3, SiO_2) on InN was also investigated. The effects of InN thickness in the range from 2 to 15 nm and of bulk donor concentration from 10^{18} to 5×10^{20} cm^{-3}, the Fermi level pinning at the bare InN surface, as well as of the presence of fixed positive sheet charges at the insulator/InN and the bottom InN/buffer interfaces were considered.

The energy band profile of InN is significantly affected by the polarization-induced charges at the InN/buffer interface (bottom interface). Specifically, a positive sheet charge occurs at the InN/GaN interface, which favors an accumulation of electrons, whereas the exhibited negative charge at the InN/AlN interface contributes to the depletion of the InN channel of electrons. However, owing to the very large polarization discontinuity between InN and AlN, a two dimensional hole gas (2DHG) is predicted at the aforementioned interface.

The 2DHG formation at the InN/AlN bottom interface could be prevented by assuming a positive charge (Q$\sim 1 - 2 \times 10^{13}$ cm^{-2}) confined at the bottom interface. The (physical) origin of this charge could be donor states associated with the network of misfit dislocations, whose dislocation line length per cm^{-2} is of the order of 10^{14} nm. This would require a charge contribution of +1e per 5 nm of misfit dislocation line. Alternatively, no 2DHG formation could result from a high bulk donor concentration ($\sim 10^{20}$ cm^{-3}) within the thin InN layer.

Similar results with the case of AlN buffer are acquired by considering a compressively strained InN layer on $In_{0.8}$ $Al_{0.2}N$ buffer layer, being either homogeneous or compositionally step-graded alloy on AlN substrate. The reduction of the spontaneous polarization of the $In_{0.8}$ $Al_{0.2}N$ buffer, in comparison to AlN buffer, is compensated by the piezoelectric polarization in the compressively strained InN, whose sign is opposite to the spontaneous polarization. I.e. the polarization discontinuity $\Delta\vec{P}$ at the bottom InN/buffer interface is approximately conserved. In the case of the compositional step-graded InAlN buffer, parallel conductive channels are also predicted near successive InAlN interfaces. An InAlN buffer layer on GaN would lead to the formation of a 2DEG at the respective interface which is undesirable.

The formation of InN-based Metal-Insulator-Semiconductor (MIS) structures using Si_3N_4, HfO_2, Al_2O_3 or SiO_2, efficiently depletes the InN channel of electrons. The depletion effect is stronger as the insulator dielectric constant increases, with HfO_2 exhibiting the lowest densities of mobile carriers. A positive sheet charge at the insulator/InN interface, would result in the formation of a two-dimensional electron gas (2DEG), which is closer to experimental results.

The feasibility of the growth of continuous 2-5 nm InN films on GaN or AlN (0001) buffer layers has been showcased. Atomic force microscopy measurements indicated atomic-smooth surfaces with a root mean square roughness of 0.3 nm. Hall effect measurements on an InN/GaN heterostructure determined a high 2DEG density of approximately 8×10^{13} cm^{-2}. Considering a high InN donor concentration of $\sim 2 \times 10^{20}$ cm^{-3}, SCSP calculations are consistent with experimental results.